

Investigation of electronic order using
resonant soft x-ray diffraction

Inaugural-Dissertation
zur
Erlangung des Doktorgrades
der Mathematisch-Naturwissenschaftlichen Fakultät
der Universität zu Köln

vorgelegt von
Justina Schlappa
aus Oppeln (Opole)

Köln 2006

Berichterstatter:

Prof. Dr. L. H. Tjeng

Prof. Dr. J. R. Schneider

Vorsitzender der Prüfungskommission:

Prof. Dr. L. Bohatý

Tag der mündlichen Prüfung: 1. Dezember 2006

Contents

Introduction	5
1 Resonant soft x-ray diffraction	9
1.1 X-ray diffraction	9
1.1.1 Geometry	11
1.1.2 Structure factor	12
1.1.3 Scattering volume	13
1.2 Atomic form factor	13
1.2.1 Isotropic terms	14
1.2.2 Resonant terms	15
1.3 X-ray optics	16
1.3.1 Refraction	17
1.3.2 Reflectivity	19
1.3.3 Absorption	19
1.4 Spectroscopic analysis	20
2 Experimental	25
2.1 Instrumental	26
2.2 Sample alignment	28
3 Diffraction from a stepped surface of SrTiO₃	31
3.1 SrTiO ₃	32
3.2 Experimental	32
3.3 Diffraction data	33
3.4 Optical constants	36
3.5 Modelling of the spectra	42
3.6 Results and discussion	44
4 Spectroscopy of stripe order in La_{1.8}Sr_{0.2}NiO₄	47
4.1 La _{2-x} Sr _x NiO ₄ system	47
4.2 Experimental	48
4.3 Bulk sensitivity	50
4.4 Spectroscopic analysis	52
4.4.1 Microscopic modeling	55
4.5 Temperature dependence	60
4.6 Discussion	66

5 Spectroscopy of charge and orbital order in Fe₃O₄	67
5.1 Magnetite (Fe ₃ O ₄)	67
5.2 Experimental	69
5.3 Diffraction data	71
5.4 Spectroscopic analysis	71
5.5 Conclusions	75
Summary	77

Introduction

Correlated electron systems, like transition metal oxides (TMO) and rare earth (RE) systems, often display phases of spatially ordered electronic degrees of freedom. The most known one is magnetic order, which is a periodic arrangement of magnetic moments, occurring mostly if atomic sites with partly occupied d - or f -shells are present. A non-ferromagnetic magnetic structure leads to the appearance of additional diffraction peaks (in the magnetic scattering signal), since the unit cell is effectively enlarged. This is the case for instance for various antiferromagnetic structures, including helical magnetic structures in e.g. Dy and Ho metals and multiferroic oxides and can be regarded as the formation of a superstructure with respect to the crystal lattice. Not only direction and size of magnetic moments, but also the valence or orbital occupation can be spatially modulated, leading to the formation of a long-range charge or orbital order. Systems, where such kind of orders have been predicted first are Fe_3O_4 (magnetite) and $\text{La}_{1-x}\text{Ca}_x\text{MnO}_3$. Both compounds are mixed-valent systems, where transition-metal ions have a formally fractional oxidation state; $\text{Fe}^{2.5+}$ on octahedral sites in magnetite and $\text{Mn}^{(3+x)+}$ in $\text{La}_{1-x}\text{Ca}_x\text{MnO}_3$. The occurrence of charge order has been predicted in magnetite by Verwey in 1939 [1]. He explained the sudden drop of electric conductivity in Fe_3O_4 , when cooled below 122 K (the Verwey transition), by the occurrence of charge order, i.e., a periodic arrangement of Fe^{2+} and Fe^{3+} ions leading to the localization of charge carriers. Later, Goodenough demonstrated the complicated interplay between magnetic, orbital and charge degrees of freedom for the $\text{La}_{1-x}\text{Ca}_x\text{MnO}_3$ system [2], where strong variations of magnetic properties with Ca doping were observed [3], suggesting for the first time the existence of orbital order.

Understanding of the ordering of electronic degrees of freedom is important for the study of many of the often spectacular properties in correlated systems, including high-temperature superconductivity and metal-insulator transitions. One famous example for a possible interplay between different electronic degrees of freedom is the so-called stripe order in superconducting cuprates. The strong dependence of magnetic correlation length of $\text{La}_{2-x}\text{Sr}_x\text{CuO}_4$ on doping with Sr, and above all the observation of modulation of the antiferromagnetic structure for $x > 0.05$ [4–7], led to the assumption of a stripe-like superstructure in the system [8–11]. In this model the doped holes form linear charge stripes in the CuO_2 -plane, which work as antiphase domain-walls for the antiferromagnetic order on the Cu^{2+} -sites. The first structural evidence for the existence of such a charge-spin stripe order was found for the closely related Ni compound $\text{La}_{2-x}\text{Sr}_x\text{NiO}_4$, where mutually commensurate charge and spin modulations were observed [12–14].

While magnetic properties of a bulk material can be investigated using neutron

diffraction, an appropriate technique for the identification of orbital and charge order was lacking for a long time. Neutrons interact directly with the atomic nuclei and with magnetic moments. Neutron diffraction is therefore the appropriate technique for investigation of crystalline and magnetic structures. However, since neutrons do not interact with electrons, they cannot reveal phenomena involving charge distribution, as charge and orbital order directly, but only via effects on the crystal structure such as changed bond lengths. Therefore, superstructure reflections observed with neutrons can serve only as indication for the existence of a charge or orbital order, but cannot deliver the direct proof.

Conventional x-rays are directly sensitive to charge, but they interact with all electrons in the material in the same manner. Thus the technique is hardly sensitive to small changes involving only outer-shell electrons of heavier atoms, which are those electrons that determine the electronic properties of a solid, and the only electrons that will participate in the formation of an ordered state. The contrast created by the order may be too small, compared to the core-electrons background, to be detected. For this reason, a diffraction method is needed, which is sensitive to small changes in the configuration of valence electrons, as it is resonant x-ray diffraction.

The first attempt to study orbital order by resonant x-ray diffraction in manganites was made by Murakami et al., at the Mn K -edge ($1s \rightarrow 4p$ transition) in the conventional x-ray range (6540 eV) [15, 16]. They observed a pronounced dependence of the scattered intensity of a "forbidden" reflection on the azimuthal angle of the sample, which they identified with the direct observation of orbital order. This interpretation however received criticism from theory [17, 18], which demonstrated that diffraction studies at the Mn K -edge are not suitable to detect orbital order directly, since the method is predominantly sensitive to lattice distortions, like the accompanying collective Jahn-Teller distortion. In the following Castleton and Altarelli [19] showed that in order to probe the orbital order directly, the scattering process has to involve an excitation into a Mn $3d$ orbital, as is the dominant excitation in resonant diffraction at the Mn $L_{2,3}$ edge ($2p \rightarrow 3d$ transition) in the soft x-ray range (650 eV). The energy dependence of the scattered intensity across the resonance turns out to be so extremely sensitive to the order that no recording of the azimuthal dependence is required to identify it.

Resonant soft x-ray diffraction is therefore a method that has the potential to combine diffraction with spectroscopy. The signal is here sensitive to both; to a long-range order (structure) with a certain periodicity and to the electronic state of the TM-ions. This fact can be used to perform either *spectroscopically-resolved structure study*; through selecting diffraction intensity due to a certain electronic order - or to perform *structurally-resolved spectroscopy study*; since in combination with the appropriate microscopic model the technique is able to reveal the electronic structure of the ordered part of the system.

The first experimental study, applying resonant soft x-ray scattering at transition-metal oxides, was published in 2002 by Abbamonte et. al. [20]. Already before that, Schüßler-Langeheine et al. published soft x-ray diffraction results from a single crystalline Ho metal film at the Ho M_5 resonance [21]. Experimental diffraction studies on electronic order in various transition-metal oxides followed; in manganese-oxides

at the Mn $L_{2,3}$ edge [22–28], copper-oxides at the Cu $L_{2,3}$ and O K edge [29–31], nickel-oxides at the Ni $L_{2,3}$ edge [32, 33], ruthenium-oxide at the Ru $L_{2,3}$ edge [34] and in Fe_3O_4 at the oxygen K edge [35]. Also the magnetic structure of thin films of Ho and Dy metals was studied at the rare earth $M_{4,5}$ resonance [36–38]. Despite the fact that most of these studies use the shape of the spectra for the interpretation of their data, a full spectral analysis of the data in terms of a realistic microscopic theory - as it is state of the art in the closely related x-ray absorption spectroscopy (XAS) - is very rare, showing that the technique is still in its infant state.

This thesis deals with the application of resonant soft x-ray diffraction technique for the investigation of electronic order in transition metal oxides at the TM $L_{2,3}$ edge, trying to obtain a quantitative understanding of the data. The method was therefore first systematically explored through application to a model system, with the emphasis on understanding of how x-ray optical effects have to be taken into account. Two more complex systems were investigated; stripe order in $\text{La}_{1.8}\text{Sr}_{0.2}\text{NiO}_4$ and charge and orbital order in Fe_3O_4 . The main focus of the work is on the spectroscopic potential of the technique, trying to obtain a level of quantitative description of the data. For x-ray absorption spectroscopy (XAS) from transition metal oxides, cluster configuration interaction calculation provides a powerful and realistic microscopic theory. In the frame work of this thesis this cluster theory, which also considers hybridization effects between the TM-ion and the surrounding oxygen ligands, has been applied for the first time to describe resonant diffraction data; previous publications confined themselves to a pure ionic picture in their model calculations [19, 24, 25]. Results of our calculations show indeed that hybridization plays an important role for TMO, due to the strong delocalization of charges over the (TM) O_6 cluster.

In the first chapter of this thesis the principles of resonant soft x-ray diffraction (RSXD) is described, including a description of the optical properties of materials for x-rays. Furthermore the spectroscopic analysis of resonant diffraction data at TM $L_{2,3}$ edges is explained.

The second, experimental chapter describes the experimental setups used within this thesis and gives technical details about the sample preparation.

The third chapter presents diffraction and optical data of the model systems, which were SrTiO_3 single crystals with terraced surfaces. The feasibility and sensitivity of the technique is investigated. The optical constants are obtained across the Ti $L_{2,3}$ resonance. It is shown how optical and diffraction-spectroscopy data are related in an ordered system consisting of electronically identical transition metal ions, serving as a reference for a charge or orbitally ordered system built up of electronically inequivalent TM ions.

In the fourth chapter resonant soft x-ray diffraction data from charge and spin order in $\text{La}_{1.8}\text{Sr}_{0.2}\text{NiO}_4$ are presented. The existence of charge order in $\text{La}_{1-x}\text{Sr}_x\text{NiO}_4$ systems is directly confirmed. From the scattering data the spin canting and the energy splitting between the partially un-occupied e_g states can be determined. A quantitative microscopic analysis of the spectral data delivers a complete picture of the electronic states involved in the stripe structure in nickelates, revealing similarities to cuprates, which appeared absent in XAS data [39].

The fifth chapter presents the results of a resonant soft x-ray diffraction study on magnetite (Fe_3O_4) at the iron $L_{2,3}$ edge. Two reflections are observed, $(0\ 0\ 1/2)$ and $(0\ 0\ 1)$. The $(0\ 0\ 1/2)$ reflection can be clearly assigned to orbital order involving the octahedral Fe^{2+} sites, whereas the $(0\ 0\ 1)$ reflection is due to charge order of the octahedral Fe^{2+} and Fe^{3+} sites.

Chapter 1

Resonant soft x-ray diffraction

Resonant soft x-ray diffraction is an experimental method combining diffraction with spectroscopy. The diffraction signal of a periodic structure is investigated, probing its energy dependence across a selected absorption edge. Due to the strong sensitivity of the spectral shape, very detailed information about the form and the electronic properties of the investigated structure can be obtained.

The energies of soft x-rays lay in the range of 200 - 2000 eV. Resonant excitations taking place in this region are for instance: the oxygen $1s \rightarrow 2p$ (K edge), the transition-metal $2p \rightarrow 3d$ ($L_{2,3}$ edge) and the rare-earth $3d \rightarrow 4f$ ($M_{4,5}$ edge) transition. The energy range is therefore particularly suitable for investigation of transition-metal oxides and rare-earth materials, which display a rich variety of long period electronic superstructures (charge, magnetic and orbital order) matching the soft x-ray wavelengths [40, 41]. The structures investigated in this work were: stepped-surface SrTiO_3 as a model system, charge and spin stripe-order in $\text{La}_{1.8}\text{Sr}_{0.2}\text{NiO}_4$ and charge and orbital order in Fe_3O_4 .

This chapter describes the principles of resonant soft x-ray diffraction. In the first part a few general aspects of x-ray diffraction are outlined, relevant for the technique. The second part treats the resonant interaction of x-rays with atoms. In the third part the optical properties of soft x-rays are described. The connections is made between this macroscopic reaction of matter to x-rays and the atomic picture given in part two. The last part discusses the rich information one can obtain from the spectroscopic analysis of the soft x-ray diffraction signal.

1.1 X-ray diffraction

All experiments were carried out at synchrotron-radiation sources, which provide well-focused, monochromatic and polarized photon beams of very high intensity. A monochromatic electromagnetic wave with a defined polarization direction $\vec{\epsilon}$ can be described, for any fixed moment in time, by the plane wave $\vec{E}(\vec{r}) = \vec{\epsilon} \cdot E_0 \cdot e^{i\vec{k}\vec{r}}$, where \vec{k} is the wavevector and \vec{r} the position vector. If such a wave hits a target potential, it can generate a non-homogeneous spherical wave, which will propagate away from the center of collision. At sufficiently large distance it will have the form $f(\Omega) \cdot \frac{e^{ik'r}}{r}$. The non-scattered part of the incoming wave will be transmitted, continuing its

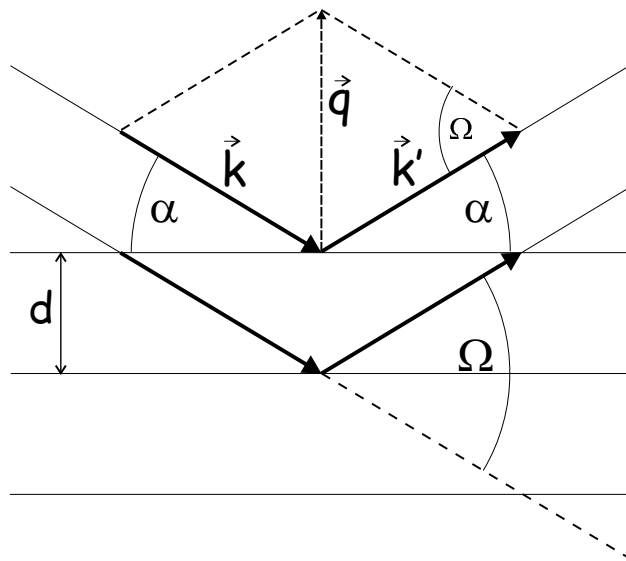


Figure 1.1: Bragg diffraction on a set of parallel crystal planes.

propagation in the direction of incidence. The resulting wave after the scattering process can be approximated through: $\psi(r) \sim e^{i\vec{k}\vec{r}} + f(\Omega) \cdot \frac{e^{i\vec{k}'\vec{r}}}{r}$. All information about the target potential is contained in the scattering amplitude $f(\Omega)$, which is a complex quantity and depends on the angle between the direction of incidence and observation Ω . The quantity accessible through the experiment is $|f(\Omega)|^2$, known as the differential cross-section. Its integration over the solid angle gives the total scattering cross-section σ_{tot} .

In a crystal the x-ray photon beam is scattered on a periodic potential, which is formed by the atomic lattice. Here each electron can be a center of collision and a source of a propagating spherical wave. The scattering amplitude of an elastic process involving a free electron (Thomson scattering) is equal to the classical electron radius $r_0 = \frac{\mu_0 e^2}{4\pi m_e} = 2.82 \cdot 10^{-5} \text{Å}$, also named Thomson scattering length (m_e denotes here the electron mass), multiplied with a polarization factor, namely: $f(\Omega) = -|\vec{\varepsilon}' \cdot \vec{\varepsilon}| \cdot r_0$, where $\vec{\varepsilon}$ and $\vec{\varepsilon}'$ represent the polarization vectors of the incoming and scattered photon (the dagger denotes the complex conjugate). The minus sign indicates that the scattering process involves a phase shift of π .

When the atomic distances in a crystal are comparable with the wavelength of x-rays, the single scattering waves can interfere constructively. Often the so-called kinematical model, which considers only interaction between the spherical parts of the waves is sufficient to describe this process, while interferences between these waves and the incident and transmitted wave are neglected. The later effects need to be included only for extremely good crystals. [42].

Constructive interference occurs when the well-known Laue-condition, or for an elastic process the equivalent Bragg's law, is fulfilled. Both conditions can be formulated in terms of the so-called scattering vector \vec{q} . The scattering vector gives the momentum transfer of a photon on the crystal lattice and is defined as $\vec{q} = \vec{k}' - \vec{k}$, with \vec{k} and \vec{k}' being the wave vectors of the incident and scattered beam respectively

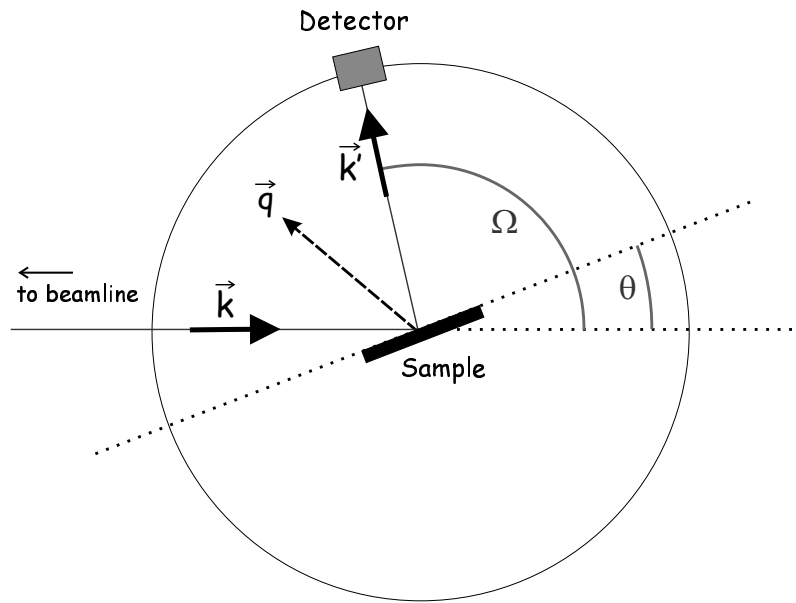


Figure 1.2: Geometry of a two-circle diffractometer.

(see Fig. 1.1 and 1.2). The Laue-condition is fulfilled when \vec{q} is equal to a reciprocal lattice vector \vec{G} , so that: $\vec{q} = \vec{G}$.

1.1.1 Geometry

Bragg diffraction is an elastic process, where the incident beam can be considered as reflected on a set of crystal planes (Fig. 1.1). For certain Bragg-angles α , the reflected waves interfere constructively. When the energy of the photons is conserved ($k = k' = \frac{2\pi}{\lambda}$), the absolute value of \vec{q} is equal: $q = \frac{4\pi}{\lambda} \sin(\frac{\Omega}{2})$, with Ω being the already introduced scattering angle $\sphericalangle(\vec{k}, \vec{k}')$. Applying the Laue condition and d being the distance between the crystal planes:

$$m\lambda = 2d \sin(\frac{\Omega}{2}), \quad m \in \mathbb{N}, \quad (1.1)$$

This is the well-known Bragg's law, here expressed in terms of the scattering angle Ω . The scattering angle is related to the Bragg-angle α (the angle between the incident/diffracted beam and the crystal plane) as follows: $\Omega = 2 \cdot \alpha$. The quantity Ω is directly accessible by the experiment.

The geometry used in x-ray diffraction experiments is shown in Fig. 1.2. The incident beam is fixed by the position of the beamline. To find a Bragg reflection, the sample and the detector are rotated. In the simplest set-up, there is one axis of rotation for both, the sample and detector, which is oriented perpendicularly to the direction of incidence. The angle between the incident beam and the sample surface is named θ and the angle between the incident beam and detector is exactly equal the scattering angle Ω . The scattering vector \vec{q} points in between the direction of incidence and diffraction. The surface of the sample is placed in the center of rotation.

1.1.2 Structure factor

The Laue or Bragg conditions give the angle, under which constructive interferences might occur. The intensity of the diffraction peak, and whether a peak is actually observed or not, depends on the structure of the unit cell of the crystal and is described in terms of the form factor f_S .

The electric fields of the incident and diffracted beam are related through the scattering amplitude: $E_{out} \propto F \cdot E_{in}$. In the kinematical approximation F is a superposition of the scattering amplitudes of the single spherical waves, weighted with the appropriate phase factors. The phase relation between two coherently scattered spherical waves is given through the scattering vector \vec{q} and the distance between their origins \vec{r} , namely: $\Delta\phi = \vec{q} \cdot \vec{r}$. Since any point in space can be chosen as the reference point, also the positions of the two points $\vec{r}_{1,2}$ can be directly used (this will have no influence on the intensity). The total scattering amplitude is then equal: $f_1 \cdot e^{i\vec{q}\vec{r}_1} + f_2 \cdot e^{i\vec{q}\vec{r}_2}$, where $f_{1,2}$ are the scattering amplitudes of the two sites.

An analogous sum can be formulated for the crystal lattice. The summation is performed over the atomic sites, the scattering amplitude of each atom being expressed through $r_0 \cdot f$, where f is here the atomic structure factor.

The scattering amplitude of a crystal is equal:

$$F = r_0 \underbrace{\sum_j f_j e^{i\vec{q}\vec{r}_j}}_{\text{all atoms}} = r_0 \underbrace{\sum_n e^{i\vec{q}\vec{R}_n}}_{\text{lattice points}} \underbrace{\sum_l f_l e^{i\vec{q}\vec{r}_l}}_{\text{1 unit cell}}, \quad (1.2)$$

The summation is performed either over all coherently scattered atoms, or by making use of the periodical structure of the crystal, first over one primitive unit cell of the crystal and then over the lattice points. The vectors \vec{r}_j in the first sum represent the positions of the atoms with respect to an origin in the crystal. In the right-hand side expression \vec{R}_n represent the crystal lattice vectors and \vec{r}_l the positions of the atoms with respect to an origin in the unit cell. The Laue-condition is fulfilled when $e^{i\vec{q}\vec{R}_n} = e^{2\pi i} = 1$ and:

$$F = N r_0 \sum_l f_l e^{i\vec{q}\vec{r}_l} \equiv N r_0 f_S, \quad (1.3)$$

f_S is the already mentioned structure factor, the q -dependent scattering amplitude of one unit cell and N the number of coherently scattering unit cells.

Here are some examples for the structure factor:

1. If the primitive unit cell consists of only one atom, the structure factor will be equal to the form factor f , independent on the scattering vector \vec{q} (as long as the Laue condition applies).
2. If the unit cell consists of two atoms of the same kind, spaced half a lattice vector apart, e.g. $a/2$, the structure factor will be equal to $f_S = f(1 + e^{i \cdot q_a \cdot \frac{a}{2}})$. If the component of q along the a -direction is exactly equal $\frac{2\pi}{a}$, then the phase factor of the second atom will be shifted by 180 in respect to the first atom and the sum will disappear, producing no diffraction signal.
3. If the unit cell consists of two different atoms, A and B , spaced as in the example above; $a/2$ apart, and if again $q_a = \frac{2\pi}{a}$, then: $f_S = f_A + f_B \cdot e^{i \cdot q_a \cdot \frac{a}{2}} =$

$f_A - f_B$. In this case the structure factor is equal to the difference of the two atomic form factors.

The aim of this work is the investigation not of crystal structures, but of superstructures formed within the chemical crystal structure. For the systems we investigated the crystal unit cells show a periodical spacial variation of their structure factors, due e.g. to a magnetic order within the system, or generally to differences in the electronic state of the corresponding atoms. In this case the real unit cell of the crystal is effectively enlarged. Since the above notation is universal, it can be also adopted to describe the scattering amplitude of such superstructures, as well.

1.1.3 Scattering volume

According to Eq. (1.2), the diffraction amplitude is proportional to the number of coherently scattering unit cells: $N = n_x n_y n_z$ ($n_{x,y,z}$ denoting the number of coherently scattering unit cells along one crystal direction). If the entire scattering volume scatters coherently, the height of a diffraction peak will grow with N^2 (while the width along one direction will decrease with $1/n_{x,y,z}$). This is the case if the correlation length of the ordered system extends over the investigated scattering volume. Otherwise the peak height will be proportional to the number of domains in the volume.

In bulk samples, due to change of penetration depth of photons with energy, the scattering volume varies across the resonance. Stronger absorption leads here to a smaller N and a decrease of the diffraction signal. For non-specular geometry the probed volume depends additionally on the relation between the angle of incidence and diffraction, since the incident and diffracted beam have to cover unequal distances in matter. Is $\theta' \equiv \Omega - \theta$, the angle between the diffracted beam and the sample surface, smaller than the incidence angle θ , then the path of the scattered photons in matter will be on average larger than the path for the incoming photons - and vice versa. The effective volume is proportional to [43]:

$$V_{eff} \propto \frac{1}{\sigma_{tot}} \frac{\sin \theta'}{\sin \theta' + \sin \theta} \quad (1.4)$$

where σ_{tot} denotes the total scattering cross-section.

The scattering volume of thin films is limited by the sample thickness and therefore does not change much across a resonance [38].

1.2 Atomic form factor

The atomic form factors describe the response of atoms to the electromagnetic x-ray field and depend on the kind of interaction between the electrons and photons. In a general expression they can be written as [42]:

$$\hat{f}(\vec{q}, \omega) = f^0(\vec{q}) + \hat{f}'(\omega) + i\hat{f}''(\omega) \quad (1.5)$$

$f^0(\vec{q})$ is an isotropic, non-resonant term. The resonant contributions; $\hat{f}'(\omega)$ and $\hat{f}''(\omega)$, also known as dispersion or anomalous corrections, are (3×3) tensors [44, 45].

Their symmetry is given by the local symmetry at the scattering atom.

The isotropic and resonant contributions in (1.5) can be derived through solving the equation of motion of bound electrons in an alternating electromagnetic field. The Hamiltonian of the system consists of an unperturbed term $\hat{H}_0 = \hat{p}^2/2m + \hat{U}(\vec{r})$, and of interaction terms with the x-ray field, which are either linear or quadratic in the vector potential of the photon field \vec{A} , so that: $\hat{H} = \hat{H}_0 + \hat{H}_1(\vec{A}) + \hat{H}_2(\vec{A}^2)$ [46, 47]. Since \vec{A} is linear in $c^\dagger(\vec{k})$ and $c(\vec{k})$; the operator of photon creation and annihilation, perturbation theory yields for the scattering probability of a photon:

$$w = \langle f|H_2|i\rangle + \sum_m \frac{\langle f|H_1^\dagger|m\rangle\langle m|H_1|i\rangle}{E_i + \hbar\omega - E_m} \delta(E_f - E_i) \quad (1.6)$$

$|i\rangle, |m\rangle, |f\rangle$ denote the initial, intermediate and final states of the electron system and E_i, E_m, E_f the corresponding energies. The first order term, corresponding to the isotropic, non-resonant contribution in (1.5), is determined by the Fourier transforms of the charge and spin distribution [46]. The resonant contributions \hat{f}' and \hat{f}'' are given by the second order terms.

1.2.1 Isotropic terms

According to Ref. [46], the first order term in (1.6) can be split into a charge and magnetic contribution. In the same way f^0 in (1.5) can be separated into a charge: f_C^0 and magnetic: f_M^0 term. The charge term is the basis of e.g. hard x-ray scattering experiments. The photons interact here with the charge density $\rho(\vec{r})$ at the atomic site [42]:

$$f_C^0(\vec{q}) = \int_{Atom} \rho(\vec{r}) e^{i\vec{q}\vec{r}} d\vec{r}^3 \quad (1.7)$$

The electrons are accelerated by the photon field as if they were free; like in the case of Thomson scattering. The \vec{q} -dependence is given through the phase relations between the charges. The interaction is of a pure electric nature, and is further due in the first order to the dipole field term: E1. Without any momentum transfer (if $\vec{q} = 0$), f_C^0 is equal to the total number of electrons on the atomic site; $N = Z - V$ (Z ordination number and V valence). The values of f_C^0 for free atoms and ions are tabulated in the International Tables of Crystallography [48]. The polarization dependence of the scattering process is the same one, as for a free electron (Section 1.1): $I \propto |\vec{\epsilon}^{\dagger} \cdot \vec{\epsilon}|^2$.

The expression for the non-resonant magnetic term is analogous to (1.7), but here the density of the magnetic moments $\mu(\vec{r})$ is considered:

$$f_M^0(\vec{q}) = \frac{\hbar\omega}{m_e c^2} \int_{Atom} \mu(\vec{r}) e^{i\vec{q}\vec{r}} d\vec{r}^3 \quad (1.8)$$

This interaction is of magnetic nature, since the spin density interacts with the magnetic field of the photon field (in the first order B1). The factor $\frac{\hbar\omega}{m_e c^2}$ ($\sim 10^{-4}$) makes the scattering process very weak. The different polarization dependence from

charge-density scattering: $I \propto |(\vec{\varepsilon}^i \times \vec{\varepsilon}) \cdot \vec{\mu}|^2$, provides however a way to separate the magnetic-density signal from the charge-density signal [49].

In the following; only the charge density term (f_C^0) will be considered when referring to f^0 .

1.2.2 Resonant terms

The resonant terms take into account the bounding of electrons to atoms. To understand their energy dependence, we look directly at the electronic state of the entire atomic site. If ψ and φ are two electronic states, then under the influence of an x-ray electric field a transition $\psi \rightleftharpoons \varphi$ can be stimulated. The probability for the $\psi \rightarrow \varphi$ transition is equal to $\langle \varphi | \hat{O} | \psi \rangle$, with \hat{O} being the transition operator. For resonances in the soft x-ray range, the dominating channel is the electric dipole-allowed E1 process. Therefore in the following we confine ourselves to electric dipole (E1) transitions, neglecting all other excitations, including the magnetic dipole (B1).

The electric dipole operator is defined as: $\hat{P} = -e \sum_n \hat{r}_n = -e \sum_n (\hat{x}_n + \hat{y}_n + \hat{z}_n)$, with e being the elementary charge and \hat{r}_n the position operator for all charges in respect to the atomic nucleus. The transition probability $\langle \varphi | \hat{P} | \psi \rangle$ corresponds to the spatial overlap of the wave functions ψ and φ . According to (1.6), the resonant diffraction term is described by a second order perturbation processes, where the atom is virtually excited into an intermediate state. In our case the occurring transition is $\psi \rightarrow \varphi \rightarrow \psi$, with φ being the intermediate state and ψ both; the initial and the final state. This process is coherent and therefore an observation of a Bragg-reflection is possible.

Since the functions ψ and φ describe the entire electronic state of the atom, the transition probability at resonance is sensitive to both, to the charge distribution; including the valence and orbital orientation, and to the magnetic (spin and orbital) moments at the atom [50]. This is in a clear contrast to E1-scattering outside resonance, where the signal is sensitive only to charge density.

The interaction between an electron and the electric part of the photon beam is given through: $-\frac{e\vec{A}\vec{p}}{m_e c}$, with \vec{p} the momentum operator. If we use an adequate set of basis functions, the expression for the resonant term $\hat{f}(\omega) = \hat{f}'(\omega) + i\hat{f}''(\omega)$ becomes:

$$\hat{f}(\omega) = k^2 \sum_m \frac{\langle n | \hat{P}^t | m \rangle \langle m | \hat{P} | n \rangle}{E_n + \hbar\omega - E_m} \delta(E_n - E_m), \quad (1.9)$$

$|n\rangle$ is the electronic ground state with energy E_n , $\hbar\omega$ the photon energy, $|m\rangle$ are the intermediate states with energies E_m and \hat{P}^t the inverse of the dipole operator. The summation is performed over all transition-allowed states (see Section 1.4). The expression can be also written as [51]:

$$\hat{f}(\omega) = k^2 \langle n | \hat{P}^t \frac{1}{E_n + \hbar\omega - \sum_m \hat{H}_m + i\hat{\Gamma}_m/2} \hat{P} | n \rangle, \quad (1.10)$$

Here \hat{H}_m represent the Hamiltonian-operators of the intermediate states and $\hat{\Gamma}_m$ the lifetime-broadening operators.

As already mentioned above, the scattering process at resonance is anisotropic. The anisotropy is determined by the symmetry of the unoccupied atomic states, involving charge and magnetic degrees of freedom, which can be connected to / or accompanied by an anisotropy of the environment at the atomic site, e.g. due to crystal field and exchange couplings [44]. During the scattering process the polarization of the photon might be also changed, leading to non-diagonal elements in the transition matrix. The different anisotropy factors, and especially the charge and magnetic properties of the scattering ions, will contribute in a different way to the symmetry of $\hat{f}(\omega)$ [47, 50, 52–54] and can be therefore in principle separated.

The total scattering intensity of a resonant E1-process is proportional to:

$$I(\omega, \vec{\varepsilon}, \vec{\varepsilon}') \propto |\vec{\varepsilon}'^\dagger \cdot \hat{f}(\omega) \cdot \vec{\varepsilon}|^2 \quad (1.11)$$

1.3 X-ray optics

The macroscopic optical properties of a material are described in terms of the dimensionless refractive index n . Since the index of refraction in the x-ray regime is very close to unity, the following expression is normally used:

$$n = 1 - \delta + i\beta \quad (1.12)$$

The quantities δ and β are referred to as optical constants and in the conventional hard x-ray regime they are of the order $10^{-5} - 10^{-8}$. In the soft x-ray range they can reach values up to 10^{-2} at resonance (Chapter 3.4). It is interesting to notice that in the hard x-ray regime - where the energy of photons lies above the most transition edges - δ is always positive, causing the real part of n being smaller than one. In the optical regime, on the contrary, the refractive index is always larger than one, since the photon energy is lower than any transition edge.

The atomic form factors describe the response of atoms to the electromagnetic x-ray field. The scattering amplitudes in the forward scattering direction (without momentum transfer; $\vec{q} = 0$) of an atomic system can be therefore used to describe the optical properties of the system at the atomic level. For a material consisting of one kind of homogeneously distributed non-magnetic atoms, with the form factor f , the refractive index n would be [42]:

$$n(\omega) \equiv 1 - \frac{2\pi\rho_a}{k^2} r_0 f(\omega)_{q=0} = 1 - \frac{2\pi\rho_a}{k^2} r_0 \{f_{q=0}^0 + f'(\omega) + if''(\omega)\} \quad (1.13)$$

Here $\rho_a = \frac{\rho N_A}{M}$ is the atomic mass density (ρ mass density, N_A Avogadro-constant, M atomic mass), r_0 the Thomson scattering length and $k = \frac{2\pi}{\lambda} = \frac{\omega}{c}$ the wave number in vacuum. Like the scattering amplitude, the index of refraction, n , is strongly energy dependent across a resonance. For a non-isotropic system, where the optical properties are polarization-dependent, it has to be expressed through a

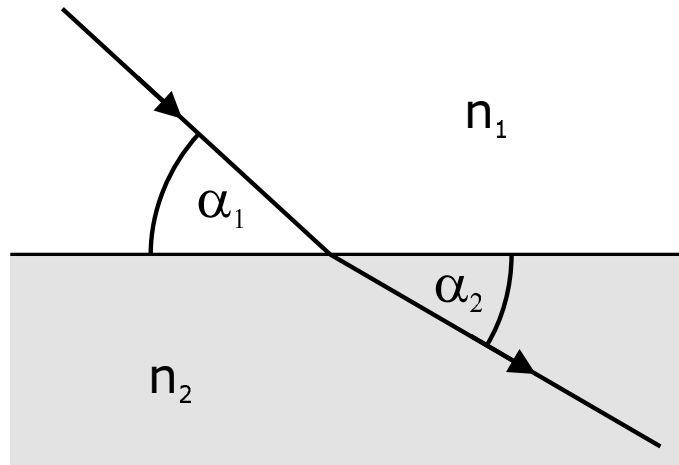


Figure 1.3: Refraction at the border of two media. When x-rays enter matter, the propagation angle becomes usually more shallow.

(3×3) tensor. δ corresponds to the real part of the scattering amplitude of the homogeneous system:

$$\delta(\omega) \equiv \frac{2\pi\rho_a}{k^2} r_0(f^0 + f'(\omega)) \quad (1.14)$$

and β relates to its imaginary part:

$$\beta(\omega) \equiv -\frac{2\pi\rho_a}{k^2} r_0 f''(\omega). \quad (1.15)$$

For conventional x-rays outside resonance f' and f'' are negligible small and therefore n is approximately equal:

$$n \approx 1 - \delta \approx 1 - \frac{2\pi\rho_a}{k^2} \cdot r_0 f^0. \quad (1.16)$$

The index of refraction depends here only on the average number of electrons pro atomic site (or volume element), since $\delta \sim N = Z - V$ (Z : ordination number and V : valency). The propagation direction of the x-ray beam in the material is more shallow than in vacuum, since n is smaller than unity (the medium is optically less dense than vacuum). This leads to the occurrence of total external reflection for angles smaller than the critical angle: $\alpha_c = \arccos \sqrt{1 - \delta}$. In this case the electromagnetic wave cannot penetrate the second medium and the entire intensity is reflected. This effect occurs also for soft x-rays, if $\delta > 0$.

1.3.1 Refraction

At the border of two media the propagation velocity of an electromagnetic wave changes, leading to refraction. The ratio of velocities in these media is equal to the inverse of the ratio of their refractive indices, as is known from electrodynamics [55]:

$$\frac{c_1}{c_2} = \frac{\lambda_1}{\lambda_2} = \frac{n_2}{n_1} \quad (1.17)$$

Here $\lambda_{1,2}$ are the corresponding wavelengths. From the continuity of the tangential component of the electric field \vec{E} and its derivative across the border Snell's law can be deduced:

$$\frac{\cos \alpha_1}{\cos \alpha_2} = \frac{n_2}{n_1} \quad (1.18)$$

with α_1 being the angle of incidence and α_2 the angle of refraction in respect to the tangential of the surface (Fig.1.3). This notation applies if both media are isotropic and homogeneous, so that $n_{1,2}$ are position-independent scalars. If the first medium is vacuum, then $n_1 = 1$ and n_2 can be set to n . The refractive angle becomes:

$$\cos \alpha_2 = \frac{\cos \alpha_1}{n} \quad (1.19)$$

In soft x-ray regime n is a complex number, leading to a complex cosine. To understand the meaning of the complex $\cos \alpha_2$ we look at the wave vector of the refracted wave $e^{i\vec{k}\vec{r}}$ in matter. We separate \vec{k} into contributions parallel (k_{\parallel}) and perpendicular (k_{\perp}) to the tangential of the surface. Applying (1.16) and (1.18) the parallel component of \vec{k} is equal:

$$k_{\parallel} = \frac{2\pi}{\lambda_2} \cdot \cos \alpha_2 = \frac{2\pi}{\lambda_1} \cdot \cos \alpha_1 = k_{\parallel vac} \quad (1.20)$$

and the perpendicular component:

$$k_{\perp} = \frac{2\pi}{\lambda_2} \cdot \sin \alpha_2 = \frac{2\pi}{\lambda_1} \cdot \sqrt{n^2 - \cos^2 \alpha_1} \quad (1.21)$$

The component parallel to the surface does not change through the diffraction process, since the change of wavelength is exactly compensated by the change of the refraction angle. Only the perpendicular component k_{\perp} changes. If the angle of incidence is normal ($\alpha_1 = 90^\circ$):

$$k_{\perp} = \frac{2\pi}{\lambda_2} = \frac{2\pi}{\lambda_1} \cdot n = n \cdot k_{\perp vac} \quad (1.22)$$

and $\vec{k} = n \cdot \vec{k}_{vac}$. In this case the optical constant δ defines the change in wavelength, whereas β is responsible for an exponential decrease of the electric field with depth z :

$$E(z) = E_0 \cdot e^{-\beta \cdot k \cdot z} e^{i(1-\delta) \cdot k \cdot z} \quad (1.23)$$

For an arbitrary incidence angle, α_1 , since the expression in (1.20) is a square-root of a complex number, the change of the wavelength in medium will depend to some extent on the imaginary constant β and the damping of the electric field on the real constant δ . However, if the incidence angle is steep enough, the expression for k_{\perp} can be simplified. Since $\delta, \beta \ll 1$, their quadratic contributions in n^2 might be neglected, so that: $\sqrt{n^2 - \cos^2 \alpha_1} \approx \sqrt{\sin^2 \alpha_1 - 2\delta + 2i\beta}$. Now, expanding $\sin(\alpha_1)(1 - \frac{2(\delta-i\beta)}{\sin^2 \alpha_1})^{1/2}$ in the binomial series and taking into account the first two terms (valid if $\frac{2|\delta+i\beta|}{\sin^2 \alpha_1} \ll 1$):

$$k_{\perp} \approx \frac{2\pi}{\lambda_1} \cdot \sin \alpha_1 - \frac{2\pi}{\lambda_1} \frac{\delta}{\sin \alpha_1} + i \cdot \frac{2\pi}{\lambda_1} \frac{\beta}{\sin \alpha_1} \quad (1.24)$$

The influence of β on the real part of k_{\perp} and of δ on the imaginary part of k_{\perp} is in this case negligible small. For positive δ , k_{\perp} is smaller than $k_{\perp vac}$ and the propagation angle in matter is more shallow. For normal incidence the expression (1.24) agrees with (1.22).

In the SrTiO₃-system, the norm $\sqrt{\delta^2 + \beta^2}$ reaches values up to 0.013 at the Ti $L_{2,3}$ resonance (see Section 3.4), meaning that the mixing of the real and imaginary terms might occur for angles smaller than 30 deg. Outside resonance $\sqrt{\delta^2 + \beta^2}$ is however not larger than 0.003.

1.3.2 Reflectivity

While Snell's law describes the propagation direction of a wave refracted at the border of two isotropic media, the intensity of the refracted (transmitted) and reflected part of the wave is given by Fresnel equations. If the first medium is vacuum and the second a non-magnetic material, the amplitude of the reflected part of the wave for the polarization direction parallel to the scattering plane (π polarization) is equal [56]:

$$E_{\pi}(\alpha, n) = E_0 \cdot \frac{n^2 \sin \alpha - \sqrt{n^2 - \cos^2 \alpha}}{n^2 \sin \alpha + \sqrt{n^2 - \cos^2 \alpha}} \quad (1.25)$$

while for polarization perpendicular to the scattering plane (σ polarization):

$$E_{\sigma}(\alpha, n) = E_0 \cdot \frac{\sin \alpha - \sqrt{n^2 - \cos^2 \alpha}}{\sin \alpha + \sqrt{n^2 - \cos^2 \alpha}}. \quad (1.26)$$

E_0 is the electric field of the incident wave and α the angle of incidence in respect to the surface normal. Fresnel equations are valid also in the range of total reflection, where Snell's law does not apply.

1.3.3 Absorption

Absorption leads to attenuation of the signal in the medium. According to the empirical Beer-Lambert law, the amount of light absorbed at each layer of a homogeneous medium is the same, causing an exponential decrease of intensity with depth. This can be described in terms of the linear absorption coefficient $\mu = \rho_a \sigma_a$ (ρ_a atomic mass density, σ_a absorption cross section). For normal angle of incidence the photon intensity at depth z will be equal to: $I(z) = I_0 \cdot e^{-\mu(\omega)z}$, with I_0 being the incident intensity. The photon penetration depth Λ is the reciprocal of μ .

According to (1.23), the atomic quantity μ must be related to the macroscopic constant β as follows: $\beta(\omega) = \frac{\mu(\omega)}{2k}$, with $k = \frac{2\pi}{\lambda} = \frac{\omega}{c}$ being the wave number in vacuum. This is in accordance to the Optical Theorem, which is valid for any scattering process in the forward scattering direction ($\vec{q} = 0$) [57]:

$$-r_0 \cdot f''(\omega) = \frac{k}{4\pi} \cdot \sigma_a(\omega). \quad (1.27)$$

The law says that the absorption cross section $\sigma_a(\omega)$ of a scattering process (which corresponds to the total scattering cross section) is proportional to the imaginary part of the scattering length. For photons σ_a can be measured directly using x-ray absorption spectroscopy (XAS).

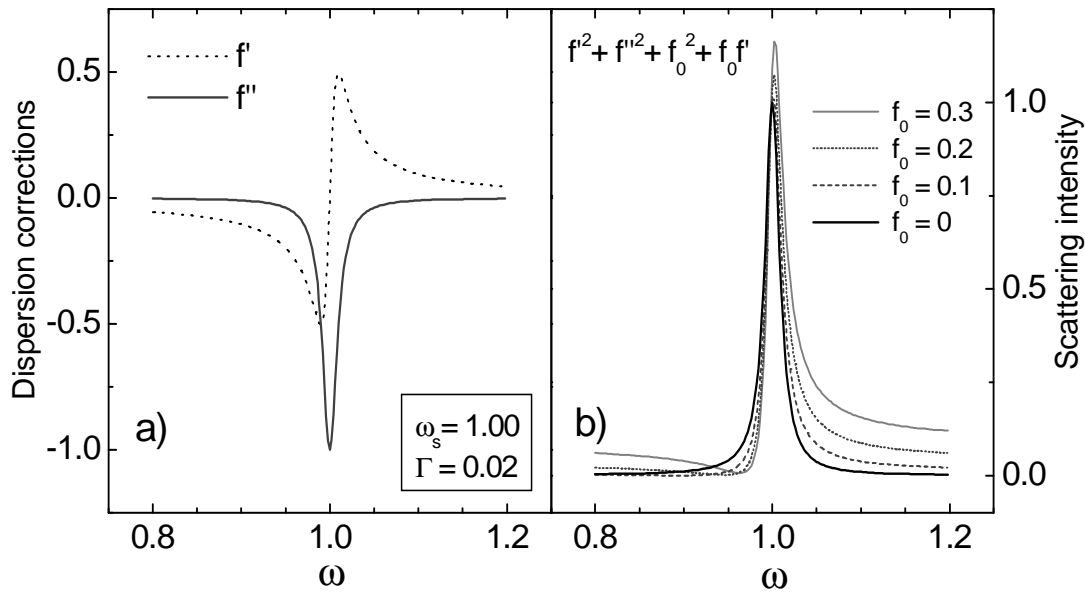


Figure 1.4: Single harmonic oscillator at resonance; resonant contributions to the scattering amplitude: f' and f'' (a) and the scattering intensity (b). In the shown example the resonance energy ω_s was set to unity and $\Gamma = \omega_s/50$ (Γ : full-width half maximum).

1.4 Spectroscopic analysis

In a simple approximation an electronic excitation can be described as a single harmonic oscillator. The resonant parts of the scattering amplitude will then have a similar energy dependence as shown in Fig. 1.4a); the imaginary part f'' being a negative Lorentzian with the maximum positioned at the resonance energy ω_s (here set to unity) and the width Γ (full-width half maximum) determined by the lifetime of the excited state. The real part f' of the response function is the Kramers-Kronig transformed of f'' . The absorption signal of a single oscillator is proportional to $-f''/\omega$, according to (1.27), which has approximately the shape of a Lorentzian too, since in realistic cases $\Gamma \gg \omega_s$. In Fig. 1.4 Γ was set to $\omega_s/50$.

According to (1.5) the scattering intensity at resonance is equal to: $f'^2 + f''^2 + f_0 f' + f_0^2$. Since the non-resonant, isotropic term f_0 varies only slowly with energy, f_0^2 has almost no influence on the line shape of the spectrum. However the interference term $f_0 f'$ cannot be neglected. Fig. 1.4b) shows the scattering intensity for different ratios of f_0 and f''_{max} , the peak value of the imaginary part. The interference term leads to an asymmetry in the line shape, already if f_0 is ten times smaller than f''_{max} . For a vanishing f_0 the spectrum would have a Lorentzian shape.

Fig. 1.5 displays the coherent scattering intensity of two oscillators, which have the same strength and lifetime broadening, but slightly different resonance energies, so that: $f_A(\omega) = f_B(\omega + \Delta\omega)$. While the absorption spectrum of this system will be just the sum of two Lorentzian-like functions (indicated by the gray lines), the coherent signal will depend strongly on $\Delta\omega$, the phase relation between the two oscillators. The curves in Fig. 1.5 represent two cases, (1): $\Delta\omega = 2\pi$, the two

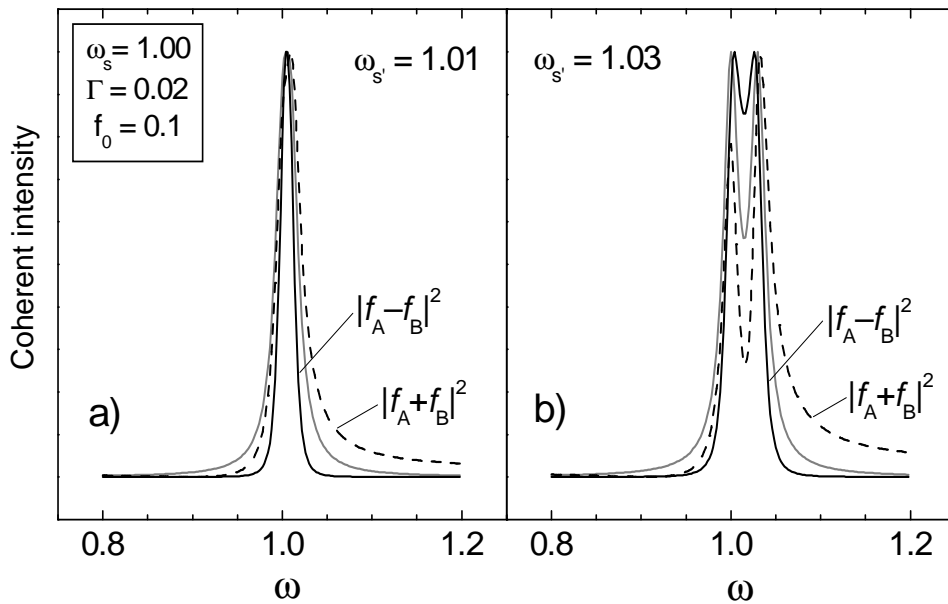


Figure 1.5: Coherent intensity of two oscillators at resonance; oscillating in-phase (dashed lines) and opposite-phase (solid lines). The oscillators have the same strength and width, but slightly different resonance energies; shifted either by $\Gamma/2$ (a) or by $3\Gamma/2$ (b) (Γ : full width half maximum). The gray line in each diagram is the incoherent sum $f''_A + f''_B$, representing the absorption signal.

oscillators resonate in-phase (dashed lines) and the coherent intensity is equal to $|f_A + f_B|^2$, (2): $\Delta\omega = \pi$, the two oscillators are opposite-phase (solid lines) and the coherent intensity is equal to $|f_A - f_B|^2$. The two examples represent a realistic scenario for a mixed-valent system, which contains two similar atomic sites A and B with a slightly different valence. A homogeneous distribution of A and B will always lead to a diffraction signal similar to example (1), where the coherent intensity is equal to the squared sum of the two atomic form factors f_A and f_B . On the contrary, an inhomogeneous distribution of A and B (= charge order), will lead to a diffraction signal with the structure factor given by the difference of f_A and f_B , as in case (2). Fig. 1.5a) demonstrates a situation where: $\Delta\omega_s = \Gamma/2$, so that the energy shift between the two resonances is too small to be resolved. In Fig. 1.5b) the energy shift is larger than the peak width: $\Delta\omega_s = 3\Gamma/2$, leading to a two-peak structure.

The opposite-phase resonating oscillators (black solid lines) show in both diagrams a symmetric line shape and a very sharp resonance, which is clearly steeper than the absorption signal (gray line). By contrast, the curves simulating the in-phase oscillators (dashed lines) are broader and non-symmetric. The reason for this asymmetry is the contribution of the already mentioned interference term; $f_0(f'_A + f'_B)$, which vanishes in the case of two equally strong opposite-phase oscillators, but does not vanish for the oscillators in-phase. In the shown examples the ratio $\frac{f_0}{f''_{max}}$ was set to 0.1.

Generally an atom at resonance behaves like an ensemble of harmonic oscillators, rather than like a single oscillator. This is due to multiplet effects, which lift the

degeneracy of electronic states, belonging to the same configuration. The $2p^5 3d^m$ configuration, which describes an excited $3d$ atom after a $2p \rightarrow 3d$ transition, consist of $\frac{6 \cdot 10!}{m!(10-m)!}$ states, counting all possible permutations for the occupation of the p and d orbitals. This number can be quite large and the single electronic states within this ensemble will be more or less spread in energy, depending on the spatial symmetry at the atomic site. An atomic spectrum can therefore consist of many resonance lines. Fortunately, the actually allowed atomic transitions are considerably limited through selection rules, which depend on the experimental geometry. The dipole selection rules are:

$$\begin{aligned} \Delta l &= \pm 1 & \Delta L &= \pm 1 \\ \Delta s &= \pm 1, 0 & \Delta S &= \pm 1, 0 \\ \Delta j &= \pm 1, 0 & \Delta J &= \pm 1, 0 \end{aligned} \quad (1.28)$$

with l, s, j being the one-electron quantum numbers for the orbital, spin and total angular momentum, respectively, and L, S, J the corresponding atomic quantum numbers.

Selection rules are very crucial for spectroscopy. On the one hand they decisively simplify the form of the spectra. On the other hand they bring about that the set of the permitted excited states is unique for a certain electronic initial state. This makes spectroscopy extremely sensitive to the electronic properties of the resonant atom. Any change in the ground state has a visible impact on the form of the spectrum. This allows for a very accurate determination of the electronic state of the investigated system.

This fact has been already successfully applied in the analysis of x-ray absorption spectroscopy (XAS) data of several TMO-systems at the TM $L_{2,3}$ and O K edges. The credit for this achievement goes to large extend to the availability of an appropriate powerful theoretical tool; full-multiplet cluster model calculation, which allows for a precise estimation of the electronic state of transition-metal oxides from spectroscopy data [58–60]. Making use of this approach the electronic structure of several transition-metal oxides could be obtained to great detail [61].

The approach of cluster modeling comes from chemistry (ligand field theory) and was originally developed to describe the electronic structure of transition-metal complexes. In these compounds, a metal-ion, is surrounded by an arrangement of non-metallic ions (ligands), generating an electrostatic field effecting the central ion. A similar situation is found in crystals consisting of such units; and where the charge carriers are well confined to a cluster. Transition-metal oxides are particularly suitable systems for this approach. In the ground state the charge carriers are well localized within the TMO_n cluster. The electronic state can be already well described by taking into account the TM $2p$ and $3d$ electrons and the oxygen $2p$ electrons, including the ligand crystal field at the TM site. For crystals with cubic (O_h) symmetry there are 6 oxygen ligands arranged on an octahedron (tetrahedron) around the metal. An excitation like the $2p \rightarrow 3d$ transition on the metal ion leads to the formation of a localized exciton. This electronic transition can be therefore entirely modelled by means of the cluster approach. The link between the scattering

amplitude and the electronic state of an atomic site is given through (1.9), (1.10), the necessary set of parameters can be extracted from Ref. [59, 62].

To compare the signals measured with soft x-ray absorption spectroscopy (XAS) and resonant soft x-ray diffraction (RSXD), we introduce the expression $\tilde{f}(\omega)$, denoting the atomic scattering amplitude of an electric dipole (E1) transition:

$$\tilde{f}(\omega) \equiv \vec{\varepsilon}'^\dagger \cdot \hat{f}(\omega) \cdot \vec{\varepsilon}, \quad (1.29)$$

where $\vec{\varepsilon}$ represents the polarization unit vector of the incoming and $\vec{\varepsilon}'^\dagger$ the complex conjugate of the scattered photons and $\hat{f}(\omega)$ the atomic form factor. An absorption signal is proportional to the sum of the imaginary parts \tilde{f}_n'' of all “atomic species”, each weighted depending on the frequency of occurrence a_n in the compound:

$$I_{XAS}(\omega) \propto -\frac{1}{\omega} \sum_n a_n \tilde{f}_n''(\omega) \quad (1.30)$$

This signal is sensitive to all atomic sites at resonance in the same manner and delivers therefore the average optical information about the electronic state of the entire system. In contrast, the diffraction signal is more selective:

$$I_{RSXD}(\omega) \propto \left| \sum_{u. \text{ cell}} e^{i\vec{q}\vec{r}_j} (\tilde{f}^0 + \tilde{f}_j'(\omega) + i\tilde{f}_j''(\omega)) \right|^2 \quad (1.31)$$

This summation is performed only over atomic sites belonging to one unit cell of the investigated structure, where the relative weights are determined by the phase relations between the single atoms. This signal is therefore a result of a coherent process, and it is sensitive only to a long-range order with a certain periodicity, where the investigated structure might be either the crystal structure, or a superstructure. The measured quantity is the squared sum of the contributing atomic form factors.

The spectral shape of a resonant soft x-ray diffraction signal depends exclusively on the electronic state of the atomic sites directly involved in the formation of the investigated order, in contrast to an absorption signal. The technique is therefore especially suitable for the study of mixed-valent systems displaying phases of electronic order.

Chapter 2

Experimental

Soft x-rays are low energy x-rays with energies between 200 - 2000 eV. The absorption cross section of soft x-rays in air is very high, requiring the whole diffractometer to be inside vacuum. In materials the soft x-ray mean free path is several 10 nm even at resonances (see section 3.4), making the technique only moderately surface sensitive. Still, often the experiments require ultra-high vacuum (UHV) conditions, since the measurements have to be performed at low temperatures, where water and other residual gases would otherwise adsorb to the surface.

Another challenge of the technique is the rather long wavelength (5-30 Å), making the detectable part of k -space very small. For this reason, not every system might be suitable for being investigated with this technique. The number of diffraction peaks, reachable for a certain sample, is limited as well. However, due to the spectroscopic power of the technique, a single diffraction peak can deliver lots of information about the electronic system.

Most experiments of this thesis were performed at the UE52-SGM1 and U49/2-PGM1 beamlines at BESSY. One experiment, as well as various tests, were performed at X1B of NSLS Brookhaven. All these beamlines are undulator soft x-ray beamlines with linearly polarized light or variable light polarization. The scattering geometry was always horizontal. The instruments operated were: the 2-circle UHV soft x-ray diffractometer at BESSY, built by Eugen Weschke and coworkers, and the 5-circle Spinoza diffractometer at NSLS, built by Peter Abamonte and coworkers. Since most of the data presented here were measured at BESSY, the setup there will be described in greater detail in the following.

Table 2.1: Beamline parameters at BESSY-diffractometer.

<u>Beamline</u>	Energy	Resolving power	Linear polariz.	Horizontal divergence	Vertical divergence
UE52-SGM1	400-1800 eV	10^4	π, σ	6 mrad	1 mrad
U49/2-PGM1	400-1800 eV	10^4	π	2 mrad	2 mrad

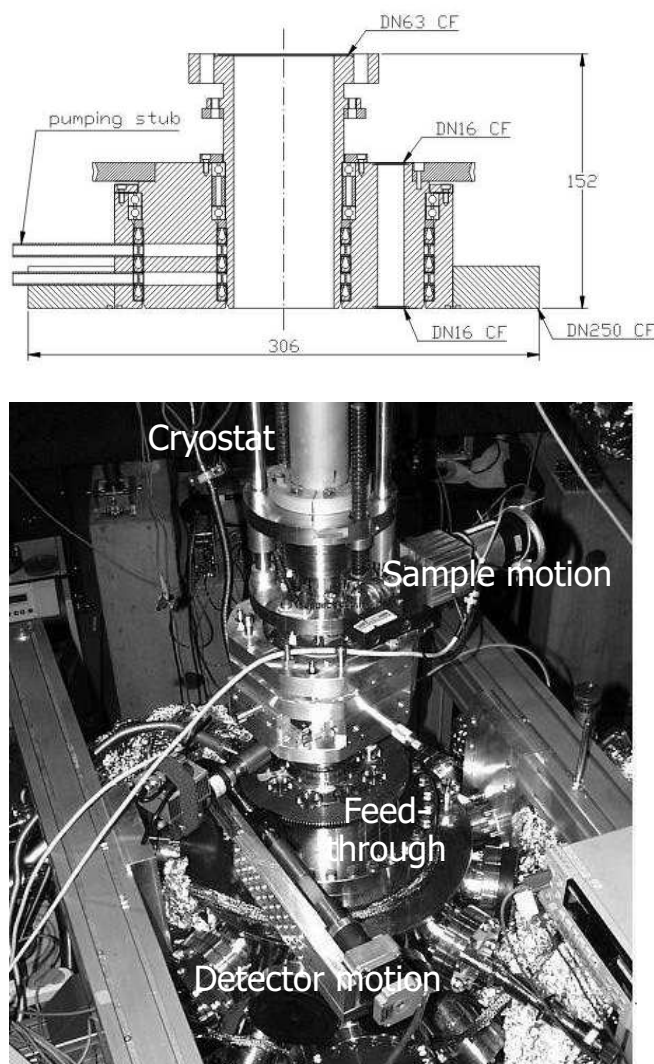


Figure 2.1: The BESSY-diffractometer. Upper: design of the rotary feed-through, bottom: view on the diffractometer showing the lower part of the cryostat on the x,y,z-translation stage and the rotary feed-throughs with motors.

2.1 Instrumental

The parameters of the beamlines in BESSY are listed in Table 2.1. The used diffractometer, designed by E. Weschke and coworkers from the Freie Universität Berlin [63], is an UHV two-circle diffractometer. The design is such that all motors are placed outside vacuum, guaranteeing good vacuum conditions with a base pressure of $< 10^{-10}$ mbar, even when the motors are operating. The sample and detector motion of this machine is accomplished by a double concentric differentially pumped rotary feed-through (see Fig. 2.1). The diffractometer design allows to easily install different kind of detectors. The typical diffraction geometry of a two-circle diffractometer is described in Chapter 1.1.1.

For the experiments presented here the used detector was an IRD-AXUV 100 Si-photodiode coated with 1000 Å Al to suppress the sensitivity to visible light. The

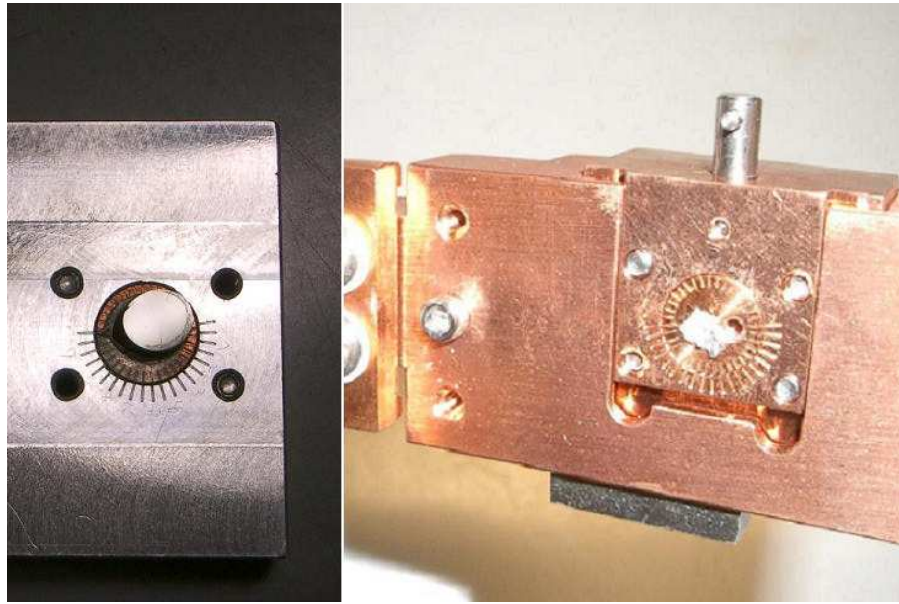


Figure 2.2: Azimuthal orientation. Left: a polished single crystal sample on the copper disc, placed on the Laue-camera holder, right: the wedge-shaped sample holder, mounted to the diffractometer sample stage.

diode was mounted on a 120 mm long arm, behind a slit carousel, which allows for variation of the slit width - the 8 slits being between $50 \mu\text{m}$ and 2 mm wide (in the scattering plane). We used a 2-mm detector slit, which corresponded to an angular acceptance of $\pm 0.5^\circ$ in-plane, which still provides an excellent k-resolution at the large detector angles. The out-of plane acceptance was defined by the diode height of 10 mm to $\pm 2.5^\circ$. The detector signal was measured with a Keithley 6514 electrometer and integrated over time with a voltage-to-frequency converter connected to the analog output of the electrometer and with a digital counter. The typical size of the detector signal was 20-50 pA, over a dark current of 4 pA. The signal was normalized to the photon flux as measured by the drain current of the last refocusing mirror of the beamline. The variation of the photoemission cross-section of the mirror with photon energy was determined using the detector diode in the direct beam and was corrected for as well as for the difference in the mirror signal for different light polarizations.

To allow for the sample exchange and azimuthal rotation of the samples in situ, we designed and built a transfer system. The system consisted of a load lock chamber with a sample garage, a transfer-arm, a wedge-shaped sample holder and a corresponding stage mounted to the diffractometer cryostat (Fig. 2.2, right). The samples could be transferred between the garage and the sample holder stage, using the transfer-arm. The wedge fitting of the sample holder into the stage ensured a good fit and a good thermal contact between the two components. Due to the open-axis design of the system, the sample holder stage could be directly mounted to the cryostat. The thermal and electrical contact between the probe and the cryostat was therefore very good, which allowed for a reliable temperature measurement, indispensable for low-temperature experiments, especially for investigation of prop-

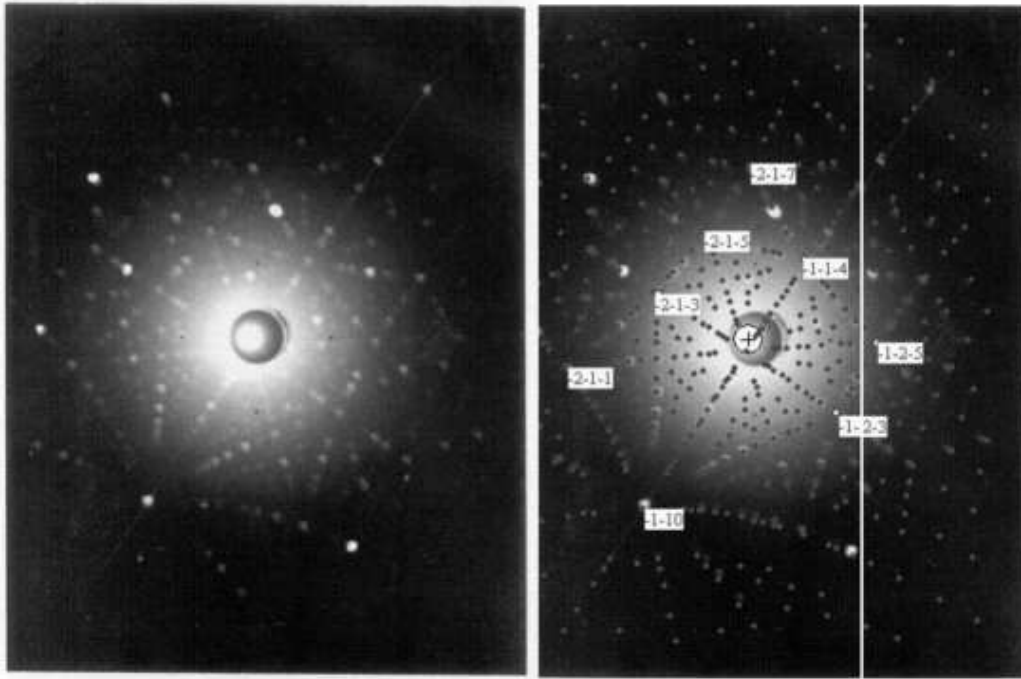


Figure 2.3: Laue picture of the investigated $\text{La}_{1.8}\text{Sr}_{0.2}\text{NiO}_4$ sample (left). The reflections were identified using the Orient Express orientation program (right).

erties near phase-transitions. The cooling of the system was accomplished by means of a APD dispex-type He closed-cycle refrigerator. The temperatures reached at the sample were lower than 40 K. As the thermometer a Si-diode thermo-sensor was used, in combination with a four probe Lakeshore controller. Stabilization of the sample temperature was achieved with the aid of a tantalum-wire heater, mounted in the vicinity of the sample, directly on the stage. A drain current measurement was used for total electron-yield absorption measurements (XAS).

2.2 Sample alignment

Bulk samples, such as $\text{La}_{1.8}\text{Sr}_{0.2}\text{NiO}_4$, were polished with the Logitech PM2 machine, in a two-step process. In the first step the sample was lapped on a cast iron disc, using a watery Al_2O_3 solution with $3 \mu\text{m}$ grain size, which removed the coarse roughness of the surface, as e.g. traces from the saw-blade. In the second step the sample was polished on a polyurethane disc, applying a $0.5 \mu\text{m}$ -granulated alkaline colloidal silica suspension. The sample reflectivity achieved in this way was very high, minimizing signal losses due to absorption at the surface. The surface of the sample was mirror-like, similar to the sample visible in Fig. 2.2, left. Due to the limited sample orientation possibilities in situ in the BESSY diffractometer, the sample had to be oriented and cut with a high accuracy, and after surface preparation mounted in a controlled way on the sample holder. The direction of the investigated crystal reflections had to lie within an accuracy of 1 in the scattering plane, to be detected. In order to diminish reflectivity background in the signal, the sample was

mounted with a slightly misaligned surface normal. The orientation of the sample was determined using a Laue-camera (see Fig. 2.3)

Since due to the limited orientation possibilities in situ, the correct azimuthal orientation of the probes has to be determined beforehand. A system was developed, to allow for an accurate transfer of a defined orientation from the Laue camera to the diffractometer sample holder. The samples were mounted to flat copper discs (~ 9 mm \varnothing) with an angular scale and screw thread on the back, allowing for rotation inside and outside vacuum. These discs fit tightly into a hole, milled into the holder of the Laue camera (Fig. 2.2, left) and also to the wedge-shaped holder for the diffractometer (Fig. 2.2, right). Both holders are equipped with a Vernier scale, allowing for an accurate adjustment/reading of the orientation of the disc. The samples were mounted directly to the copper discs with a silver glue, guaranteeing a good electric and thermal contact, and then mounted on the disc to the holder of the Laue camera or the diffractometer. The in this way achievable accuracy of the azimuthal orientation was as good as 0.5.

Chapter 3

Diffraction from a stepped surface of SrTiO₃

The existence of charge and/or orbital order has been a question of debate for many systems. The observation of a corresponding superstructure reflection cannot be considered as a prove for such an order, since it does not exclude other superstructure-forming mechanisms, as, e.g. Jahn-Teller-like lattice modulations. A sound investigation of the electronic properties of the system is necessary to solve such questions. Spectroscopical analysis of the superstructure signal, as provided by resonant soft x-ray diffraction, is an appropriate tool for this kind of studies, and can provide criteria how to differentiate between different mechanisms.

The fundamental difference between the superstructure formed by an electronic order and by pure lattice modulations is that the first implies a periodical arrangement of two or more electronically inequivalent atomic sites, whereas the second consists of only one kind of scatterers. From the scattering point of view we can therefore refer to the two cases as inhomogeneous and homogeneous. This difference must be clearly visible in the corresponding diffraction properties of the system, in particular in the spectral behavior of the signal. The total diffraction amplitude of the inhomogeneous structure is a coherent combination of different single diffraction amplitudes, which is not a simple summation. The diffraction signal is therefore expected to deviate from the macroscopic optical properties of the system, which are determined by the incoherent sum over all ions in the system. On the contrary, the diffraction signal of a homogeneous system should resemble the optical properties.

This chapter describes resonant diffraction studies of an homogeneous model system. We used single crystalline SrTiO₃ with an artificial superstructure, formed by terraces on the surface with a width of about 20 and 70 nm. Such a 2-dimensional structure has the properties of a reflection grating. The reciprocal lattice consists of equally spaced rods, rather than of points, simplifying considerably the fulfillment of the diffraction condition. We chose the SrTiO₃ compound, since it is characterized by a particularly simple electronic structure and by isotropic optical properties at Ti resonance edges.

Such a system is also well-suited to test the feasibility / sensitivity of the technique. The large width of the terraces corresponds to a small step density; $\frac{1}{50}$ and $\frac{1}{180}$ of the total number of unit cells in one monolayer SrTiO₃. Since the diffraction

signal in the system comes only from the surface layer, these numbers have to be reduced by another factor of roughly 100, due to the photon penetration depth of a few hundred Å.

The diffraction signal from the terraced SrTiO₃ was investigated spectroscopically across the Ti $L_{2,3}$ resonance and compared with the optical properties of the system. Further the optical constants of the compound were extracted from reflectivity data on a flat sample. These were used to model the diffraction signal from the terraces, applying an extended kinematic model.

3.1 SrTiO₃

SrTiO₃ is an appropriate system for model studies, since it has a particularly simple electronic structure. The formal valence of the components in this compound is (Sr²⁺), (Ti⁴⁺) and (O²⁻), meaning that the electron shells of all atoms are either fully occupied or empty in the ground state. It is a typical insulator and possesses no permanent magnetic moments. The crystal structure at room temperature is cubic perovskite (space group Pm3m), with a lattice constant of 3.905 Å. The Ti-ions are therefore embedded in an octahedral crystal field, generated by the neighboring oxygen ions. Due to this symmetry, the optical properties of the Ti-ions are isotropic, which means independent on the polarization direction of the scattered light.

At energies around the Ti $L_{2,3}$ edge (~ 460 eV) the optical properties of the compound are totally dominated by the Ti $2p \rightarrow 3d$ transition. The Ti⁴⁺ ions are excited from the $2p^63d^0$ to a $2p^53d^1$ multiplet state, under the formation of an exciton. Therefore this process can be well described in terms of a local picture, assuming that the electron is localized at the TiO₆ cluster. The absorption spectra of d^0 systems in O_h symmetry at transition metal $L_{2,3}$ edges have been extensively studied and modelled by de Groot et al. [64], applying cluster model calculations.

The spectra can be fully described by the $2p^53d^1$ multiplet, which consists of seven dipole-allowed visible lines. The four most intense are split into two groups, due to the spin-orbit coupling of the core hole, such that the two at lower energies belong to the L_3 edge, whereas the other two to the L_2 edge. The splitting within each group is mainly determined by the crystal field-splitting of the O_h symmetry, $10Dq$. Two of the weaker lines are on the low energy side of the spectrum, the third in between the two L_3 main lines. They are due to the Coulomb and exchange interactions within the multiplet.

3.2 Experimental

The samples were prepared in the group of D. H. A. Blank at the University of Twente, The Netherlands. In order to obtain a well defined TiO₂-terminated surface, the SrTiO₃ single crystals were etched in buffered HF and subsequently annealed in oxygen [65]. The samples had the form of square plates with an edge length of 10 mm and a thickness of 0.5 or 1 mm. The surface orientation was essentially (001). For the diffraction experiments we used samples with miscut angles of 0.31 and 1.09 degrees from this direction, which corresponds to a terrace width of 70

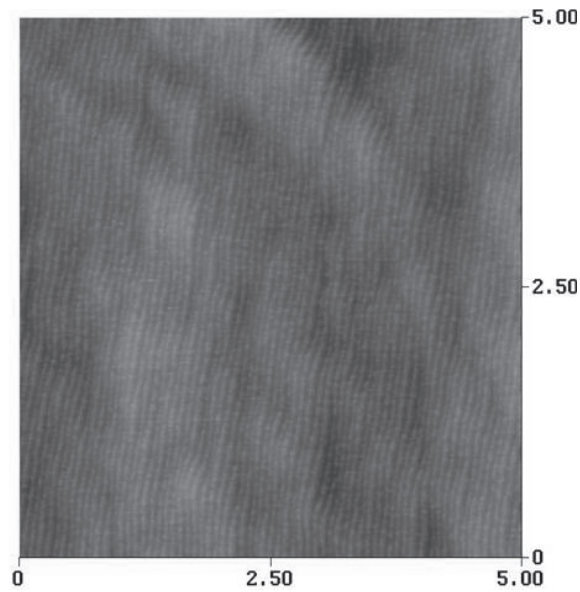


Figure 3.1: Atomic force spectroscopy (AFM), stepped SrTiO₃ [M. Huijben, University of Twente].

and 20 nm, respectively. All samples were characterized by atomic-force microscopy (AFM) and x-ray absorption (XAS). For determination of the optical parameters a flat (non-miscut) sample was used, which was prepared similarly.

Fig. 3.1 shows an AFM picture of one of the samples. The steps are equally spaced, though slightly wavy, leading to a regular stripe-like surface structure. The edges of the terraces are almost parallel to the sample edge, which has the direction [100].

Before mounting in the diffractometer, the flat sample was cleaned in acetone for 15 min and for a few minutes in methanol, using an ultrasonic bath. The stepped samples were mounted such, that the edge of the steps was oriented perpendicular to the scattering plane and the incident beam was pointing toward the steps (see Fig. 3.2). Before each measurement, the samples were annealed to 300 C inside UHV in an oxygen atmosphere of $5 \cdot 10^{-3}$ mbar for 30 min, to desorb gas particles adhering to the surface.

The experiments were performed at the X1B soft x-ray beamline of NSLS and the UE52-SGM1 beamline at BESSY. In both cases the scattering geometry was horizontal and the light linearly polarized in π -direction.

3.3 Diffraction data

A regular arrangement of steps on the surface of a sample will have the properties of a reflection grating. When the height of these steps is equal to the lattice parameter a and ξ is the miscut / inclination angle, the average width of the terraces will be equal $\frac{a}{\tan \xi}$. In analogy to a grating, a diffraction signal can be measured when the

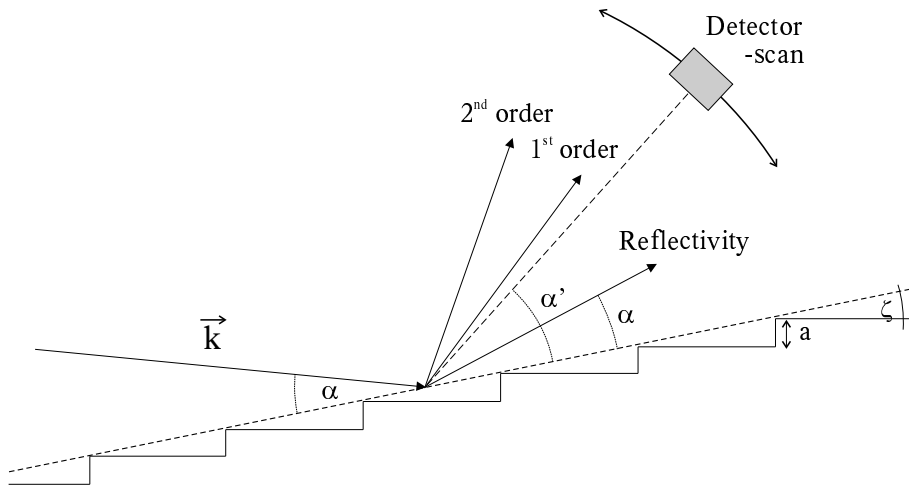


Figure 3.2: Schematic setup for diffraction from a stepped surface.

following condition:

$$\frac{a}{\tan \xi} (\cos \alpha - \cos \alpha') = n\lambda, \quad n \in \mathbb{N} \quad (3.1)$$

is fulfilled. The angles of incidence and diffraction, α and α' , are expressed here with respect to the averaged surface normal (Fig. 3.2), λ is the x-ray wavelength.

For a chosen angle of incidence several reflections can be measured, as illustrated in Fig. 3.2, one belonging to the specular reflectivity ($\alpha' = \alpha$) and others to diffraction from the terraces. These reflections can be probed, e.g. by scanning the detector angle.

The advantage of a 2-dimensional superstructure is that, like in a LEED experiment, the Laue conditions are relaxed and that it is hence much easier to find a diffraction signal. The reciprocal lattice consists of 1-dimensional rods, rather than of a 3-dimensional array of points. If the wavelength is short enough (shorter than two times the superstructure lattice parameter), a diffraction peak can be observed for any chosen angle of incidence.

Fig. 3.3 shows a scan measured from 1.09 degrees-inclined sample by changing the detector angle. The angle of incidence here was kept at 5 degrees and the photon energy was 900 eV, lying far above the Ti resonance. The symbols in the diagram represent data points whereas the solid line is a simulation according to a kinematical model. The data shows a pronounced maximum around 21.7, which is the position for the first order reflection. The observation of this signal clearly demonstrates the feasibility of the soft x-ray diffraction technique. Outside Ti resonance the contrast coming from the steps is as small as $\frac{1}{20.000}$, due to the rather long photon penetration depth, which proves that diffraction using soft x-ray energies is sensitive enough to study even very “dilute” systems.

The higher order peaks cannot be resolved from the background signal. Apparently their intensity is lower than expected for an ideal system, due to roughness of the sample [66]. The width of the measured diffraction peak shows us that the widths of the terraces on the surface vary from the average value. In the simulation a Gaussian distribution of widths around $\frac{a}{\tan \xi}$ was considered. The increase of

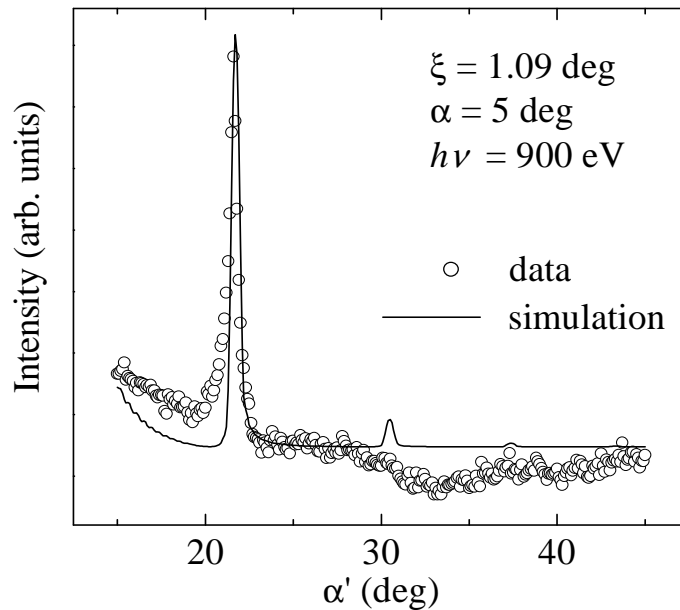


Figure 3.3: Detector-angle scan across the diffraction peaks from a stepped, 1.09 deg-inclined SrTiO₃ sample, measured off resonance.

background toward low detector angles is due to the tail of the reflectivity.

When the photon energy is tuned to the Ti L_{2-} or L_{3-} edge, the diffraction signal is considerably increases; by about an order of magnitude. The intensity of the diffraction signal varies strongly across the resonance edge, as energy is changed. Fig. 3.4 shows an energy scan of the diffraction signal, compared with the x-ray absorption (XAS) and reflectivity spectrum for the same energy range. All spectra were taken from the 0.31 deg-inclined sample at 30 deg incidence angle. The diffraction and reflectivity spectra look almost identical. They show the four main features, which are also present in the absorption spectrum, although in the latter slightly shifted toward higher energies (between 0.1 - 0.2 eV). The relative intensities of the main peaks in the absorption spectrum are different and the weak lines are more pronounced here than in the diffraction and reflectivity data. In fact it is not expected for the absorption spectrum to look exactly alike the diffraction or reflectivity signal since it is determined only by the imaginary part of the scattering amplitude, whereas the other two are described by the squared modulus of the sum of the real and imaginary part. The square involved here enhances the stronger lines more than weaker features, which is why the weak lines are barely visible in the reflectivity and diffraction data. Apart from that the similarities between the measured optical spectra and the diffraction signal are large.

The results show that the energy dependence of the diffraction signal of SrTiO₃ at the Ti $L_{2,3}$ edge does not differ much from that of the absorption spectrum. This appears to be the fingerprint of an electronically homogeneous system.

If we look carefully at the diffraction and reflectivity spectra and their dependence on the angle of incidence, there is some systematics that can be recognized. The spectra in Fig. 3.5 show diffraction and reflectivity data from samples with

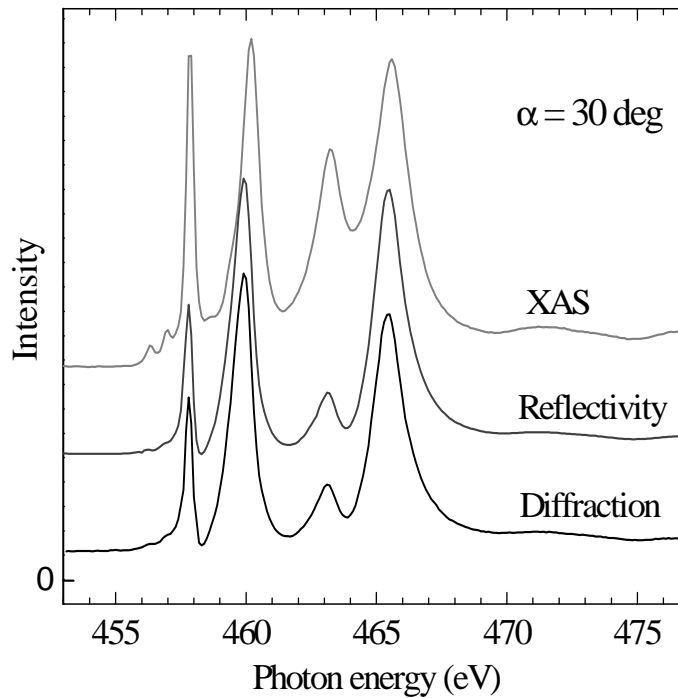


Figure 3.4: Spectroscopy of the x-ray absorption (XAS), reflectivity and diffraction signal across Ti $L_{2,3}$ edge: 0.31 deg-inclined SrTiO₃.

0.31 deg and 1.09 deg surface miscut, respectively. The diffraction and reflectivity data for both samples look very similar. With decreasing angle of incidence we observe a slight shift in the position of the maxima toward higher energies. Also the relative intensities of the peaks at higher energies increase for flatter angles. These changes are stronger pronounced in the reflectivity data than in the diffraction signal, especially at the lowest angle of incidence (5 deg). Here additionally the intensity of reflectivity behind the resonance edge is much larger than for energies below the resonance onset; such a jump is much less pronounced for larger incidence angles.

The diffraction signal of the steeper sample (1.09 deg) changes slightly less than the diffraction signal of the flatter (0.31 deg) sample. It almost doesn't shift between 30 deg and 5 deg of incidence angle, whereas the diffraction peaks of the 0.31 deg sample shift on average by 0.3 eV. Its reflectivity, however, looks exactly alike the reflectivity of the flatter sample. For comparison the reflectivity signal of the 0.31 probe at 5 deg of incidence has been plotted in the right diagram of Fig. 3.5 (dotted line).

3.4 Optical constants

For a quantitative description of the data the optical properties of the sample have to be known. While off resonance the index of refraction is tabulated [67], these tables are not accurate enough near resonance.

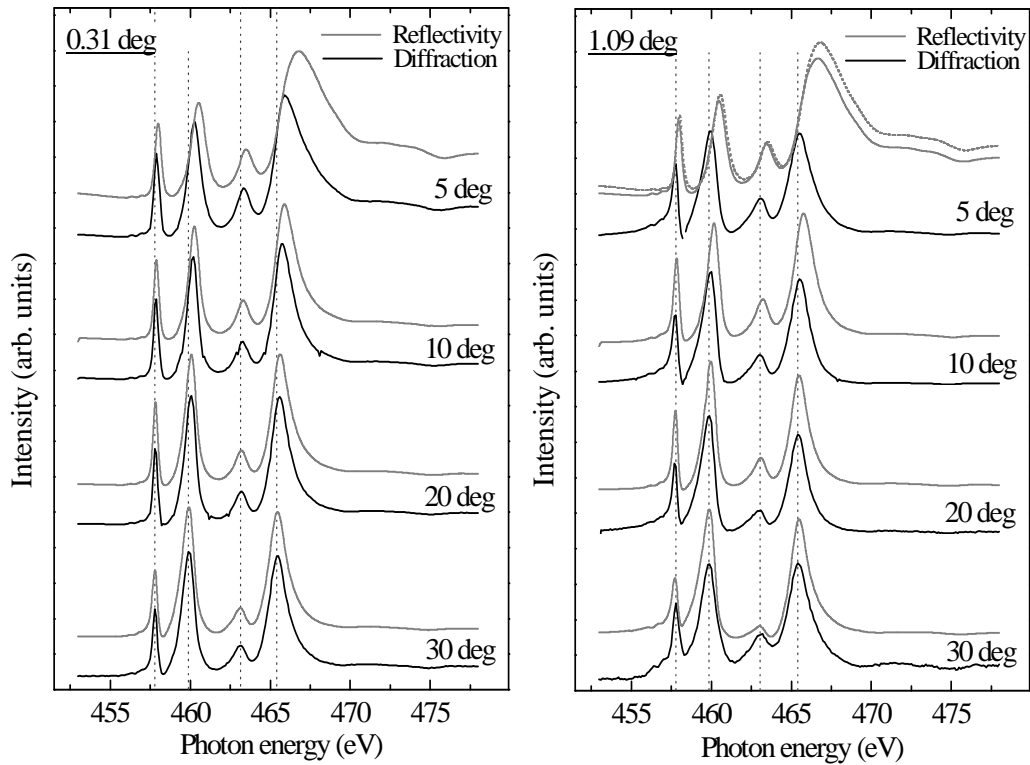


Figure 3.5: Reflectivity and diffraction data from 0.31 deg (left) and 1.09 deg (right) inclined samples for different incidence angles ($\alpha = 5, 10, 20, 30$). The dotted curve for $\alpha = 5$ at the right side (plotted for comparison) is reflectivity of the 0.31 deg sample.

As already mentioned in Chapter 1.3.2, the intensity of the reflectivity signal is described by Fresnel equations, which are functions of the angle of incidence and the refraction index. Therefore, knowing the dependence of the signal on the angle of incidence α , the index of refraction n can be obtained experimentally and consequently, according to $n = 1 - \delta + i\beta$, also the optical constants δ and β .

To that end we performed angle-dependent reflectivity measurements for a sample with a flat surface, using π -polarized light. The energy range for the entire Ti $L_{2,3}$ resonance (450-490 eV) was covered with steps of 1 eV. Fig. 3.6 shows reflectivity data for selected energies (symbols), together with the result of a least square fit (lines). The intensity of the signal decreases approximately exponentially with larger (steeper) angles of incidence. At low angles total external reflection occurs leading to the maximum around 2 degrees. The decrease of signal for very small incidence angles seen in the data is due to the fact that for flat angles the projection of the x-ray beam on the sample surface becomes larger than the surface area, leading to a loss of intensity. In this region the intensity of the light falling on the sample is proportional to $\frac{x \sin \alpha}{b}$, where x is the sample width and b the beam-width in the scattering plane.

The data were analyzed using the Fresnel equation for π -polarized light (1.24) and a Dabye-Waller like damping to account for the sample roughness of 3 Å. For most large negative values of δ (indicated in the diagram by the gray points) the shape of

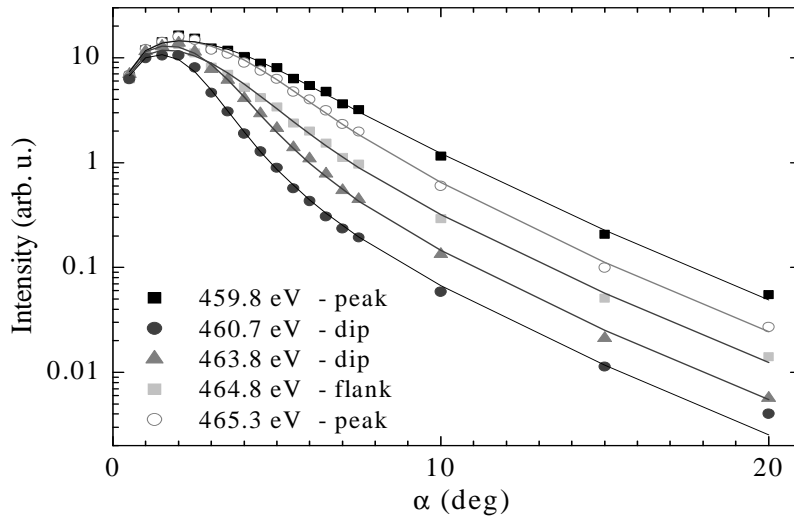


Figure 3.6: Reflectivity data (symbols) upon the angle of incidence α ; the solid lines are fits (applying Fresnel equations). Logarithmic display.

the reflectivity curve is essentially the same for a wide range of (δ, β) sets [68]. The fit does not converge in this region and the congruence of the resulting fitting curves with the data points is here not as good, as for the other (most) energies (for which Fig. 3.6 is representative). The XAS data, however, provide a second independent information about β . Therefore both constants can be fitted in the critical region as well, although with a much larger uncertainty.

The obtained optical constants δ and β are shown in Fig. 3.7, together with the absorption spectrum (XAS) at 30 deg incidence angle (upper curve). The error bars denote the maximum uncertainty for the critical region. Outside the marked points the uncertainty for δ amounts to 10 percent, whereas for β it is a little bit smaller. Behind the resonance edge, at 490 eV, δ is approximately equal to $2.5 \cdot 10^{-3}$ and β to $1.6 \cdot 10^{-3}$, which agrees very well with the tabulated x-ray data [67], giving for this energy $2.3 \cdot 10^{-3}$ and $1.5 \cdot 10^{-3}$, respectively (assuming a mass density of 5 g/cm^3 for the sample). Across the resonance the optical constants are strongly energy-dependent. Whereas β resembles the absorption spectrum, reaching peak values at each resonance - with the maximum of $12 \cdot 10^{-3}$ at 460.25 eV, δ behaves similar to the negative derivative of β . δ changes sign each time a strong absorption peak is crossed; coming from the low-energy side it decreases steadily reaching a negative-signed minimum just before the absorption peak; directly above the absorption maximum it jumps suddenly toward a positive-signed maximum, crossing the zero line exactly at the resonance, and decreases again more slowly afterwards, crossing the zero line in the vicinity of a local β minimum. The largest value that δ reaches is negative-signed; $-8 \cdot 10^{-3}$ at 460.1 eV.

The extreme variation of δ toward negative values before each resonance strongly dominates the optical properties of the material, changing its optical density. It is remarkable that the substance partially becomes optically more dense than vacuum (each time δ is negative), whereas for the conventional x-ray range (photon energies $\geq 10 \text{ keV}$) it is known that matter is always optically less dense than vacuum. This

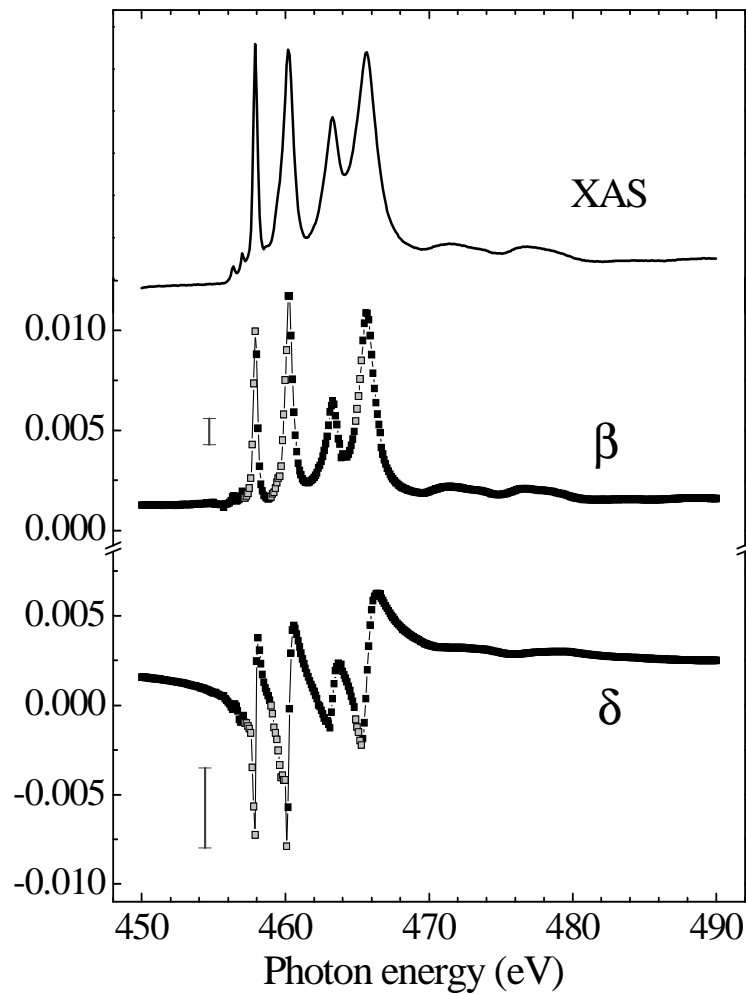


Figure 3.7: Optical constants δ and β together with the absorption spectrum (XAS) at 30 deg of incidence. The error bars indicate uncertainty for the gray marked points.

fact demonstrates that the oscillator or atomic scattering strength is extremely large in the vicinity of the soft x-ray absorption edges.

Fig. 3.8 shows the penetration depth of photons Λ and the critical angle α_c across the Ti $L_{2,3}$ resonance in SrTiO_3 . Both quantities can be directly obtained from the optical constants; Λ is the inverse of $2k\beta$ and for the later applies: $\cos \alpha_c = \sqrt{1 - \delta}$. Outside resonance Λ has values well above 100 nm, meaning that the signal is clearly bulk sensitive. At the resonance maxima the photon penetration depth can drop to 20 nm, which is still an order of magnitude higher than the penetration depth in surface sensitive techniques, as that of electrons in photoelectron spectroscopy. Nevertheless, the ability to pick up the diffraction peak from the stepped surface demonstrates that the technique *can be* surface sensitive, if the bulk material does not show (the same) superstructure. We can therefore exclude that soft x-ray scattering techniques should be representative for surface properties.

The critical angle varies across the resonance, resembling the behavior of δ . Outside resonance the magnitude of α_c lies between 2 and 3 degrees. Above each resonance maximum it reaches peak values, the highest being 4.5 deg for 478 eV

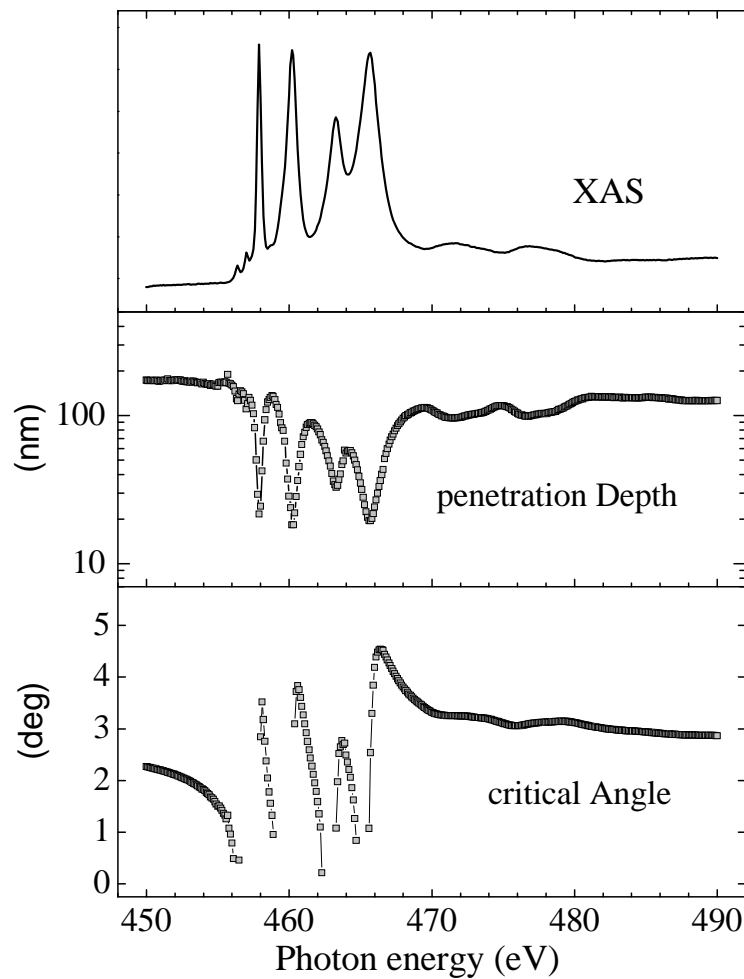


Figure 3.8: Penetration depth of photons Λ (logarithmic scale) and the critical angle α_c , both obtained from the optical constants in Fig: 3.7.

photon energy; positioned at the high energy side of the spectrum. For energies below resonance maxima, where δ becomes negative, it is not defined and the effect of total reflection disappears completely.

The rather high values of α_c suggest that optical spectra measured at low incidence angles should be strongly influenced by the appearance of total reflection. Fig. 3.9 shows specular reflectivity data for α between 7.5 and 2 degrees. The top diagram displays α_c for comparison. The reflectivity data is plotted without re-scaling of the relative intensities. The curve measured at $\alpha = 7.5$ deg resembles very much specular reflectivity for high incidence angles, but as the angle of incidence becomes flatter, the shape of the spectra changes considerably. Approaching the critical angle, the positions of the main peaks shift toward higher energies and the relative intensities of the spectrum features change; the intensity outside resonance increases strongly in comparison to the main peaks and smaller features of the spectra become more visible. Comparison with the values of the critical angle α_c at energies where these changes are particularly strong suggests that these effects are caused by the occurrence of total reflection. As the incidence angle approaches

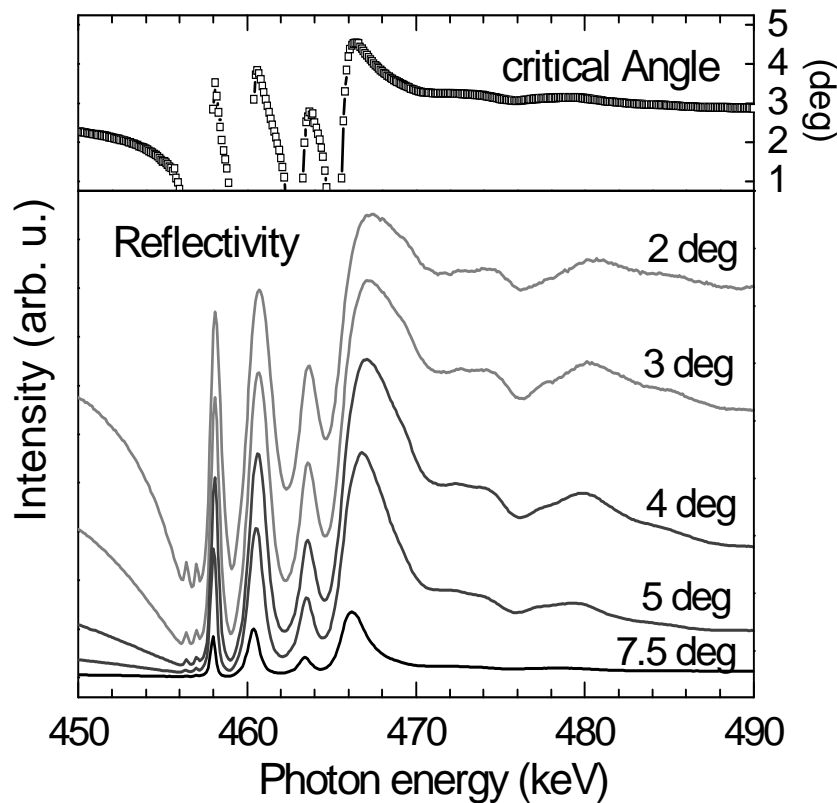


Figure 3.9: Reflectivity for low incidence angles for the flat SrTiO₃ sample. The upper diagram shows the critical angle obtained from δ .

α_c , the intensity of specular reflectivity is strongly increased, e.g. at the position of the highest energy peak (466 eV) for $\alpha = 4.5$ deg and at the background below the resonance edge for $\alpha = 2$ deg. When the incidence angle becomes smaller than the critical angle, the increase in intensity is reduced, probably due to saturation (maybe one part of the intensity is also reflected in a non-specular direction). This would explain the decrease of the relative intensity of the main peaks below 5 degrees of incidence. (Above the critical angle Fresnel equations predict an exponential increase of intensity for π -polarized light toward low angles.)

The influence of α_c on the absorption spectra (XAS) is even larger, since the spectra are partially distorted. In the absorption spectra first the intensity in the main peaks is reduced and further these peaks seem to disappear and shift, or reappear at different positions. This effect has been already observed in the past (as well as the changes in the reflectivity data), and interpreted in terms of appearance of new multiplet terms [69]. Our data (Fig. 3.10) clearly shows that the changes in the absorption spectra at low incidence angles are caused by the occurrence of total reflection, leading to a loss of intensity for certain energy values. This fact is clearly visible in Fig. 3.10, in the data measured at 1.5 deg incidence. Here the absorption data behaves like the negative of the reflectivity data, the absorption spectrum showing minima exactly at the positions of maxima of the reflectivity signal. Well above the critical angle both spectra look very similar (see 30 deg of

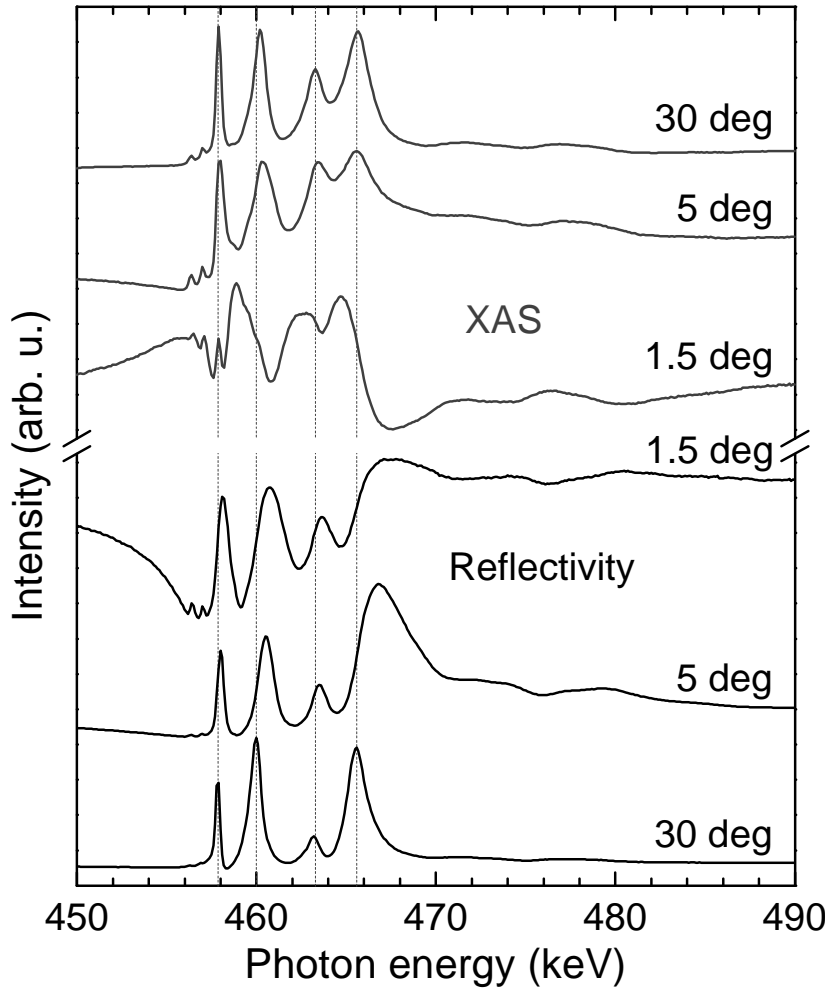


Figure 3.10: Comparison of XAS (upper 3 curves) and reflectivity data for different angles of incidence ($\alpha = 30, 5$ and 1.5).

incidence). These results show that the effect of total reflection indeed dominates both, reflectivity and absorption spectra, for low incidence angles.

3.5 Modelling of the spectra

We modelled the stepped system through a 2-dimensional array of points, each point representing one crystal unit cell of SrTiO₃. This model accounts only for unit cells lying in the diffraction plane. The extension of the x-ray beam perpendicular to the diffraction plane is neglected, which in fact should not have any influence on the results. The position of each unit cell in the array is described by means of the Cartesian coordinate system (x, z) , the x -axis pointing along the surface of the terraces and the z -axis towards the crystal, see Fig. 3.12. The distance between two cells along these directions corresponds to $a = 3.905 \text{ \AA}$, the lattice constant of the cubic SrTiO₃ structure.

The scattering amplitude of each array point is the same, since it corresponds

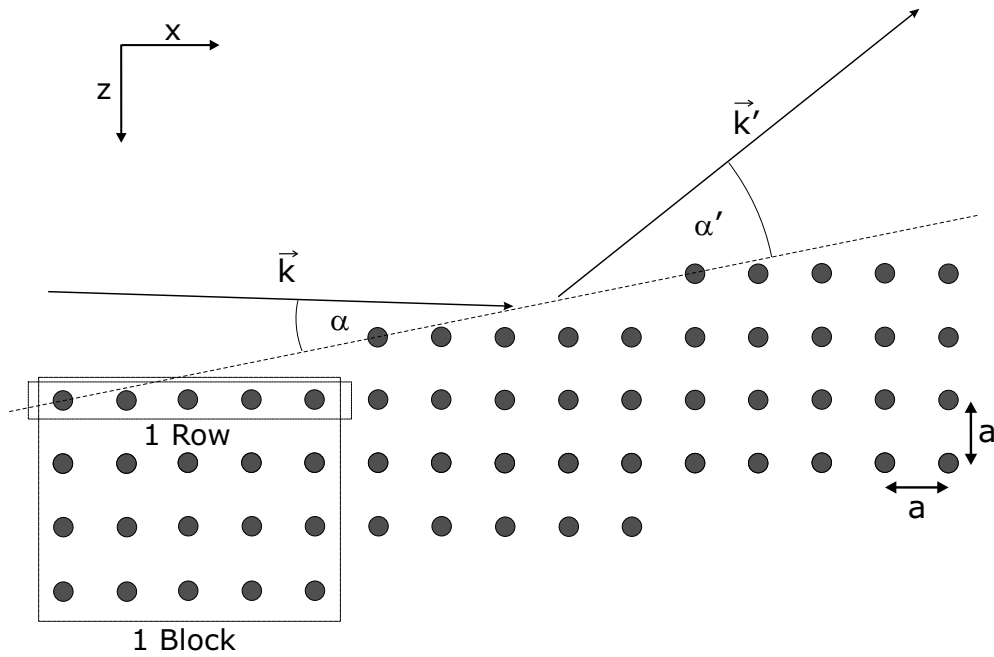


Figure 3.11: Model of the stepped surface used in the simulation.

to the form factor of the crystal unit cell of SrTiO_3 ; $F_S(\vec{q}, \omega)$, the stepped system can be hence denoted as homogeneous (from the scattering point of view). Because the optical properties of SrTiO_3 at the Ti $L_{2,3}$ edge should be isotropic, $F_S(\vec{q}, \omega)$ is independent on the orientation of the sample and can be therefore described through a complex quantity. In the following the q -dependence of F_S will be neglected, based on the assumption that the shape of the diffraction spectrum at the Ti resonance is totally dominated by the energy-dependent terms. $F_S(\omega)_{q=0}$ is calculated applying (1.12), using the obtained optical constants δ and β from the previous section.

Applying the kinematical approximation, the diffraction amplitude of the 2-dim array is equal:

$$A(\vec{q}_v, n(\omega)) = \underbrace{F_S \cdot \sum_{j=1}^W e^{i\vec{q}_m j a \vec{e}_x}}_{\text{1 Row}} \underbrace{\sum_{l=1}^Z e^{i\vec{q}_m l a \vec{e}_z}}_{\text{1 Block} \equiv \text{1 unit cell}} \sum_{m=1}^N e^{i\vec{q}_v m a (W \vec{e}_x + \vec{e}_z)}. \quad (3.2)$$

The vectors $\vec{q}_v = (q_{vx}, q_{vz})$ and $\vec{q}_m(\vec{q}_v, n(\omega)) = (q_{mx}, q_{mz})$ represent the scattering vectors in vacuum and in matter. The coordinate system has been chosen such, that q_x and q_z correspond to q_{\parallel} and q_{\perp} , the components parallel and perpendicular to the surface normal of the steps; see Fig. 3.12. The first sum in (2.2) calculates the scattering amplitude of one row of SrTiO_3 crystal unit cells; represented by a linear chain of equidistant points, spaced by a . The chain has exactly the length of one surface terrace: $W a = \frac{a}{\tan \xi}$ (ξ being the surface-inclination angle). Multiplication of this term with the second expression yields the amplitude of a 2-dimensional terrace block, consisting of Z rows. This block forms the unit cell of the stepped-surface

system, the displacement between the single blocks being $\vec{d} = (Wa, a)$. The last summation in the equation calculates the scattering amplitudes of N blocks. This step leads to the fulfillment of the diffraction condition, producing a non-vanishing diffraction intensity at the corresponding angle. This diffraction peak is a pure result of the periodic modulation of the scattering phases (with the vector \vec{d}).

The special feature of our model is that the scattering vector $\vec{q}_m \equiv \vec{k}'_m - \vec{k}_m$ in (1.2) is a complex quantity. This is the consequence of applying Snell's law to the complex refractive index n , in analogy to Chapter 1.3.1. The wave vectors of the incident and diffracted beam in matter, \vec{k}_m and \vec{k}'_m , were obtained directly from (1.19) and (1.20). Accordingly, only q_{zm} , the component perpendicular to the surface, has an imaginary contribution. This accounts in a correct way for the damping of the photon electric field inside matter, since the scattering intensity is the same for all points at the same depth in the sample. Also the variation of the scattering volume across the resonance is automatically taken into account.

The model reproduces the correct positions for the specular reflectivity and for the diffraction signal, in terms of the detector angle, as was already shown in Fig. 3.3. Further, using the obtained optical constants from the previous section, it allows for the calculation of the energy dependence for both signals. Fig. 3.12 shows results of the simulation for the 0.31 deg-inclined sample (dotted line and symbols) together with the data (solid line), measured across the Ti $L_{2,3}$ edge. The left side displays the specular reflectivity data and the right side the first-order diffraction peak data. The incidence angles are from the top to bottom: 5, 10, 20 and 30 degrees. The simulation curves in both sets fit the data quite well, although not perfectly. The spectral shape and the relative intensities of the main peaks are well reproduced, including the transfer of intensity toward higher energy peaks for smaller incidence angles. The exact position and the width of the peaks in the simulation, however, deviates a little from the data. Whereas the agreement between the simulation and the data set for the 10 degrees angle is rather good (apart from deviation in intensity behind the resonance edge for the reflectivity spectrum), for higher angles the simulated spectra seem to be shifted in energy toward higher values, in respect to the measured ones. The width of the second main resonance in the model is here also smaller. Apparently, the model does not reproduce the energy shift, occurring in the diffraction and reflectivity data (evident from Fig. 3.5, left) when the incidence angle changes. In the 5 degrees spectra, the strong intensity increase behind the resonance edge, especially for the reflectivity signal, is not reproduced. Since this effect is due to approaching the critical angle value (see Fig. 3.8), where the Snell's law is known to break down, the model cannot describe this effect.

3.6 Results and discussion

The stepped surface of a single crystal can work as an artificial 2-dimensional superstructure, with a periodicity in the nm-range, which can be used to produce diffraction peaks with soft x-rays. The signal is well visible, even for a step density smaller than $\frac{1}{50}$, and can be further amplified if energies corresponding to a resonance edge of the system are used. This proves the feasibility of the technique,

demonstrating that resonant soft x-ray diffraction is extremely sensitive and suitable to study also very “dilute” systems.

We investigated the first-order diffraction signal from a stepped SrTiO₃ system, with a terrace width of 20 and 70 nm at the Ti $L_{2,3}$ resonance. The behavior of the diffraction signal with energy resembles the behavior of the optical data, showing the same spectral features and the same energy dependence. We are convinced that this attribute is a fingerprint for a system, where the superstructure is due to a pure phase modulation, rather than to a contrast in the scattering amplitudes. The electronic structure seen by the coherent diffraction signal is then namely the same, as the electronic structure seen by the incoherent absorption signal. This should be not the case, if the superstructure was formed by a long-range electronic order.

Measurement of the reflectivity signal can be used to obtain the optical constants δ and β across resonance in the soft x-ray range, as was already done for instance in the ultraviolet-soft-x-ray region [68]. The optical constants in the SrTiO₃ system reach values up 10^{-2} at the resonance maxima of the Ti $L_{2,3}$ edge, δ changing sign before and after each strong resonance, which dominates the optical properties of the system in this region. The photon penetration length varies between 20 and 200 nm, showing that the method is not very surface sensitive. Nevertheless, it can be sensitive to the surface if the bulk material has no or a different superstructure. The values of the critical angle are considerably large, lying between 2-3 degrees outside resonance and reaching up to 4.5 deg close to the maxima. Data obtained at low incidence and detection angles might be therefore influenced by the appearance of total external reflection. In the SrTiO₃ system both, reflectivity and absorption data become distorted when the incidence angle approaches 5 degrees. Below the critical angle the intensity of the absorption signal is strongly decreased.

The energy dependence of the specular reflectivity and the diffraction signal from the stepped system could be obtained fairly well by applying a kinematical model and taking into account the variation of the optical constants δ , β with energy. The deviations between the simulation and the data for higher angles of incidence could be due to the fact that the optical constants can be obtained only with a limited accuracy, especially at the low energy site of each resonance. Since only k -components, which are perpendicular to the surface plane of the sample change, depending on the values of δ and β , this could explain the better fit for data with a flatter incidence angle (but a still sufficiently larger than the critical angle). Other possibilities would be a changed electronic structure at the surface or maybe near-field effects, which could lead to the breakdown of Snell’s law for the outermost sample layers.

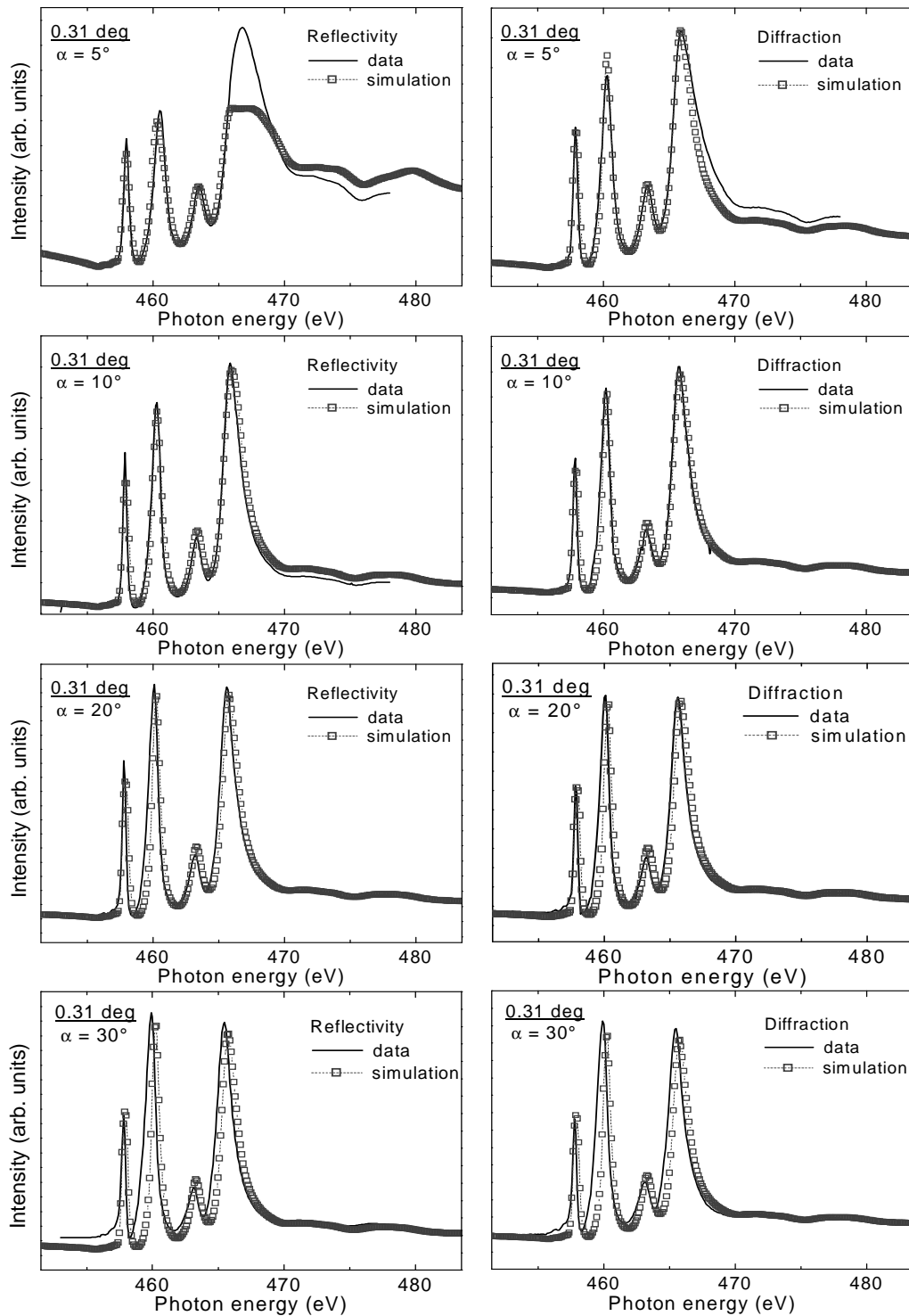


Figure 3.12: Results of the kinematical model simulation (dotted line and symbols) in comparison to the measured signal (solid line) for the 0.31 deg-inclined sample; left: specular reflectivity, right: first-order diffraction signal.

Chapter 4

Spectroscopy of stripe order in $\text{La}_{1.8}\text{Sr}_{0.2}\text{NiO}_4$

4.1 $\text{La}_{2-x}\text{Sr}_x\text{NiO}_4$ system

Sr-doped La_2NiO_4 has been intensely studied in the past, not only because of its relevance for the understanding of high-temperature cuprate superconductors [13, 39, 70–90]. Like the iso-structural La_2CuO_4 , La_2NiO_4 is an antiferromagnetic insulator (AFI). Upon doping either by replacing La with Sr or by adding oxygen $\text{La}_{2-x}\text{Sr}_x\text{NiO}_{4+\delta}$ stays in this AFI state up to high doping levels $n_h = x + 2\delta < 0.7$. This behavior is in strong contrast to the cuprate system, for which the antiferromagnetic order is quickly destroyed already for $x > 0.05$ and which for higher x values becomes metallic and superconducting at low temperatures. On the other hand the doped Cu and Ni systems show similar order phenomena: in both systems ordered periodic arrangements of doped holes were found. These so called stripes are 1-dimensional hole rich regions, which form antiphase domain walls for the antiferromagnetic background of the hole-poor sites [14]. In the stripe phase the doped holes are confined to the NiO_2 or CuO_2 layers, respectively and the hole spin couples antiferromagnetic to the transition-metal spin. While in the nickelates these stripes are static with a propagation direction diagonal with respect to the Ni-O-Ni bond directions in the NiO_2 planes, for $\text{La}_{2-x}\text{Sr}_x\text{CuO}_4$ essentially dynamic stripes are found with a propagation direction along the Cu-O bonds. The existence of static stripes in nickelates is the reason why they were observed in this system first by diffraction techniques, while the observation of stripes in cuprates was obtained afterwards in a compound where static order was stabilized by additional Nd-doping. Only very recently stripe order was observed directly in $\text{La}_{2-x}\text{Ba}_x\text{CuO}_4$ with $x = 1/8$ by resonant soft x-ray diffraction [30]. While the majority of experimental studies are in favour of the stripe model, competing models for the order pattern have been proposed as well [91, 92].

The relationship between charge ordering and superconductivity has been a central question in the studies on stripe phases in cuprate systems. It is generally believed that superconductivity can be destroyed by an electronic ordering phenomena (charge ordering), which competes with the interaction of Cooper-pairs [79].

Most of our knowledge about stripe phases in nickelates and cuprates is based on

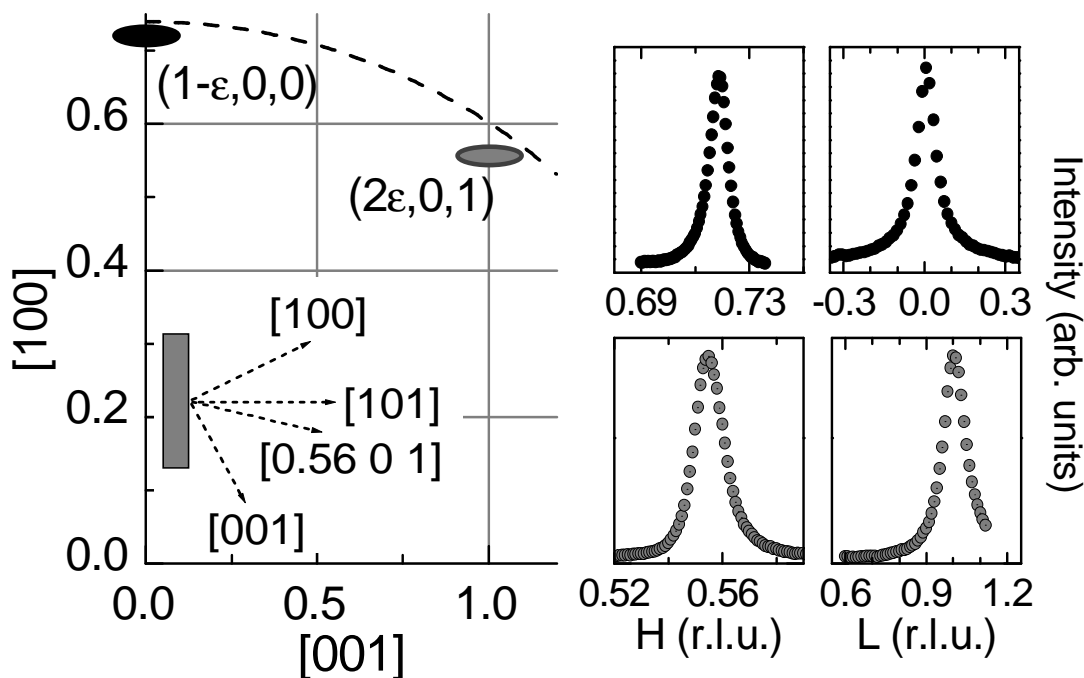


Figure 4.1: Position of the investigated superstructure peaks in k -space (left) and scans along the H- and L-direction (right) using π -polarized light. Black symbols: spin order $(1 - \epsilon, 0, 0)$ peak, gray symbol: charge order $(2\epsilon, 0, 1)$ peak. The inset shows the scattering geometry; the position of the accessible reflections in the scattering plane.

neutron, conventional x-rays diffraction and x-ray absorptions spectroscopy (XAS). These probes, however, are not directly sensitive to the electronic state of the scatterer and charge order is probed indirectly via the accompanying lattice distortions. K -edge resonant diffraction is advantageous in the sense that it provides contrast for different valence from the chemical shift of the resonance, but the spectroscopic information obtainable is rather limited since the electronic excitation involves the transition-metal $4p$ states, which are only weakly sensitive to the $3d$ electronic state of interest. The spectroscopically most powerful technique is resonant soft x-ray scattering at the transition-metal $L_{2,3}$ or oxygen K resonance, which involves virtual excitations into the metal $3d$ or oxygen $2p$ states and which is hence extremely sensitive to the electronic state of the scattering ions.

4.2 Experimental

We performed spectroscopy studies of diffraction peaks from stripe order in the $\text{La}_{1.8}\text{Sr}_{0.2}\text{NiO}_4$ system, across the Ni $L_{2,3}$ resonance. The $\text{La}_{1.8}\text{Sr}_{0.2}\text{NiO}_4$ single crystal was grown by Mohammed Benomar, applying the traveling solvent method in the institute in Cologne, with a four-mirror image furnace (FZ-T-10000-H-VI-VP, Crystal Systems Inc.) [93]. It was characterized by powder x-ray diffraction for phase purity and by neutron diffraction at the Orphée reactor diffractometer 3T.1. Its incommensurability parameter ϵ was found to be about 0.28.

At room temperature $\text{La}_{1.8}\text{Sr}_{0.2}\text{NiO}_4$ has a tetragonal $I4/mmm$ symmetry with the lattice constants $a = 3.807 \text{ \AA}$ and $c = 12.55 \text{ \AA}$ (referred to as the High Temperature Tetragonal phase, HTT). For low temperatures, often the orthorhombic $Bmab$ unit cell is used, with $a' \approx b' = \sqrt{2}a = 5.38$ (Low Temperature Orthorhombic phase, LTO). Though no indication for a structural phase transition was found in the system, in the following we will refer to the LTO notation. In this notation the charge stripes extend along the b' direction. The superstructure can be described by means of the modulation vectors g_i , the position of the superstructure peaks, given in respect to the fundamental lattice reflections, being $G \pm g_i$; G representing the lattice vectors. For the $\text{La}_{1-x}\text{Sr}_x\text{NiO}_4$ system the modulation vectors are equal $g_1 = \pm(2\epsilon, 0, 1)$ for charge order and $g_2 = \pm(1 - \epsilon, 0, 0)$ for spin order [14]. The so-called, incommensurability (or location) parameter ϵ depends on the hole-doping level n_h and on the temperature [Ref]. For a doping level close to $1/3$, $\epsilon \approx n_h$ and almost no temperature dependence is observed. For lower and higher n_h , ϵ deviates from n_h and shows a strong trend to approach $1/3$ for higher temperatures [87].

The diffraction experiments were performed at the soft x-ray beamlines U49/2-PGM1 and UE52-SGM1 of BESSY, using the two-circle UHV diffractometer, designed at the Freie Universität Berlin (described in section 2.1), in horizontal scattering geometry. Reference soft-x-ray absorption measurements on $\text{La}_{1.8}\text{Sr}_{0.2}\text{NiO}_4$ and LaTiO_3 have been performed at the Dragon beamline of the NSRRC in Taiwan.

The preparation and orientation of the sample is described in Section 2.2. The sample was mounted with the a' and c' directions aligned parallel to the scattering plane (see inset of Fig. 4.1). The stripes in this geometry were aligned perpendicular to the scattering plane. This orientation, together with the chosen doping level ($\epsilon \approx 0.28$), allowed us to reach two superstructure reflections: one belonging to spin order and one to charge order, in a single two-circle scattering setup. The investigated diffraction peaks were: $(2\epsilon, 0, 1)$ - charge order and $(1-\epsilon, 0, 0)$ - spin order peak at the La $M_{4,5}$ and Ni $L_{2,3}$ resonance (see Fig. 4.1) and the fundamental $(0\ 0\ 2)$ peak at 1010 eV energy. The fundamental Bragg peak was used to define the orientation of the sample. The momentum resolution at the k -points of the two superstructure peaks was estimated to: 0.0016 r.l.u. (0.0022 r.l.u.) along the H-direction and 0.0075 r.l.u. (0.0064 r.l.u.) along L-direction for the charge order (spin order) peak. Due to the large detector slit in the vertical scattering direction it can be assumed that the main part of intensity of the two peaks was detected along the K-direction (see Section 2.1).

We took energy scans of the charge order and spin order peak across the Ni and La resonances, as well as scans along the H- and L-direction in k -space. The measurements were performed for different temperatures in the range of 40-140 K. The polarization of the photon beam was linear either parallel (π polarization) or perpendicular (σ polarization) to the scattering plane. The energy resolution was approximately 300 meV and the beam spot on the sample smaller than $100 \times 100 \mu\text{m}^2$. No polarization analyser was used.

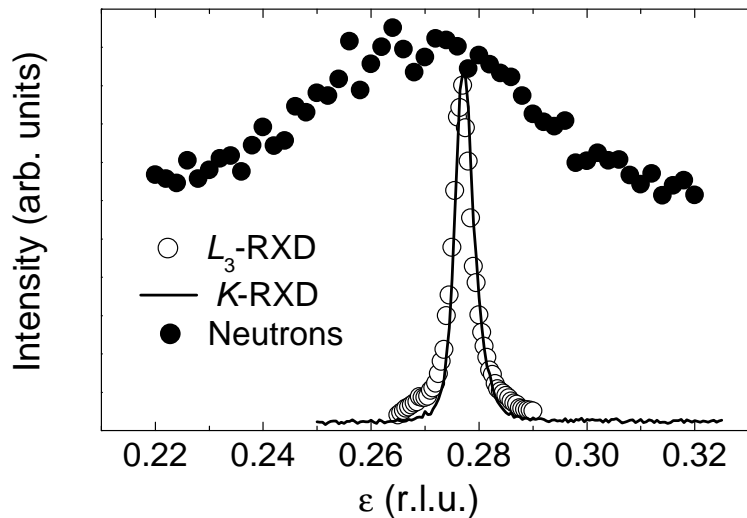


Figure 4.2: Diffraction data from the charge order: $(2\epsilon, 0, 1)$ -reflection measured with soft x-rays at the Ni L_3 -resonance at 60 K (open symbols), $(2-2\epsilon, 0, 3)$ -reflection measured with x-rays at the Ni K -edge at 60 K (solid line) and $(4-2\epsilon, 0, 1)$ -reflection measured with neutrons at 50 K (filled symbols).

4.3 Bulk sensitivity

The right side of Fig. 4.1 shows scans through the superstructure peaks along H- and L-direction at the Ni L_3 resonance, using π -polarized light. From the peak widths we determine the correlation length along a' to about 200 Å for charge order and to about 300 Å for spin order. The order along the c direction is less developed with correlation lengths of 50 Å (40 Å) for spin (charge) order. These values indicate that the stripe-order has a strong 2-dimensional character.

Soft x-ray diffraction is relatively surface sensitive; in comparison with neutron diffraction or standard x-ray diffraction, and the near-surface region may have therefore properties different from the bulk, either due to the surface treatment or due to oxygen loss near the surface. Therefore we compared the soft x-ray diffraction results to bulk-sensitive neutron diffraction data and Ni- K -edge resonant diffraction in the conventional x-ray range. For each technique we used different pieces of the same single crystal. The results for the charge order peak are presented in (Fig. 4.2). The scans were taken along the H-direction in k -space going through the equivalent $(4-2\epsilon, 0, 1)$ peak for the case of neutron diffraction, $(2-2\epsilon, 0, 3)$ for K -edge diffraction and $(2\epsilon, 0, 1)$ for $L_{2,3}$ -edge diffraction. No background subtraction was applied. The peak positions, which are sensitive indicators of the doping level, agree for all methods, showing that the volume probed by soft x-ray diffraction is indeed representative for the bulk. On the other hand the peak width differs considerably between the neutron and the x-ray data: the $(2\epsilon, 0, 1)$ soft x-ray peak (filled symbols) is a sharp Lorentzian with the FWHM of 0.011 r.l.u., similar to the K -edge data. In contrast, the $(4-2\epsilon, 0, 1)$ neutron peak has a triangular shape and is about 10 times broader.

The origin of this discrepancy is a certain amount of inhomogeneity of the doping

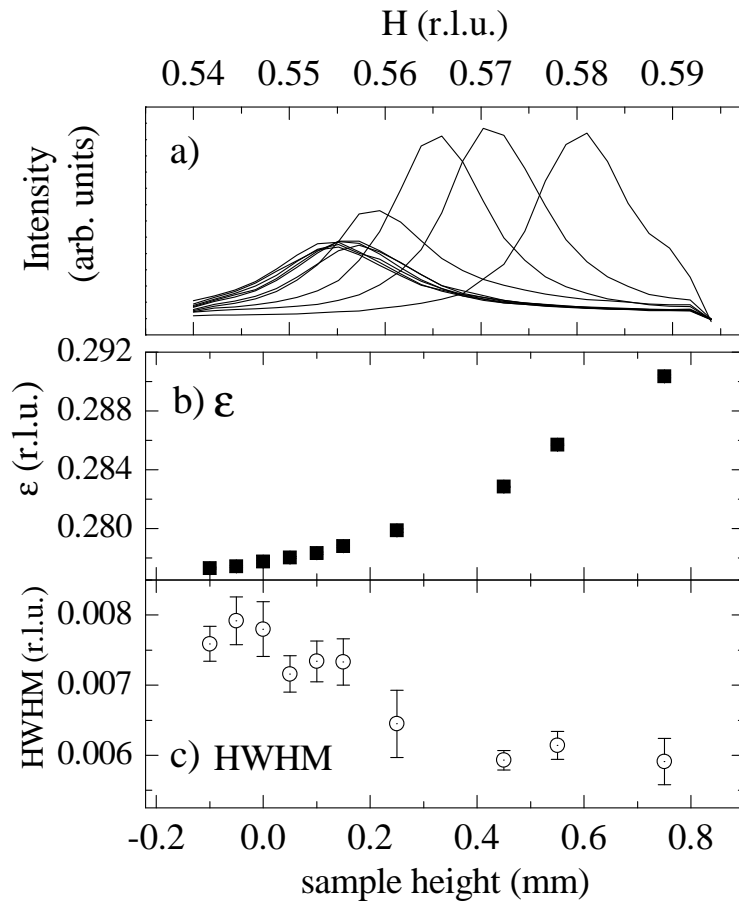


Figure 4.3: a) Scans along the H-direction across the charge order peak for different vertical positions of the sample (different sample height), b) variation of the incommensurability parameter ϵ and c) variation of half-full width of the charge order peak, as functions of the sample height.

level in the sample, which becomes obvious when we scan the well focused soft x-ray beam across the sample. The results are presented in Fig. 4.3. In the top panel scans through the charge order peak recorded at different sample heights are shown; below, the peak position as given by ϵ and the peak width is plotted. By changing the position of the sample by 1 mm the incommensurability parameter ϵ shifts from 0.278 to 0.291. Since ϵ depends on the doping level, this finding clearly demonstrates that the amount of doping varies across the crystal. Assuming that the difference is mainly due to the oxygen content, which may vary slightly during the growth process, and assuming further that $\epsilon \approx n_h$, the gradient in ϵ corresponds to a difference in the oxygen content of about 0.01, which is ≈ 0.3 percent of the total oxygen content.

It is instructive to compare the peak width found here to other results from the literature. For a sample with $x = 0.225$ and a value of ϵ similar to ours, a width of the magnetic peak of 0.007 \AA^{-1} corresponding to a correlation length of 150 (\AA) was found [78], which is about half of our result. From the systematics presented in Ref. [87] an in-plane correlation length of about 50 \AA for charge order and of about

200 Å for spin order can be expected. The correlation length observed with soft x-ray diffraction is well above all these values, showing that within the respective sample volume the order is very well developed. To ensure that all data were taken from the same position on the sample, the soft x-ray experiments were carried out in a region where ϵ depends little on height (around 0.0 mm-position in Fig. 4.3c). For each temperature this region could be safely identified from position-dependent scans. Interestingly, the tendency of charge order to be better developed for ϵ values closer to $1/3$ [87] can be seen from the height-dependent scans on one single sample, as well. When the peak position shifts toward higher H-values, it becomes narrower (Fig. 4.3c) and more intense (Fig. 4.3a).

4.4 Spectroscopic analysis

The energy dependence of the superstructure diffraction peaks was measured across the La $M_{4,5}$ and the Ni $L_{2,3}$ edge and compared with the spectra of the optical data. Fig. 4.4 shows the absorption (XAS) and reflectivity spectrum, together with that of the charge order $(2\epsilon, 0, 1)$ and spin order $(1 - \epsilon, 0, 0)$ reflections, obtained with two different linear polarizations (π and σ). The optical and the diffraction data have a totally different energy dependence. While XAS and reflectivity spectra show a strong resonance at the La $M_{4,5}$ edges (833 eV and 849.2 eV) and a weak signal at the Ni $L_{2,3}$ resonances (851.6 eV and 868.6 eV), the diffraction signals are strongly amplified at both Ni edges, resonating little at the La resonances. This is not just a self-absorption effect, since both diffraction spectra were corrected for the variation of probing volume across the resonance, according to Section 1.1.3.

As already discussed in Section 1.3 and Chapter 3, XAS and reflectivity signal are determined by the average optical properties of the entire system, whereas the diffraction signal is sensitive only to an ordered part with a certain periodicity. The gain in contrast at the Ni edge for both diffraction peaks demonstrates that the superstructure exists in a sublattice within the $\text{La}_{1.8}\text{Sr}_{0.2}\text{NiO}_4$ system, which is formed to a large extent by the Ni ions. The magnetic, as well as the charge order, must therefore involve Ni ions rather than La ions, meaning that not only the magnetic moments, but also the doped charges are located at (or in the direct vicinity of) the Ni ions. The fact, that there is a small enhancement observed at the La resonance, which has essentially the same magnitude in the spectra of both peaks, suggests a weak coupling between the Ni and La sites as well. This could be caused for instance by a weak hybridization or by the influence of NiO_6 octahedra distortion on the neighboring La sites.

The spectral shapes of the charge-order and spin-order spectrum are different, reflecting that the contrast mechanisms responsible for the existence of the two diffraction peaks are different as well. The observation of a charge-order signal is due to different energy dependences of the $(2p \rightarrow 3d)$ excitation process for two ions with an other oxidation state, here Ni with and without the extra positive charge (formally Ni^{3+} , Ni^{2+}). An excitation at a 3+ ion will always cost more energy than the excitation at a 2+ ion.

The dipole contribution to the resonant *magnetic* x-ray scattering amplitude

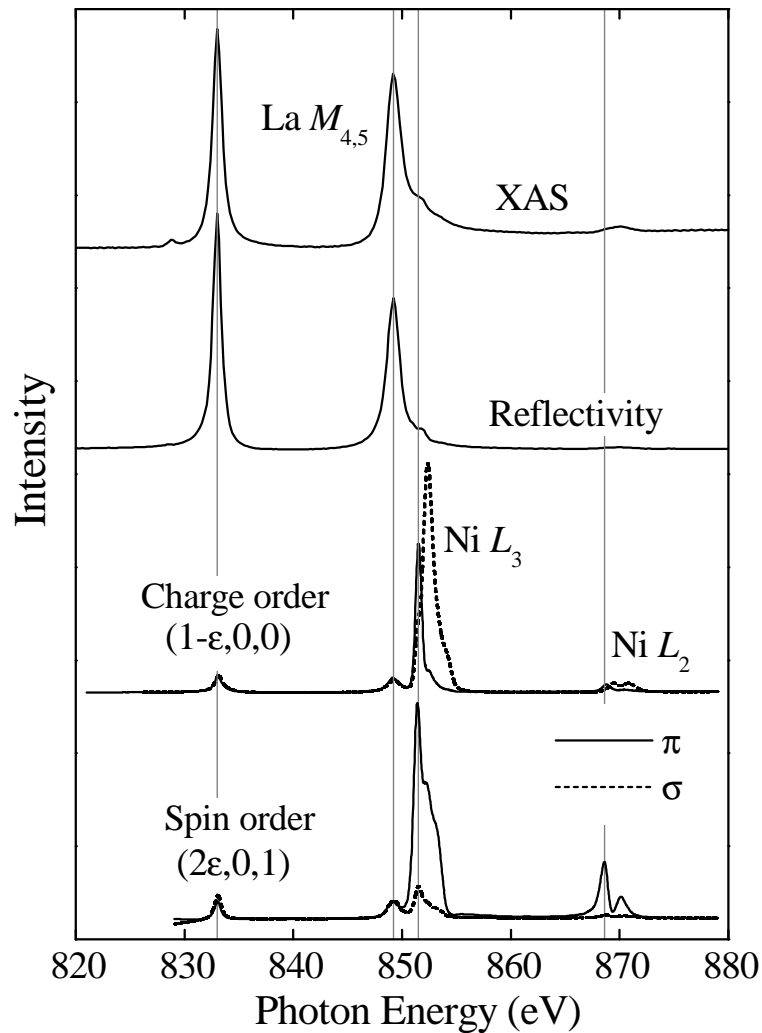


Figure 4.4: Energy dependence of x-ray absorption (XAS), reflectivity, charge-order ($2\epsilon, 0, 1$) and spin-order ($1 - \epsilon, 0, 0$) reflection (diffraction signal measured at 60 K). Reflectivity data were measured with π -polarized light and the superstructure data with π - (solid line) and σ - (dashed line) polarized light.

is described by three terms [50]. One of them has essentially the same momentum dependence as the fundamental Bragg peaks and does hence not give rise to superstructure reflections. The two remaining contributions are related to circular-dichroism and linear dichroism. The linear-dichroic term is not relevant here either, because the system is known to be collinear antiferromagnetic such that all terms proportional to the absolute value of the magnetic moment give no contrast. The magnetic scattering is hence due to the circular dichroic effects. The corresponding scattering cross section is proportional to $(\hat{e}' \times \hat{e}) \cdot \hat{m}$ with \hat{e}' and \hat{e} being unit vectors along the polarization of the outgoing and incoming photons and \hat{m} a unit vector along the local magnetic moment. Consequently only the magnetic moment perpendicular to the polarization of the incoming photons is probed.

The polarization dependence of both diffraction signals in the $\text{La}_{1.8}\text{Sr}_{0.2}\text{NiO}_4$

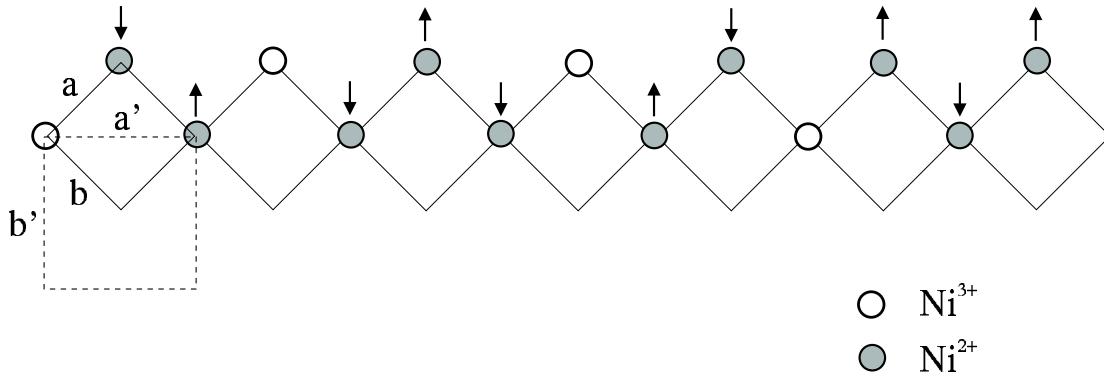


Figure 4.5: Superstructure unit cell used for the cluster modeling calculation; a, b (a', b') coincide with the lattice vectors of the tetragonal (orthorhombic) crystal structure and the solid lines (dashed line) denote the corresponding crystal unit cell. The arrows indicate the spin orientation on the Ni^{2+} sites, \uparrow : spin-up and \downarrow : spin-down.

system is strong, as evidenced by Fig. 4.4. Looking at the spin-order peak, one observes that the signal obtained with σ -polarization is about ten times weaker than the signal for π -polarization. The weak σ -signal indicates that the spin orientation at the Ni-sites is almost, but not perfectly, perpendicular to the scattering plane. The canting angle with respect to the b' direction is approximately 15 deg.

The polarization dependence for the charge order peak shows itself in an energy shift between the π and σ polarization signal, which is as large as 1 eV. Additionally, the resonance for σ polarization is about 50% stronger than for π polarization. To understand this difference, it is necessary to look at the orbital occupation at the Ni ions. The ground state of Ni^{2+} is $3d^8$, meaning that all t_{2g} states are fully occupied and both e_g states singly occupied ($t_{2g}^6 e_g^2$). The ground state of Ni^{3+} is $t_{2g}^6 e_g^1$, the extra hole being located in an e_g state. The $2p \rightarrow 3d$ transition can therefore lead only to the population of an e_g state on both sites. The experimental geometry was such (Fig. 4.1), that the e_g states with the $3z^2 - r^2$ symmetry were oriented parallel to the scattering plane, whereas the $x^2 - y^2$ states had a component in the scattering plane, as well as in the out-of-plane direction. Therefore σ -polarized light could lead mainly to the population of the $x^2 - y^2$ state, whereas π -polarized light to excitation into both orbitals, the probability for the population of $3z^2 - r^2$ being slightly higher. The ~ 1 eV energy shift between the π and σ spectrum is therefore an evidence for a large energy split between the two e_g states, with the $x^2 - y^2$ state lying higher in energy - and therefore for a large crystal field. As a consequence, the extra hole at the Ni^{3+} is expected to be located mainly in the state with the $x^2 - y^2$ -symmetry, which is extending in the (a, b) -crystal plane.

4.4.1 Microscopic modeling

The qualitative analysis of the diffraction spectra delivers already very valuable information about the electronic state of the $\text{La}_{1.8}\text{Sr}_{0.2}\text{NiO}_4$ system. More detailed information can be obtained however through a microscopic modeling of the diffraction spectra, as provided by the already discussed cluster model calculation.

The cluster modeling of our $\text{La}_{1.8}\text{Sr}_{0.2}\text{NiO}_4$ data was performed by Arata Tanaka from Hiroshima University, according to the method presented in Ref. [59]. In this model each Ni^{2+} (Ni^{3+}) ion site is described as a NiO_6^{10-} (NiO_6^{9-}) cluster with D_{4h} symmetry, taking into account the Ni $2p$ and $3d$ one-electron states and $2p$ states of the neighboring oxygens. The transition tensor for the resonant scattering process is given by Equation (1.10) in Section 1.2.2, the dominant second order scattering process being the electric dipole (E1) $2p \rightarrow 3d$ transition. The ground state of the NiO_6 cluster corresponds to a $2p^6 3d^n$ configuration. The eigenstate $|n\rangle$ and eigenenergy E_n of the ground state is fully described by considering Coulomb and exchange interactions between Ni $3d$ electrons, spin-orbit interaction for the $3d$ electrons and hybridization between the Ni $3d$ and the oxygen $2p$ orbitals. Additionally, a small molecular field H_{mol} is applied for the Ni^{2+} sites to induce spin moments. The intermediate states correspond to the $2p^5 3d^{n-1}$ configuration. Calculating the Hamiltonian H_m , Coulomb and exchange interactions between the $3d$ electrons and the $2p$ core hole and $2p$ spin-orbit interaction are additionally considered.

Taking into account the polarization dependence for an E1-transition with linearly polarized light, the diffracted intensity of the entire unit cell (see Fig. 4.5) is calculated applying the equation:

$$I(\omega) = \left| \sum_n e^{i\vec{q}\vec{r}_n} \vec{\varepsilon}' \cdot \hat{f}_n(\omega) \cdot \vec{\varepsilon} \right|^2 \quad (4.1)$$

as shown in Chapter 1.2. The vectors \vec{r}_n represent the positions of the Ni sites and $\hat{f}_n(\omega)$ the corresponding scattering tensors. The scattering vector, \vec{q} , is given through the position of the structure peak in the reciprocal space: $(2\varepsilon, 0, 1)$ for charge order and $(1 - \varepsilon, 0, 0)$ for spin order. The polarization unit vectors of the incident (ε) and diffracted (ε') beam are expressed in respect to the sample crystal axes. All information about the specific geometry of the diffraction experiment is then contained in the quantities \vec{q} , $\vec{\varepsilon}$ and $\vec{\varepsilon}'$. Each $\hat{f}_n(\omega)$ contains the relevant information about the electronic transitions at the respective site.

The unit cell of the superstructure used in the model is shown in Fig. 4.5. The cell is a linear zig-zag chain of Ni^{2+} and Ni^{3+} ions (more exactly the NiO_6^{10-} and NiO_6^{9-} clusters), each Ni^{2+} ion coupled antiferromagnetically to the closest Ni^{2+} ions. The neighboring cluster sites are spaced by the distance $a = 3.807 \text{ \AA}$, corresponding to the lattice constant of the tetragonal crystal structure. The permutation of this building block along the a' and b' -direction reproduces the stripe-order superstructure: an antiferromagnetic arrangement of Ni^{2+} ions, separated by hole rich Ni^{3+} antiphase domain-walls [8]. The average displacement between the neighboring Ni^{3+} stripes along the tetragonal a -direction is here equal to $7/2$, which corresponds to $\epsilon = 2/7 \simeq 0.286$. This is close to the observed incommensurability parameter $\epsilon = 0.28$ of the investigated sample.

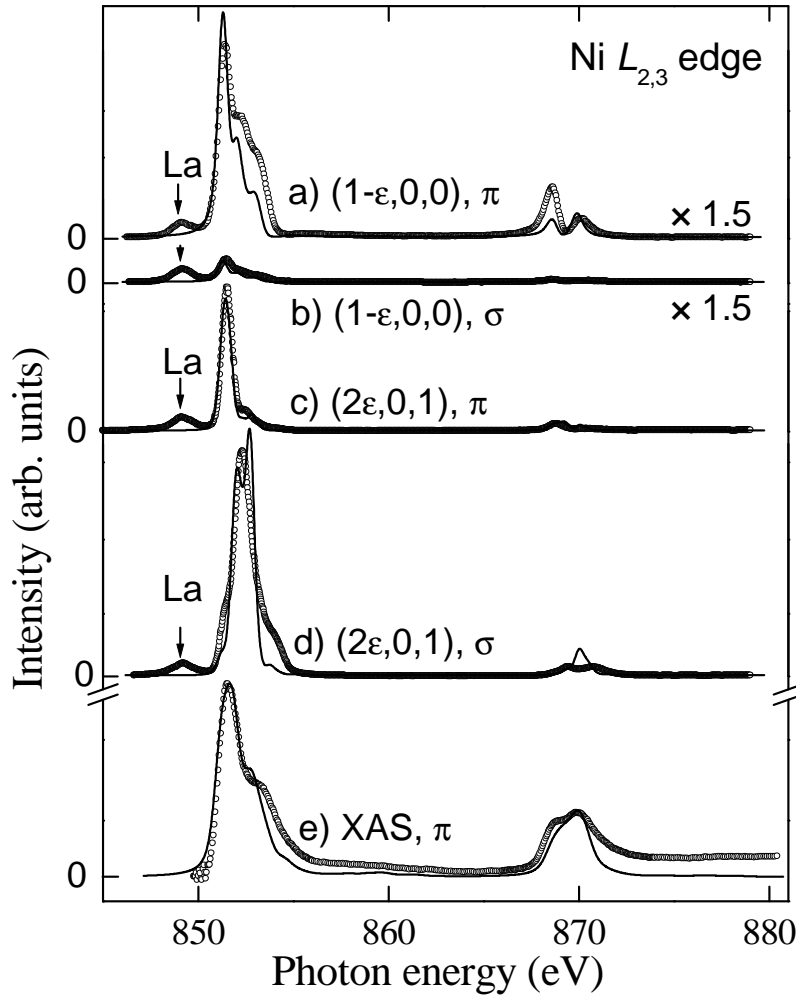


Figure 4.6: Comparison between measured data (symbols) and the results of cluster simulation. The simulated diffraction spectra have been scaled by one common factor to match the experiment. The La M_4 peaks at 849.2 eV, marked by arrows, are not included in the simulation.

The values for the cluster model parameters correspond to the standard ones used for nickeloxide materials [59]. The energies determining the Coulomb interactions were: $U_{dd}=7.0$ eV and $U_{dc}=8.5$ eV, the crystal field: $10Dq=0.5$ eV and the charge transfer energy: $\Delta_{2+}=6.5$ eV (for Ni^{2+}). We use: $(pd\pi) = -\sqrt{3}/4(pd\sigma)$. The chosen molecular field was equal $H_{\text{mol}} = 0.02$ eV. A new aspect is that the in-plane hopping integral $(pd\sigma)_1$ was set at a higher value than the out-of-plane $(pd\sigma)_2$, to account for the much shorter in-plane length for the Ni-O bonds, namely: $(pd\sigma)_1 = -1.88$ eV and $(pd\sigma)_2 = -1.12$ eV. The lifetime-broadening was set to $\Gamma_m = 0.15$ eV at the L_3 and 0.2 eV at the L_2 edge and a Gaussian broadening with a 0.2 eV-width (HWHM) was applied, which is close to the nominal resolution of the beam-line (0.15 eV).

With this single set of parameters, the shape of all diffraction spectra can be well described, including the relative intensities of the signals, as presented in Fig. 4.6. The model also reproduces the experimental Ni contribution to the x-ray absorption

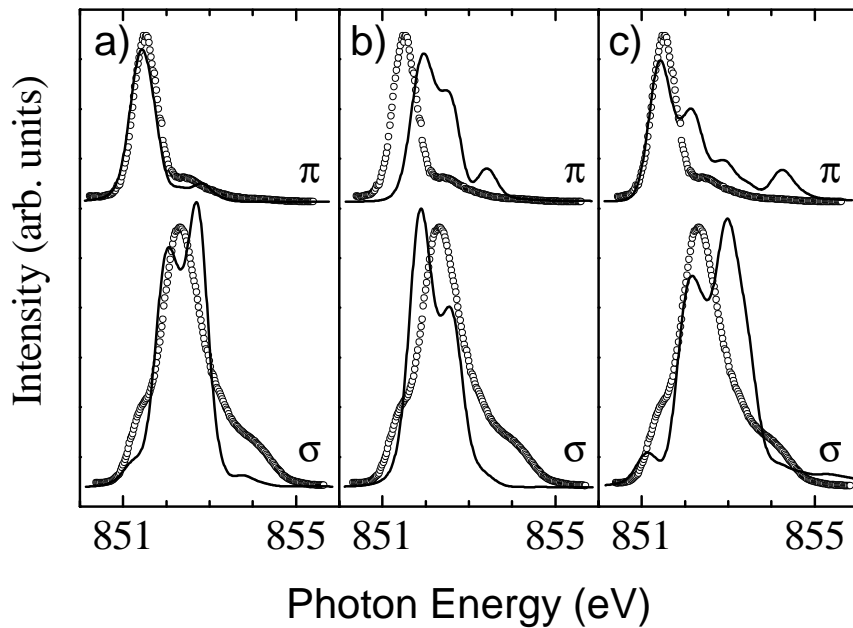


Figure 4.7: Sensitivity of the simulated spectra to the model as seen at the L_3 resonance of the $(2\epsilon, 0, 1)$ charge-order peak: the oxygen holes are a) confined in-plane and antiferromagnetically coupled to the Ni, b) not confined in-plane ($(pd\sigma)_1 = (pd\sigma)_2 = -1.88$ eV), c) ferromagnetically coupled to the Ni ($U_{dd} = 2$ eV). The circles are the experimental data.

spectrum (Fig. 4.6e), which was determined by subtracting out the La contribution obtained from LaTiO_3 . The agreement for the spin- and charge-order spectra is satisfactory. The energy positions of the peaks, shoulders and valleys are in most cases well reproduced, including the 1-eV energy shift between the π and σ polarization for the charge order L_3 resonance. There are deviations, e.g. at the L_2 resonance for the spin-order (π) and charge order (σ) and we speculate that perhaps the influence of the La ions needs also to be included in a more extensive model.

The analysis provides a detailed understanding of the ground state in the charge-ordered phase: At the Ni^{3+} sites, where the effective charge-transfer energy $\Delta_{3+} = \Delta_{2+} - U_{dd}$ is negative, the doped holes reside mainly in the oxygen ligand molecular orbital with $x^2 - y^2$ symmetry. The $3d$ electron count at the Ni^{3+} sites is as high as 7.9, which is surprisingly not much smaller than the 8.2 for the Ni^{2+} . The spins of the holes on the ligand and $3d$ orbitals couple antiferromagnetically and form an $S = 1/2$ state [39, 94] in which the Ni ion with $t_{2g}^6 e_g^2$ configuration is dressed with a hole in the $(x^2 - y^2) \uparrow$ ligand orbital. This state is analogous to the Zhang-Rice singlet state in a cuprate superconductor [95, 96]. This assignment is strongly supported by the observation that between the two polarizations there is a strong shift of about 1 eV in the peak maxima in each of the L_2 and L_3 edges of the $(2\epsilon, 0, 1)$ spectrum, which indicates a large energy splitting of the unoccupied $x^2 - y^2$ and $3z^2 - r^2$ levels.

In order to probe the reliability of our analysis we present in Fig. 4.7 also a scenario in which the oxygen hole is not confined in-plane (Fig. 4.7b) or is ferromagnetically coupled to the Ni (Fig. 4.7c). One can clearly see significant deviations from the experimental data (Fig. 4.7a) and the antiferromagnetic/in-plane scenario.

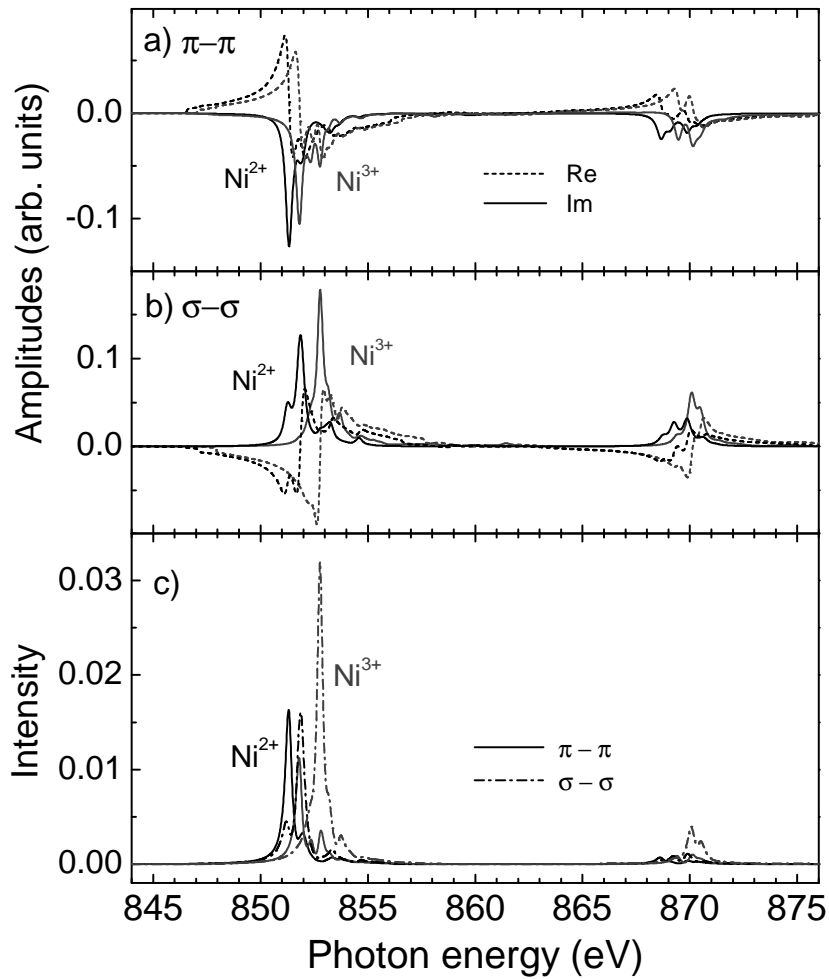


Figure 4.8: Charge order: the modeled scattering amplitudes for the Ni^{2+} (black) and Ni^{3+} (gray) sites in the $(2\varepsilon, 0, 1)$ scattering geometry for the $\pi - \pi$ (a) and $\sigma - \sigma$ (b) polarization channel. The solid (dashed) lines represent the imaginary (real) parts of the scattering amplitude. c) *Scattering* intensities at the two ions in the same geometry; solid line: $\pi - \pi$, dotted-dashed line: $\sigma - \sigma$ channel.

If the oxygen hole is not confined in-plane the 1-eV energy shift in the polarization dependence is missing and the lineshape of the π signal is too broad; if the oxygen hole is ferromagnetically coupled, there is by far too much intensity on the high-energy side of the peaks.

It is instructive to study the scattering signals of the single NiO_6 clusters involved in the formation of the charge and spin order, as they result from the model calculation. Fig. 4.8 and 4.9 display the charge order $(2\varepsilon, 0, 1)$ and spin order $(1 - \varepsilon, 0, 0)$ data, respectively. The upper two diagrams in the figures display the scattering amplitudes; $\vec{\varepsilon}' \hat{f} \vec{\varepsilon}'$, of the contributing clusters, corresponding to the: (a) $\pi - \pi$ and (b) $\sigma - \sigma$ channels. The dashed (solid) lines correspond to the real (imaginary) parts. The bottom diagrams (c) show the *scattering* intensities; $|\vec{\varepsilon}' \hat{f} \vec{\varepsilon}'|^2$, for $\sigma - \sigma$ (dashed line) and $\pi - \pi$ (solid line). The $\pi - \sigma$ and $\sigma - \pi$ channels are negligible small.

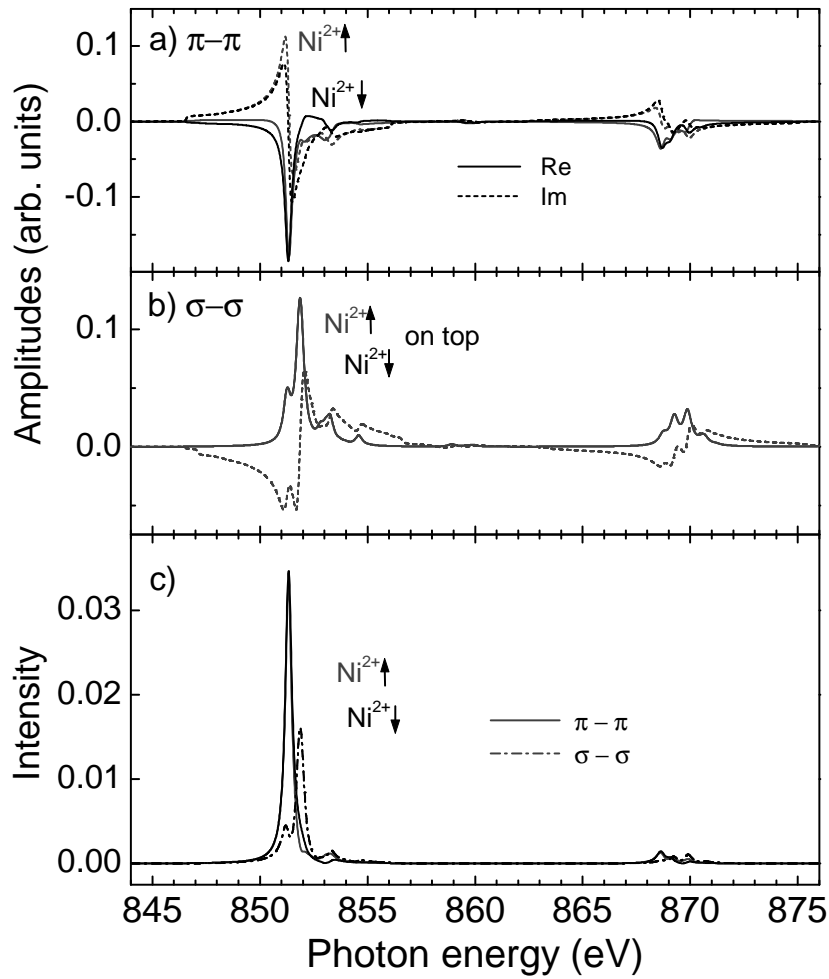


Figure 4.9: Spin order: the modeled scattering amplitudes for the $\text{Ni}^{2+\uparrow}$ (gray) and $\text{Ni}^{2+\downarrow}$ (black) sites in the $(1 - \varepsilon, 0, 0)$ scattering geometry for the $\pi - \pi$ (a) and $\sigma - \sigma$ (b) polarization channel. The solid (dashed) lines represent the imaginary (real) parts of the scattering amplitude. c) *Scattering* intensities at the two ions in the same geometry; solid line: $\pi - \pi$, dotted-dashed line: $\sigma - \sigma$ channel.

The contrast leading to the appearance of $(2\varepsilon, 0, 1)$, Fig. 4.8, comes from difference between the electronic states of the Ni^{2+} (black color) and Ni^{3+} (gray color) clusters. The resonances of the Ni^{3+} clusters lie between 0.5 and 1.0 eV higher than the resonances of Ni^{2+} , due to the higher valence. Because of the crystal field splitting, the $\sigma - \sigma$ channels are shifted toward higher energies in respect to $\pi - \pi$. The scattering intensities for Ni^{2+} , having partly occupied $3z^2 - r^2$ and $x^2 - y^2$ orbitals, are basically the same for the two scattering channels, whereas the $\sigma - \sigma$ intensity for Ni^{3+} is at least twice as large as for $\pi - \pi$, since $3z^2 - r^2$ is partly occupied and $x^2 - y^2$ empty.

The curves in Fig. 4.9 refer to non-canted spins. The differences between $\text{Ni}^{2+\uparrow}$ and $\text{Ni}^{2+\downarrow}$ are less pronounced than between Ni^{2+} and Ni^{3+} , but obviously large enough to produce a strong diffraction peak in the $\pi - \pi$ channel. In the $\sigma - \sigma$ channel the scattering amplitudes are identical, due to the lack of magnetic contribution.

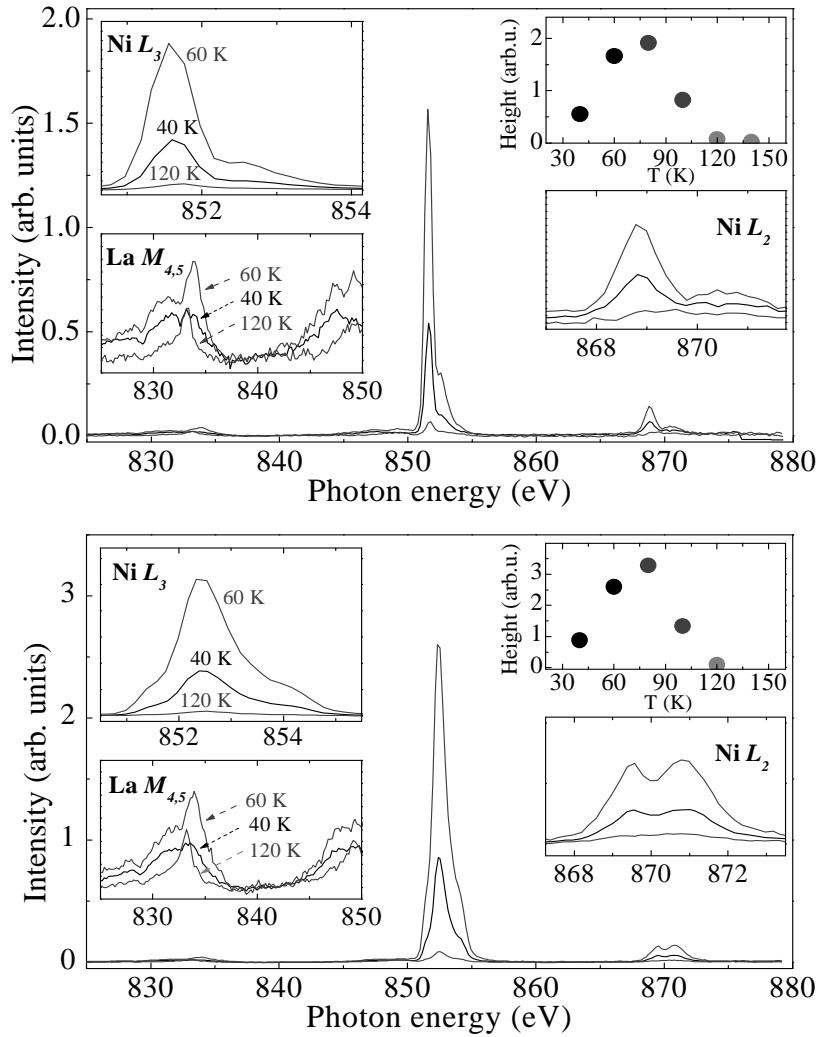


Figure 4.10: Temperature dependence of the charge-order spectrum for π - (upper) and σ - (lower) polarization for 40, 60, and 120 K. The insets show an enlarged view on the Ni L_3 resonance (upper left corner), Ni L_2 resonance (lower right), La $M_{4,5}$ resonance (lower left) and the peak height at the Ni L_3 resonance (upper right).

Since $\sigma - \sigma$ does not depend on the direction of the incoming and scattered light, the $\sigma - \sigma$ signal is the same for a cluster in the scattering geometry corresponding to the charge order and to the spin order peak. It becomes apparent from comparison of the $\sigma - \sigma$ Ni^{2+} data in Fig. 4.9 and Fig. 4.8 [e.g. Fig. 4.9b) and black curves in Fig. 4.8b)].

4.5 Temperature dependence

It has been discussed in the literature, whether the type of bonding of the holes is conserved with temperature or whether a transition occurs between the bond-centered and metal-centered stripes with temperature [81, 97]. Since resonant soft x-ray diffraction is extremely sensitive to the electronic character of the order, such

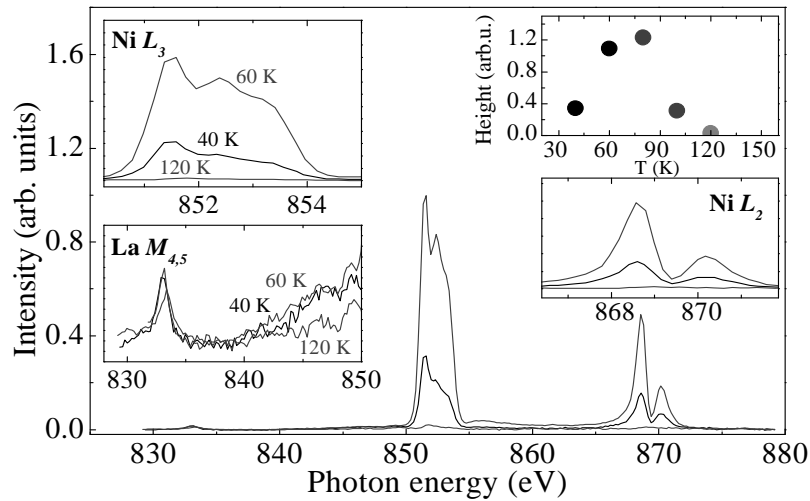


Figure 4.11: Temperature dependence of the spin-order spectrum for π -polarization for 40, 60, and 120 K. The insets show an enlarged view on the Ni L_3 resonance (upper left corner), Ni L_2 resonance (lower right), La $M_{4,5}$ resonance (lower left) and the peak height at the Ni L_3 resonance (upper right).

a change would lead to a significant change of the diffraction spectra. We studied the temperature dependence of the spectral shape of the charge and spin order peak between 37 and 135 K. The shape of the spectra taken at 40 K, 60 K and 120 K are presented in Fig. 4.10 for charge order and in Fig. 4.11 for spin order. Shown are raw data without corrections for change of the probing volume, which in any case would affect all spectra in a similar way. The peak intensity as determined from the height of the maximum of the L_3 resonance is plotted in the insets in the respective upper right corner. For both peaks, this quantity has a maximum around 80 K and decreases towards higher and towards lower temperatures. The shape of the spectra does not change in the measured temperature range; in particular the shape across the Ni $L_{2,3}$ resonance (upper left and lower right insets) remains exactly the same, clearly ruling out a change of the character of the order with temperature. The apparent change of the spectrum in the region of the La- M_5 resonance (lower left insets), where at high temperatures a peak occurs at 833.2 eV is due to the increasing thermal diffuse background, which has exactly the position and a similar shape to the reflectivity spectrum in Fig. 4.4. Evidences for strong diffuse scattering in $\text{La}_{1-x}\text{Sr}_x(\text{Ni,Cu})\text{O}_4$ systems have been reported previously [98].

What does change with temperature is among others the intensity ratio of the π and σ spectra of the spin-order peak as presented in Fig. 4.12b) in comparison with the charge-order signals in 4.12a). Both curves show the height of the maximum of the L_3 resonance above the background, normalized to the 60 K value; for the spin-order peak, the scaling was chosen such that the agreement at 60 K is within the error bars and the overall agreement of the curves is maximized. While for the charge-order peak the π and σ channel show essentially the same temperature dependence, the deviations in the spin-order peak are noticeable. In particular for low and high temperatures, the intensity ratio of the two polarizations decreases,

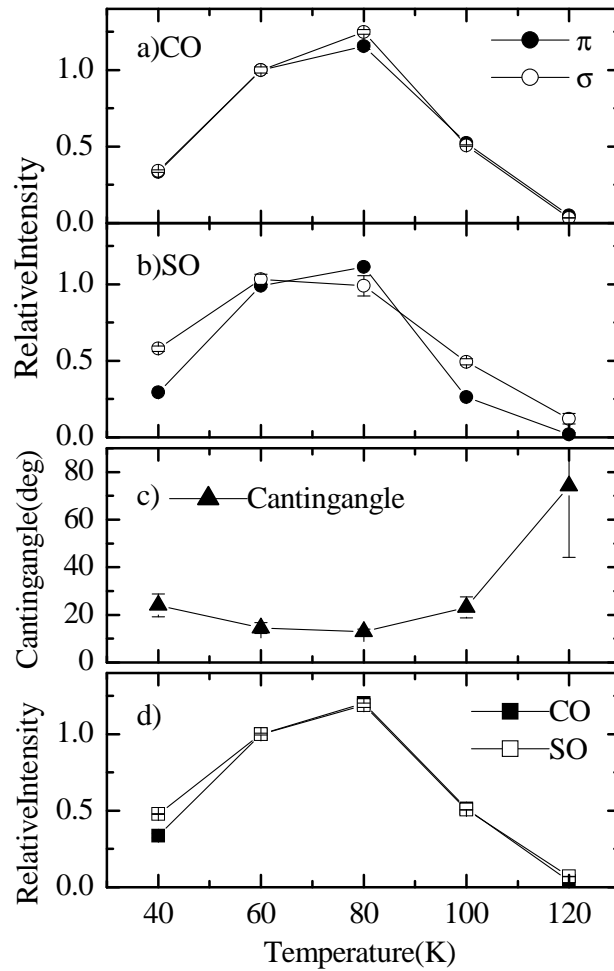


Figure 4.12: Intensity of the maximum of the L_3 resonance vs. temperature for a) the charge-order signal and b) the spin-order signal. c) Canting angle as determined from the relative intensity of the spin-order signals. d) Average of the CO signals from a) compared to the squared magnetic moment determined from the two SO curves. For comparison the curves in a) and d) have been normalized at 60 K, the SO curves in b) are normalized to within the error bars at 60 K.

showing an increasing canting angle towards lower and higher temperatures. At 40 and 100 K the intensity ratio between π and σ is only around 4, corresponding to a canting angle of around 25 degrees [Fig. 4.12c)] For 120 K the two signals are almost equal, which means that the spins are pointing essentially perpendicular to the stripes; the overall signal is too weak for a precise determination of the spin direction, though. A spin reorientation has been reported before for different doping levels [85, 88] mainly for the temperature range between 2 K and intermediate temperatures, with the same trend of a larger canting angle at low temperatures as was found here. A similar spin reorientation when going to higher temperatures has not been reported yet.

The overall temperature dependence for the charge and spin order signal is very similar as can be seen from the curves in Fig. 4.12d) where the average of the two

charge-order signals (filled symbols) and the total spin-order signal (open symbols) is shown. The latter was calculated from the spin-order signals in the two polarization channels such that the variation of the canting angle is considered. Both signals were here also normalized at 60 K for comparison. Both curves go through a maximum at 80 K and decrease towards higher and lower temperatures. Focusing first on the high-temperature behavior the similarity of spin and charge-order signal is quite surprising. So far almost all diffraction experiments for all doping levels found a distinctly lower ordering temperature for the spin-order than for the charge order signal and consequently a clearly different temperature dependence [14, 74, 77, 78, 85]. An exception is the neutron diffraction work of Sachan et al., who found for an $x = 0.2$ sample the same temperature dependence for spin and charge order when they were looking at the *energy-integrated* spin-order signal [13], while the elastically scattered magnetic signal decayed much faster upon heating. A similar persistence of magnetic correlations far above T_N was observed for an oxygen-doped system with $\delta = 0.05$ [99]. While we performed no energy analysis of the scattered intensity, from resonant inelastic x-ray scattering (RIXS) experiments it is known that the inelastic signal is very weak and should be comparable to the (in our case barely observable) fluorescence background [100]. Comparing the time scales, x-ray scattering will be the faster method and therefore more sensitive to fluctuations than, e.g., neutron diffraction. (One, of course, has to consider that the probed quantity is different in different scattering experiments.)

An intriguing feature of the temperature dependence is the decay of the peak height of the diffracted intensity towards lower temperatures, which appears to be symmetric to the high-temperature behavior. For the overall temperature dependence different results have been published in the literature. Neutron diffraction mostly observed a saturation of the charge order and spin order intensity at low temperatures [13, 14, 74, 77, 78, 85], while in conventional x-ray diffraction experiments a temperature dependence similar to the one presented here was found with an initial increase of the charge order signal upon heating and a maximum around 80 K (110 K) for $x = 0.275$ ($x = 0.30$), followed by a gradual decrease toward zero [82, 89].

In order to characterize the temperature dependence better we recorded the data in a more dense set with π -polarized light. These data were taken from a different part of the sample where the ϵ value is slightly higher (2.775 at 60 K as compared to 2.765 for the first data set). The temperature dependence of the signal at the L_3 -resonance maximum as shown in Fig. 4.13a) is very similar to the one in Fig. 4.12 with the maximum occurring at 70 K in this case. Again the temperature dependence of the charge-order and spin-order signal is the same. The decrease of the peak height at high and at low temperatures is accompanied by a substantial broadening of the peaks over a very wide temperature range, as can be seen from the scans through both peaks in Fig. 4.14 and from the extracted widths in Fig. 4.13 b) and c). This behavior is quite different from a usual second-order phase transition, where a substantial broadening occurs only in a narrow temperature interval below the transition temperature and above. For the high-temperature range this has been noticed before in different studies for low doping levels. Together with the overall short correlation length in these systems it has been assigned to a freezing

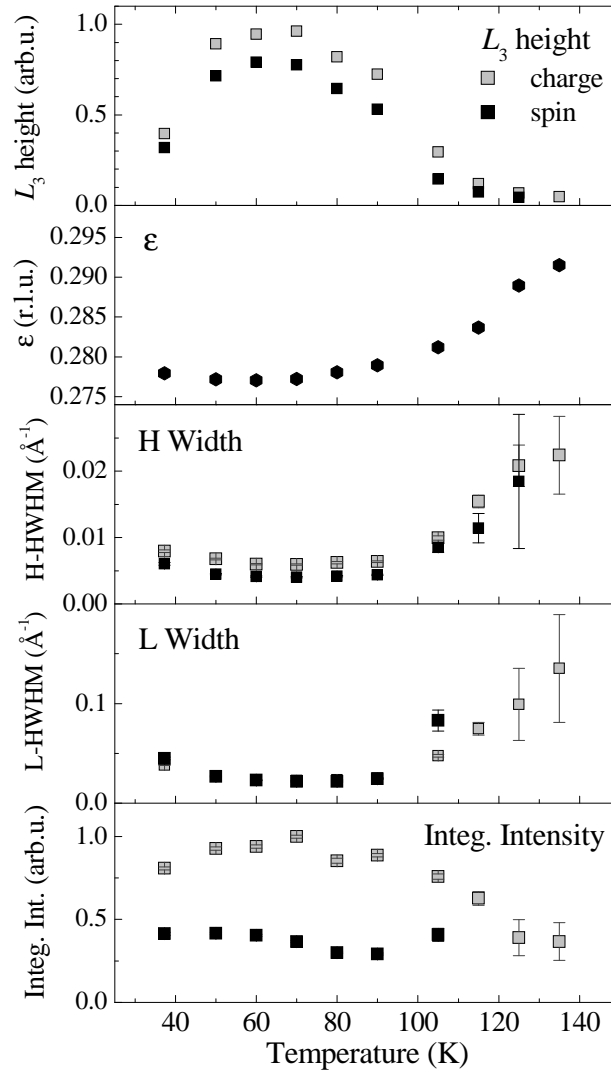


Figure 4.13: Temperature dependence of the charge order and spin order peaks: peak height (a), incommensurability parameter ϵ (b), widths of scans along H- (c) and L-direction (d) and the total integrated intensity (e).

of short-range correlations [13].

Since the decrease of the peak height is accompanied by a peak broadening in the q -space, the integrated intensity, which is proportional to the squared order parameter, does not decrease as fast as the peak height. We tried to estimate the integrated intensity as the product of the peak height and peak widths in H and L directions. We can do this safely without double counting of intensity, since the q -space resolution is about 10 times smaller than the peak width in these two directions. Along the third, K, direction we integrate over a larger interval because of the wide detector acceptance perpendicular to the scattering plane. The result of this estimate is shown in the lower frame of Fig. 4.13. The decrease of the peak height is to a large extent compensated by the increasing peak width; a large part of the integrated intensity is conserved up to high temperatures. We would like to

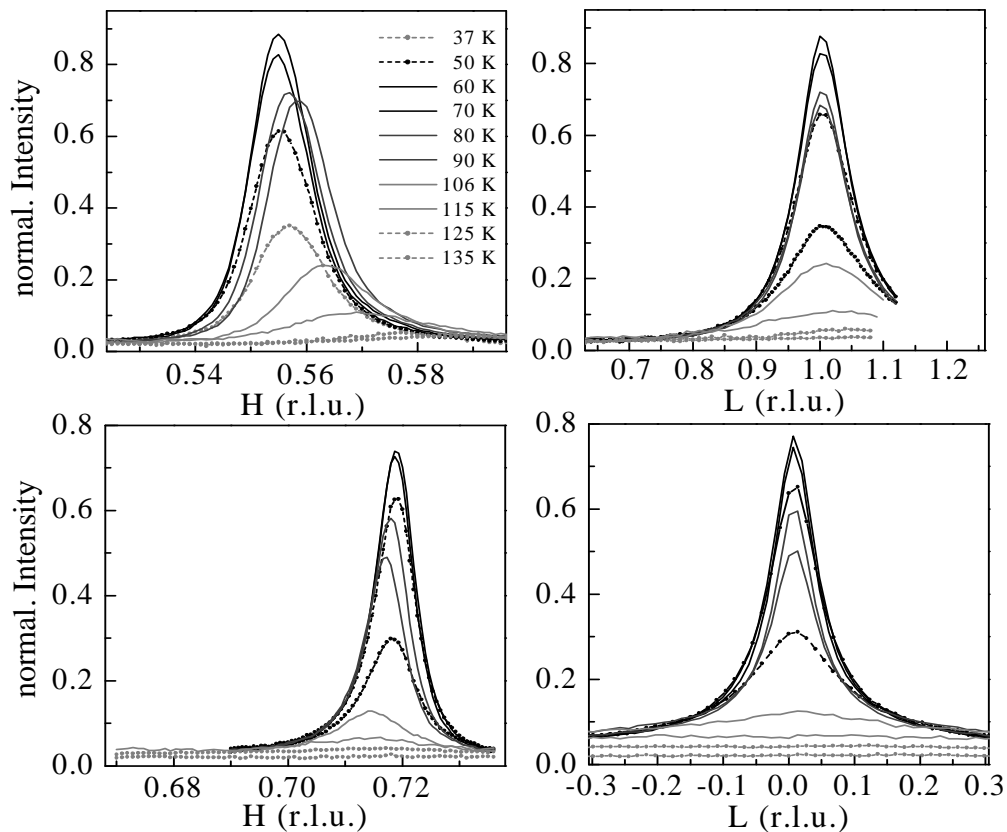


Figure 4.14: Increase of widths with temperature; H- and L-scan of the charge order (upper) and spin order (bottom) peak in the temperature range of 37-135 K.

stress that this estimate is based on the assumption of a rather regular line shape of the diffraction features. The peaks we found have an essentially Lorentzian line shape; a precise determination of the integral from a wide scan is however impossible because of the limited momentum space available. On the other hand if we assume the width along H and K to be the same, we rather underestimate the peak intensity at high temperatures because we integrate over the full K-width at 70 K, but only over about 20 percent of the width at high temperatures.

Independent from the precise quantitative value for the integrated intensity we can describe the temperature dependence as dominated by a loss of spatial coherence rather than by a decay of the order itself. The ordered part of the system breaks into smaller and smaller domains, while the order pattern and the ordered fraction of the sample is essentially conserved. Even the periodicity as seen from the value of ϵ [Fig. 4.13b)] does not change too much but shows the well known tendency to approach the most stable commensurate configuration with $\epsilon = 1/3$. The breaking into domains may facilitate this trend, because defects in the order pattern due to missing holes can be located in the domain walls; the stability of the $\epsilon = 1/3$ phase may even be the driving force for the loss of spatial coherence. The decrease of (integrated) intensity toward low temperatures could be an indication for pinning of the stripe order due to a disorder potential [101].

4.6 Discussion

To conclude, we have observed well developed superstructures in $\text{La}_{1.8}\text{Sr}_{0.2}\text{NiO}_4$ using resonant soft x-ray diffraction. The intensities of the spin-order and charge-order diffraction peaks show strong enhancements when x-ray energies are tuned to the vicinity of the Ni $L_{2,3}$ absorption edges. These observations show directly that not only the antiferromagnetic but also the charge order resides within the NiO_2 layers. The photon-energy and polarization dependence of the charge and spin-order diffraction intensity across the Ni $L_{2,3}$ edges can be reproduced by a quantitative microscopic model calculation assuming diagonal stripes of Ni^{2+} and Ni^{3+} -like ions, in which the Ni^{3+} -like objects are formed of a Ni^{2+} ion accompanied by a hole, which is essentially located at the surrounding in-plane oxygen ions in analogy to a Zhang-Rice singlet in cuprate systems. The good agreement between experiment and calculation indicates that differences in the hole concentration around the Ni ions, i.e. charge ordering, are the cause of the superstructure.

Chapter 5

Spectroscopy of charge and orbital order in Fe_3O_4

5.1 Magnetite (Fe_3O_4)

Magnetite, Fe_3O_4 , is one of the most fascinating materials in solid state physics. Besides being the first magnetic material known to the mankind, it is also the first example for an oxide to show a first order anomaly in the temperature dependence of the electrical conductivity at $T_V \approx 120$ K, the famous Verwey transition, where the conductivity drops two-orders of magnitude toward low temperatures [103].

At high temperatures magnetite has a cubic spinel structure with $a = 8.396$ Å (displayed in Fig. 5.1). There are two kinds of Fe-ions with a distinct local symmetry in the compound; $\frac{1}{3}$ of the irons is positioned in a tetrahedral crystal field, generated by the neighboring oxygens (the so-called A-sites) and $\frac{2}{3}$ in an octahedral crystal field (B-sites). The A-sites are trivalent, whereas the B-sites form a mixed-valent system with a formal valence of 2.5+. Due to this non-integer valency of the B-sites, the electrical conductivity of magnetite at high temperatures is moderate, the charges being mobile along the octahedrally coordinated B-sites (see Fig. 5.1). The system is a ferrimagnet with a high Néel temperature (~ 860 K), which is due to the anti-ferromagnetic coupling between the A-sites and B-sites (the coupling within the A and B-sites is ferromagnetic) and the resulting net magnetic moment.

The Verwey transition is accompanied by a structural phase transition from the cubic inverse spinel to a distorted, monoclinic structure, which leads to the appearance of superstructure diffraction peaks mainly characterized by the wave vectors (001) and $(00\frac{1}{2})$ (in the cubic notation). One usually connects this transition with the charge ordering (CO) of Fe^{2+} and Fe^{3+} ions on the B-sites. However, the detailed pattern of the CO in Fe_3O_4 , or in general the crystal structure, is still a matter of debate [104].

It was the recent diffraction study by Wright, Attfield and Radaelli using neutron and synchrotron-radiation from powder [102, 105], which has triggered a flurry of new theoretical and experimental studies [35, 106–116]. The authors found long-range charge order from the pattern of shorter and longer bond lengths between B-site iron and oxygen ions below T_V . They proposed a model for charge order based on an alternation of pure either divalent or trivalent layers and of mixed layers with

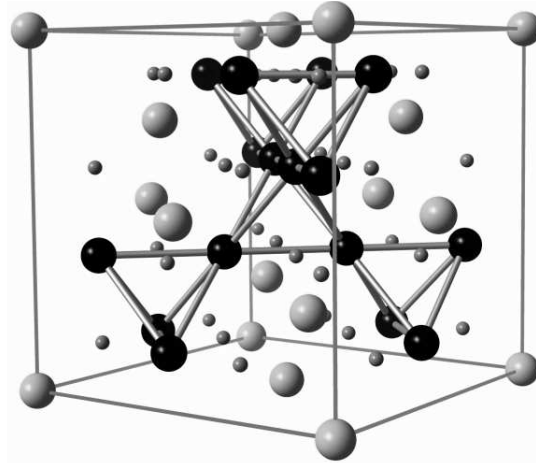


Figure 5.1: High-temperature phase of magnetite; unit cell of the cubic inverse spinel structure. The large spheres represent the iron-sites: octahedral B-sites (black) and tetrahedral A-sites (light-gray), whereas the small ones the oxygens.

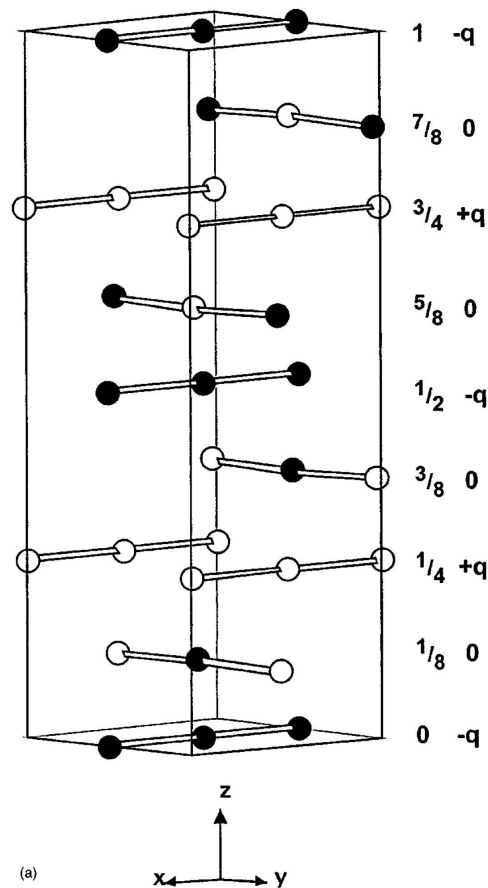


Figure 5.2: Low-temperature phase of magnetite, charge-order model proposed by Wright et al. [102]: the arrangement of the iron B-sites in the $P2/c$ cell. The closed (open) circles represent the formal Fe^{2+} (Fe^{3+}). (From Wright et al. [102])

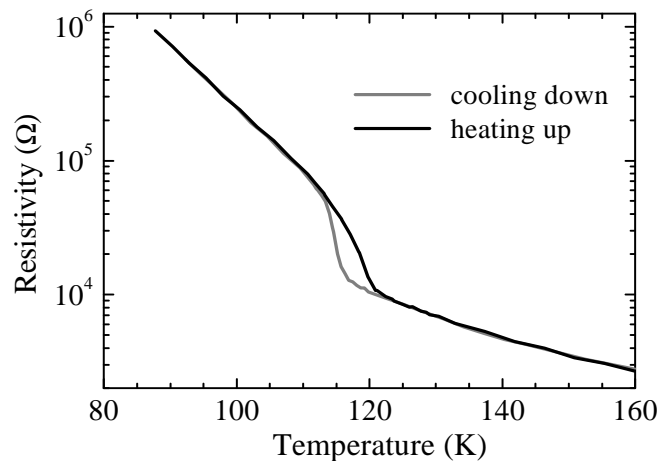


Figure 5.3: Resistivity of thin film Fe_3O_4 on MgO . [Measured by C. F. Chang]

both Fe^{2+} and Fe^{3+} ions along the c -direction (see Fig. 5.2). Characteristic for this model is that it does not meet the classic Anderson condition [117]. Subsequently, using this structure as input, local density approximation + Hubbard U (LDA+ U) band structure studies have calculated the corresponding orbital ordering [110, 111].

The interpretation by Wright and coworkers has been challenged by a resonant x-ray diffraction study at the iron K -edge [112]: from the intensity change across resonance of various diffraction peaks and from absence of the $(00\frac{5}{2})$ and $(00\frac{7}{2})$ peaks it was concluded that no charge modulation of more than a tenth of an electron charge can exist in this system. Very recently, however, resonant soft-x-ray diffraction (RSXD) of the $(00\frac{1}{2})$ diffraction peak at the O K -edge has been interpreted as evidence for iron charge-orbital ordering [35]. This interpretation, however, is entirely based on an LDA+ U calculation for the Wright-Attfield-Radaelli structure. The calculated photon-energy dependence of the diffraction peak intensity is claimed to agree sufficiently with the measured one as to warrant the conclusion that the peak is caused by the particular type of charge-orbital ordering as calculated by LDA+ U . It is, however, at the moment not clear why not all calculated features are visible in the measurements, and whether the $(00\frac{1}{2})$ peak must really be due to charge-orbital ordering rather than a pure orbital ordering in the Fe^{2+} sublattice.

Here we present a direct experimental determination of the Fe charge and orbital order by RSXD at the Fe $L_{2,3}$ edges. This approach has the major advantage that the electronic states of the transition-metal ion are probed directly [19, 25, 32] unlike at the O- K edge, where the sensitivity to Fe orbital ordering is based on the rather weak Fe t_{2g} -O hybridization. At the iron resonance, the assignment of the diffraction features can be made directly from the spectral shape without involving band-structure calculations.

5.2 Experimental

For this study we chose a magnetite film rather than a bulk crystal for two reasons. Firstly, diffraction features in a thin film are broadened along the surface normal.

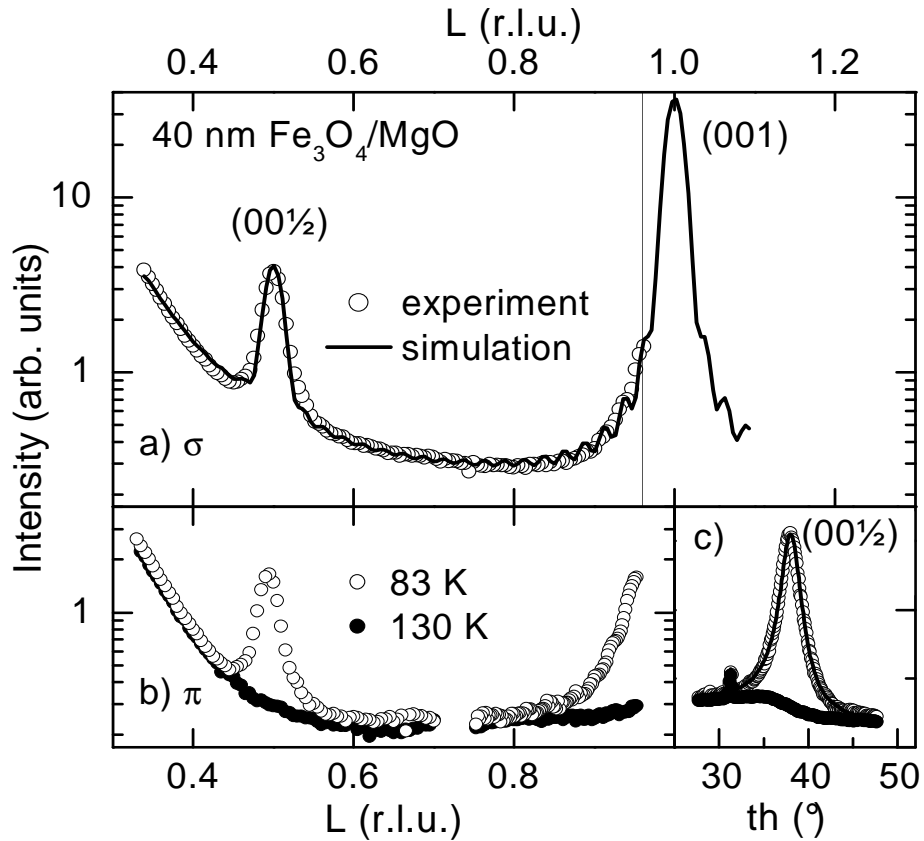


Figure 5.4: a) Scan along the L-direction below the Verwey transition, recorded at 708.5 eV photon energy. The solid line through the data points is a simulation. The vertical line at $L=0.96$ denotes the maximum possible momentum transfer at this energy (b) The same scan around $(00\frac{1}{2})$ and (001) reflections; below (open symbols) and above (filled symbols) T_V . (c) Sample rock around $(00\frac{1}{2})$ below (open symbols) and above (filled symbols) T_V , with a simulation (solid line).

This broadening allows us to study the resonance of the (001) peak, whose peak maximum cannot be reached at the $L_{2,3}$ resonance. Secondly, the volume probed by the scattering experiment is determined by the film thickness rather than by the photon penetration depth. Since the latter changes strongly across resonances in the soft x-ray range, this change may obscure the resonance effect.

A 40-nm film of Fe_3O_4 was grown ex-situ by molecular-beam epitaxy (MBE) on epi-polished MgO by C. F. (Roger) Chang. In order to separate the specular reflectivity from the c -direction of Fe_3O_4 , a substrate with about 6° miscut was used. The film was characterized by resistivity measurements, showing a sharp Verwey transition at 115 K (see Fig. 5.3).

Soft x-ray diffraction experiments were carried out at the BESSY beamline UE52-SGM using the UHV diffractometer built at the Freie Universität Berlin. The sample was oriented such that two of the cubic axes of the room temperature structure were parallel to the diffraction plane. The incoming light polarization was either perpendicular (σ -polarization) or parallel (π -polarization) to the diffraction plane.

5.3 Diffraction data

Fig. 5.4a) shows a q -scan along the $[001]$ or L direction of the reciprocal space taken at 83 K (open symbols), i.e. below T_V , with 708.5 eV photons and π -polarized light, revealing the $(00\frac{1}{2})$ diffraction peak, and the onset of the (001). The increase of intensity toward lower L is reflectivity background. Even though the maximum of the (001) cannot be reached at the Fe- $L_{2,3}$ resonance, where the maximum momentum transfer is $L=0.96$ as indicated by the vertical line, the broadening of the (001) peak transfers some intensity into the reachable momentum space. The solid line through the data points is a simulation including two peaks of the same shape but different intensity and the Fresnel reflectivity, which causes the increasing background at low L -values. This model describes the data reasonably well, even though the oscillations of the Laue profile are not resolved in the data. Both peaks disappear when the sample is heated to 130 K (filled symbols), i.e. above T_V [Fig. 5.4b)]. A rock around the $(00\frac{1}{2})$ peak, above (open symbols) and below (solid symbols) T_V , is displayed in Fig. 5.4c). The intensity around $\theta \approx 30$ corresponds to the reflectivity rod, which is offset by 6 from the $(00\frac{1}{2})$ reflection, pointing along the surface direction. The solid line is a Lorentzian over the background represented by the high temperature data.

From the peak widths in q -space we determine the correlation length perpendicular to the surface to be 37 nm, which is essentially the full film thickness. The in-plane correlation length of 10 nm is most probably limited by the formation of crystalline domains [106]. The influence of the stepped substrate on the structure of the film seems to be weak, since the in-plane correlation length is about 2.4 times larger than the width of the terraces on the MgO surface.

In order to identify the origin and nature of the two diffraction peaks, their signal has been recorded as a function of photon energy for the two different incident-light polarizations. The background below the $(00\frac{1}{2})$ peak was interpolated from energy scans at different q -positions around the peak, corresponding to: $L = 0.35, 0.4, 0.6,$ and 0.7 . The spectrum for the (001) peak was recorded at $L = 0.95$, with the background intensity taken at $L = 0.8$.

5.4 Spectroscopic analysis

The spectra obtained from the peaks and backgrounds are presented in Fig. 5.5. The shapes of the spectra for the two peaks are distinctly different: the L_3 part of the $(00\frac{1}{2})$ spectrum has a sharp resonance maximum at 708.4 eV, while the spectrum of the (001) peak shows a double peak structure, one peak at 708.6 eV, i. e. almost the same energy as the maximum of the $(00\frac{1}{2})$ spectrum, and the second one at 710.1 eV. The L_2 parts of the spectra, on the other hand, are more similar with two maxima at 720 eV and 721.4 eV. The $(00\frac{1}{2})$ spectrum shows a strong polarization dependence in the intensity and a weaker one in the spectral shape: for π polarization there is a shoulder on the low energy side of the L_3 resonance, which is almost missing in the σ spectrum; the relative intensity of the peaks in the L_2 part of the spectrum is different as well. All Fe-edge spectra are much more intense than the corresponding data from the oxygen- K edge (inset in Fig. 5.5).

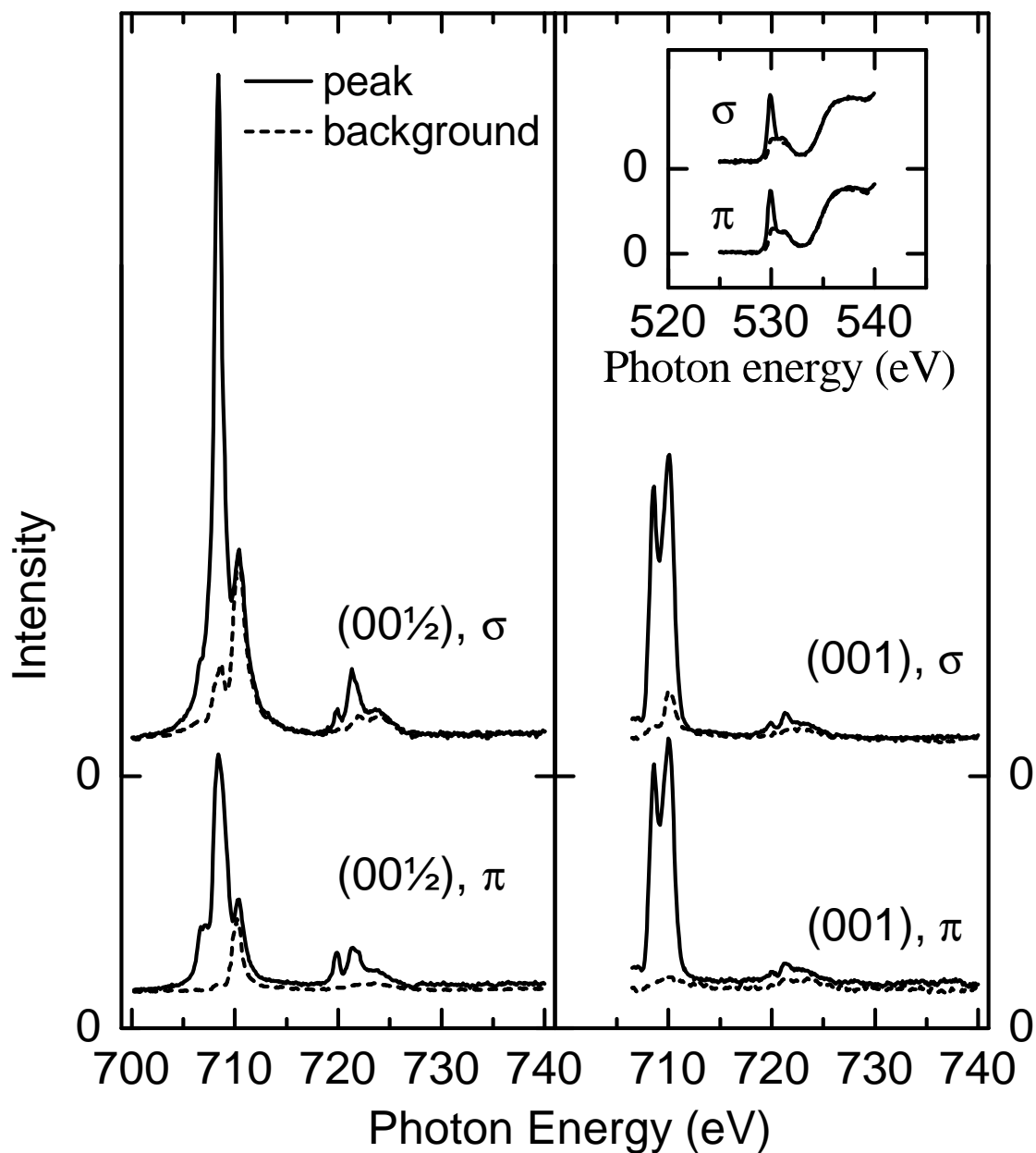


Figure 5.5: Spectra of the $(00\frac{1}{2})$ (left) and (001) (right) diffraction peaks (solid lines) and the corresponding backgrounds (dashed lines) recorded with σ (upper frames) and π (lower frames) polarized light. The inset shows the $(00\frac{1}{2})$ spectra recorded at the oxygen K -edge for comparison. All spectra are plotted on the same vertical scale.

In order to determine to what extent our results are influenced by film properties, we have carried out experiments using a film twice as thick as the one presented above and grown on a flat MgO substrate. We have seen that the reflectivity background below the $(00\frac{1}{2})$ peak was larger and that the onset of the much narrower (001) peak was less well defined. These findings however, justify precisely our motivation to use thin films on a miscut substrate rather than a bulk crystal with a low index surface as outlined in the experimental paragraph above. The key data of this thicker film are identical to those of the 40 nm film: both the $(00\frac{1}{2})$ and (001) diffraction peaks can be observed below T_V and both disappear above T_V ; the energy dependence of their intensities are very similar to the ones shown in Fig. 5.5. Furthermore the shape of the oxygen resonance of the $(00\frac{1}{2})$ peak of the thin film on the stepped surface, as shown in Fig. 5.5, agrees with the one observed in Ref. [35], which was recorded from a bulk crystal. This together indicates that the results presented are not characteristic for a magnetite film, but that they are indeed representative for the bulk material.

In Fig. 5.6 we present the resonance spectra of the two diffraction features after background subtraction together with the Fe $L_{2,3}$ XAS spectrum. The spectral lineshapes for the two diffraction peaks are clearly different from the XAS spectrum [symbols in Fig. 5.6a)].

To interpret the spectroscopic results, we resort to the existing literature on the XAS of Fe_3O_4 [108, 118] with emphasis on the strong magnetic circular and linear dichroism [108, 118] effects therein. The sharp structures in the dichroic spectra allow for a clear decomposition of the XAS spectrum in terms of contributions coming from the different Fe sites in magnetite. This decomposition is given in Fig. 5.6a): the spectrum from the B-site Fe^{2+} ion is shown by the red thick solid line, the A-site Fe^{3+} by the green dotted line, and the B-site Fe^{3+} by the blue dashed line. The maximum in the L_3 white line of each of these ions occurs at quite different energies, an aspect which we will utilize next to interpret the (001) and $(00\frac{1}{2})$ diffraction peaks.

The maximum of the $(00\frac{1}{2})$ diffraction peak spectrum occurs at essentially the same energy as that of the B-site Fe^{2+} XAS. This means that the observed $(00\frac{1}{2})$ diffraction peak is due to order, which involves *only* B-site Fe^{2+} ions. This in turn implies that orbital order of the t_{2g} electrons is at play here, since this is the only degree of freedom available which could make one B-site Fe^{2+} ion to be different from another B-site Fe^{2+} ion. Since $(00\frac{1}{2})$ is a glide-plane forbidden reflection, a charge order as proposed in Ref. 5.2, would not contribute to the this signal, since all non-diagonal elements of the scattering tensor vanish for this reflection [45].

One of the two peaks of the (001) spectrum occurs essentially at the energy of the maximum of the B-site 2+ resonance, and the other peak is split off by about 1.5 eV. Such a double-peak structure is exactly the resonance shape to be expected from two resonances well separated in energy (see Section 1.4), as it is the case for the B-site Fe^{2+} and Fe^{3+} ions. However, since the (001) reflection is not structure forbidden, but merely very weak, the shape of the resonance needs a careful study.

One has to investigate, whether the observed intensity is really due to charge order in the system, resulting in an inhomogeneous arrangement of the two B-site ions: Fe^{2+} and Fe^{3+} , or whether the distribution of the Fe^{2+} and Fe^{3+} in the system is homogeneous, leading to a formal average valency of $\text{Fe}^{2.5+}$ on the B-sites. We

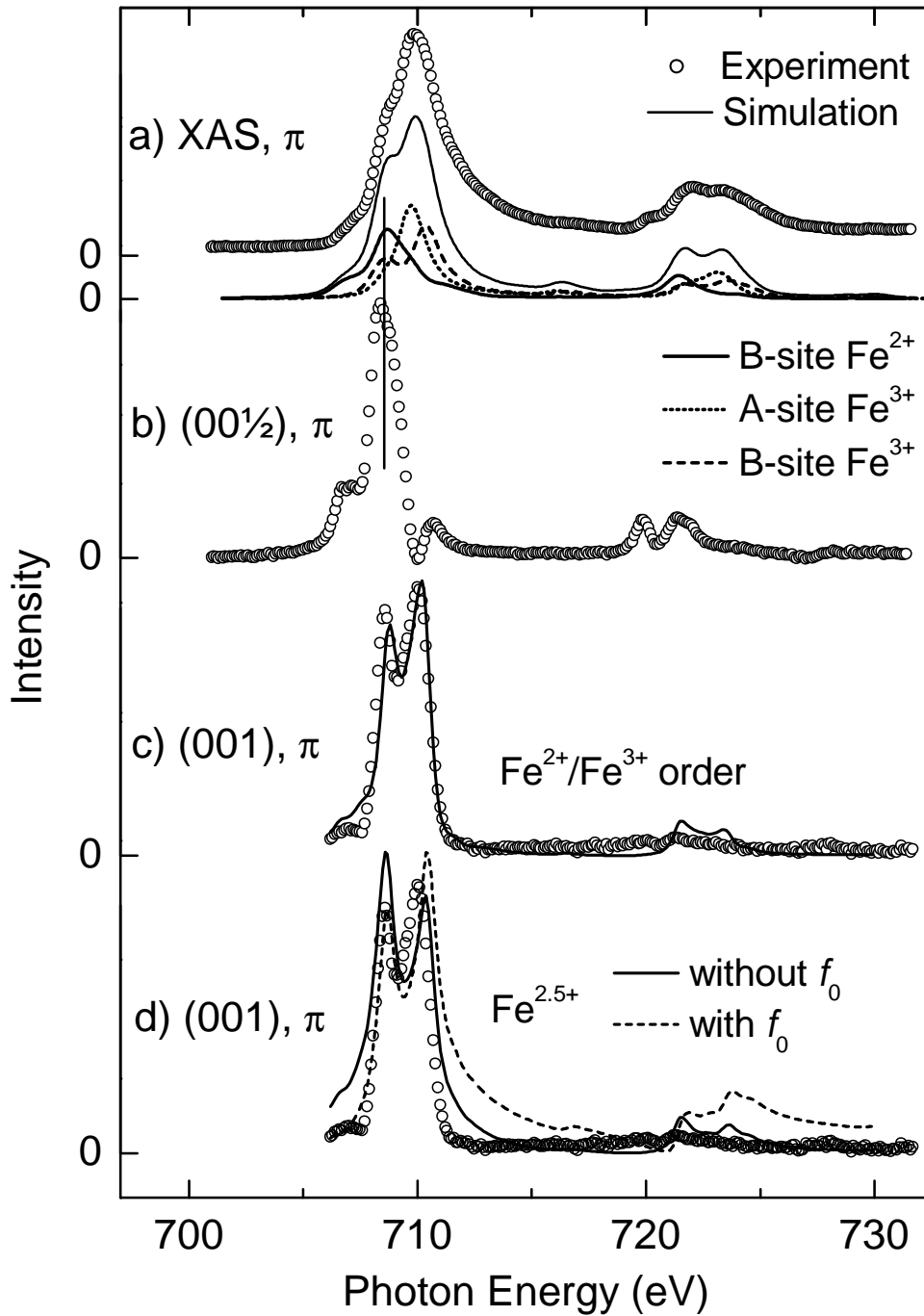


Figure 5.6: a) Experimental Fe $L_{2,3}$ XAS spectra of Fe_3O_4 (symbols). The thin solid line below the data is a simulation, which is constructed as the sum of the spectra from the B-site Fe^{2+} (thick solid line), A-site Fe^{3+} (dotted line), and B-site Fe^{3+} (dashed line) ions; b) energy dependence of the $(00\frac{1}{2})$ diffraction peak intensity; c) and d) energy dependence of the (001) intensity: data (symbols) with simulations assuming; c) charge order with (001) modulation on B-sites; d) homogeneous charge distribution (formal $\text{Fe}^{2.5+}$) on B-sites; the dashed line takes into account f^0 .

have simulated these two cases, considering the structure proposed by Ref. [102]. The complex scattering amplitudes for the Fe-ions were extracted from the XAS subspectra in Fig. 5.6a). The results are plotted in Fig. 5.6c) and d), over the data points (symbols). Fig. 5.6c) shows a simulation assuming charge order on the B-sites with a modulation vector of (001). The agreement between the experiment and simulation is very good; the steep onset of the resonance and the relative intensities of the two peaks are well reproduced. The simulations in Fig. 5.6d) consider a homogeneous charge distribution on the B-sites, i.e. no charge ordering. The curves show a broader resonance, coinciding not so well with the data points. The dashed line takes into account the non-resonant term f_0 , which vanishes in the non-homogeneous case (c). In similarity to Section 1.4, the interference term $f_0 f'$ leads to asymmetry in the line shape, a behavior which is certainly not observed in the data. This scenario can be therefore ruled out. Calculation of the structure factor for the $P2/c$ cell yields a 100-times stronger intensity if charge order on the Fe^{2+} and Fe^{3+} sites is assumed; a result strongly supporting the presented spectral analysis. We can therefore safely conclude that there is a B-site charge order in the system below the Verwey temperature, which is characterized by a (001) wave vector. The claim made in Ref. [112] that charge order does not exist in this system can be therefore clearly ruled out.

In order to quantify the amount of charge modulation one has to differentiate between the total d -electron count on the iron sites and the t_{2g} occupation. In a purely ionic picture the difference between the divalent and trivalent Fe ions would be one t_{2g} electron. On the other hand the hybridization between iron and oxygen involves mainly the iron e_g states, which are oriented towards the oxygen ligands. We can hence expect the Fe^{3+} ions to have a lower t_{2g} , but a higher e_g occupation than the Fe^{2+} ions such that the modulation of the t_{2g} occupation in the charge-ordered state is partially screened by an opposite modulation of the e_g occupation. From the cluster calculation [59] used to simulate the XAS spectrum in Fig. 2 we find a t_{2g} occupation of 3.18 for the 3+ sites and 4.04 for the 2+ sites. In addition to the hybridization with the neighboring oxygen $2p$ orbitals a deviation from the ionic model due to band formation could further reduce the effective charge modulation. We can estimate the amount of this reduction by using the results of an earlier combined photoemission/inverse photoemission study [119]. There it was found that the effective charge-transfer energy for the electron hopping process $\text{Fe}^{2+} + \text{Fe}^{3+} \rightarrow \text{Fe}^{3+} + \text{Fe}^{2+}$ is about $V_{\text{eff}} = 1$ to 1.5 eV. Using further the Harrison relations [120] we find a value of $t \approx 0.25$ eV for the hopping integral between iron B-sites. The amount of mixing is then of the order of $t^2/V_{\text{eff}}^2 \approx 10\%$, which is a rather modest value. This means that the t_{2g} charge modulation will be about 0.7 - 0.8 electrons, a value very close to the LDA+U result [110].

5.5 Conclusions

Using resonant soft x-ray diffraction at the Fe- $L_{2,3}$ threshold from a film of magnetite grown on stepped MgO two modulation vectors were observed. From the spectral analysis of the signal the (001) diffraction peak could be clearly assigned to charge order of the B-site ions; providing the first direct prove for the existence of charge

order in magnetite. It could be further ruled out that the appearance of the $(00\frac{1}{2})$ reflection below the Verwey transition should be result of charge order too. The spectral shape of the signal clearly identifies it as belonging to orbital order of B-sites Fe^{2+} ions, in contrast to Ref. [35].

Summary

The study of ordering of electronic degrees of freedom: charge, orbital and magnetic order, is important for the understanding of many of the often spectacular properties of transition-metal oxides (TMO), including high-temperature superconductivity and metal-insulator transitions. While magnetic structure of a bulk systems can be investigated directly using neutron diffraction, an appropriate technique for the study of orbital and charge order was lacking for a long time. Neutrons are not sensitive to charge and therefore cannot detect charge or orbital order directly; they can only pick-up lattice distortions that such an order might induce on the crystal lattice. The suitable technique has to be directly charge sensitive, but beyond this in particular sensitive to the outer-shell electrons, since exactly these determine the electronic properties of a solid. The conventional x-ray diffraction technique rules therefore out, since the main intensity in the detected signal comes here from the inner-shell electrons. Also resonant x-ray diffraction at the transition metal K -edge was proved to be not sensitive enough to small changes in the configuration of the $3d$ electrons at the transition metal ions [17, 18].

Resonant soft x-ray diffraction is the appropriate technique to investigate electronic order in transition metal oxides [19]. Since soft x-rays have energies in the range 200 - 2000 eV, the photon energy can be tuned such, that the diffraction process will involve one of the following virtual excitations: oxygen $1s \rightarrow 2p$ (K edge) or transition metal $2p \rightarrow 3d$ ($L_{2,3}$ edge). It is known from x-ray absorption (XAS) data that variation of the photon scattering cross section across the TM $L_{2,3}$ edge is extremely sensitive to the electronic state of the transition metal oxides [61]. Whereas XAS delivers only average information about the electronic state of the system, resonant soft x-ray diffraction is structure-selective, so that only the coherent signal belonging to a long-range order with a certain periodicity is detected. This allows for spectroscopically-resolved structure study or, using an appropriate microscopic model, for structurally-resolved spectroscopy study. Resonant soft x-ray diffraction has therefore a high potential for investigation of mixed-valent transition-metal oxide systems, where an electronic phase-separation is expected.

In the last years the electronic order of a few TMO-systems has been investigated applying the resonant soft x-ray diffraction technique [22–35]. Nevertheless, a full spectral analysis of the data in terms of a realistic microscopic theory - as it is state of the art in the closely related x-ray absorption spectroscopy (XAS) - is very rare, showing that the technique is still in its infant state. Up to now most of the studies use a qualitative analysis of the spectral shape for the interpretation of their data.

The aim of this PhD work was the application of resonant soft x-ray diffraction

technique for the investigation of electronic order in transition metal oxides at the TM $L_{2,3}$ edge, trying to obtain a quantitative understanding of the data. The method was first systematically explored through application to a model system in order to test the feasibility of the technique and to understand of how x-ray optical effects have to be taken into account. Two more complex systems were investigated; stripe order in $\text{La}_{1.8}\text{Sr}_{0.2}\text{NiO}_4$ and charge and orbital order in Fe_3O_4 . The main focus of the work was on the *spectroscopic* potential of the technique, trying to obtain a level of quantitative description of the data. For x-ray absorption spectroscopy (XAS) from transition metal oxides, cluster configuration interaction calculation provides a powerful and realistic microscopic theory. In the frame work of this thesis cluster theory, considering explicit hybridization effects between the TM-ion and the surrounding oxygen ligands, has been applied for the first time to describe resonant diffraction data; previous publications confined themselves to a pure ionic picture in their model calculations [19, 24, 25]. Results of our calculations show indeed that hybridization plays an important role for TMO, due to the strong delocalization of charges over the $(\text{TM})\text{O}_6$ cluster.

The method was first applied to a model system, which was single crystalline SrTiO_3 with a stepped surface (Chapter 3). Although the density of the steps on the surface was smaller than $\frac{1}{50}$, a well pronounced diffraction signal was observed already far above the Ti $L_{2,3}$ resonance, the penetration depth being there larger than 100 nm. This proves that the technique is extremely sensitive and even able to detect signals from very dilute systems. The stepped-surface diffraction signal was investigated across the Ti $L_{2,3}$ resonance, showing the same resonance behavior as that of the optical data. We are convinced that this attribute is a fingerprint for a system, where the superstructure is due to a pure phase modulation, rather than to a contrast in the scattering amplitudes (the second would be the case for a structure peak produced by an electronic order).

From angle-dependent reflectivity measurements on flat-surface SrTiO_3 the optical constants δ and β have been obtained across the Ti $L_{2,3}$ resonance. Both vary strongly with energy, reaching values of the order of 10^{-3} and δ changing sign when a strong absorption maximum is crossed. This behavior totally dominates the optical properties of the system. Due to the sign-change in δ , the optical density of matter changes here from less dense than vacuum to more dense than vacuum close to an absorption maximum. This is in strong contrast to what is known from optical properties of hard x-rays, where matter is always less dense than vacuum. The photon penetration length in SrTiO_3 varies across the Ti $L_{2,3}$ resonance between 20 and 200 nm, showing that the method is not very surface sensitive. Nevertheless, it can be sensitive to the surface if the bulk material has no or a different superstructure. The values of the critical angle are considerably large, lying between 2-3 degrees outside resonance and reaching values up to 4.5 deg close to resonance maxima. Data measured at low incidence angles displays strong distortions due to the appearance of total external reflection.

Applying an extended kinematical model, the energy dependence of the reflectivity and the diffraction signal from the steps could be essentially reproduced, the model failing, however, to reproduce the subtle energy shift of the signal maxima

toward higher energies with a steeper incidence angle. The simulation does not account for the strong increase of reflectivity signal close to the critical angle.

The data from the second investigated system: stripe order in $\text{La}_{1.8}\text{Sr}_{0.2}\text{NiO}_4$ was presented in Chapter 4. Using resonant soft x-ray diffraction two well-pronounced superstructure reflections were observed in the system; $(2\epsilon, 0, 1)$ belonging to charge order and $(1-\epsilon, 0, 0)$ belonging to spin order. Both superstructure signals were investigated across the La $M_{4,5}$ and Ni $L_{2,3}$ resonance with linearly (π and σ) polarized light. Both show a strong resonance behaviour at the Ni $L_{2,3}$ edge, indicating that not only the magnetic moments, but also the doped charges reside within the NiO_2 layers. From the diffraction data the spin canting and the energy splitting between the partially un-occupied e_g states could be determined. The spin canting at 60 K was estimated to 15 deg, canting away from the stripes toward high and low temperatures. The crystal field splitting was estimated to 1 eV. The spectral behavior of the superstructure signals does not change in the temperature range between 37-135 K, demonstrating that the character of the order is conserved.

The photon-energy and polarization dependence of the charge and spin-order diffraction intensity across the Ni $L_{2,3}$ edges can be reproduced by a quantitative microscopic model calculation, which delivers a complete picture of the electronic states involved in the stripe structure in nickelates. The model assumes diagonal stripes of Ni^{2+} and Ni^{3+} -like ions, in which the Ni^{3+} -like objects are formed of a Ni^{2+} ion accompanied by a hole, which is essentially located at the surrounding in-plane oxygen ions, and couples antiferromagnetically to the Ni, in analogy to a Zhang-Rice singlet in cuprate systems [95]. This confinement to the in-plane oxygens could not be observed in XAS data [39]. The good agreement between experiment and calculation proves that differences in the hole concentration around the Ni ions, i.e. charge ordering, are the cause of the superstructure, providing the first direct prove for the existence of charge order in the $\text{La}_{1-x}\text{Sr}_x\text{NiO}_4$ system.

The third investigated system was charge and orbital order in magnetite (Chapter 5). The $(00\frac{1}{2})$ and (001) low-temperature reflections were studied from thin film Fe_3O_4 grown on stepped MgO , across the Fe- $L_{2,3}$ edge. The two diffraction peaks show a different spectral shape, which is also distinct from the absorption spectrum. From the spectral analysis (001) can be clearly assigned to charge order of the octahedral B-site ions; providing the first direct prove for the existence of charge order in magnetite. The $(00\frac{1}{2})$ reflection can be ruled out as belonging to charge order too, since its spectral shape indicates that the corresponding order involves only B-site Fe^{2+} ions. This reflection can be therefore assigned to orbital order on the divalent B-site irons, having an additional, orbital degree of freedom.

Bibliography

- [1] E. J. W. Verwey, *Nature* **144**, 327 (1939).
- [2] J. B. Goodenough, *Phys. Rev.* **100**, 564 (1955).
- [3] E. O. Wollan and W. C. Koehler, *Phys. Rev.* **100**, 545 (1955).
- [4] H. Yoshizawa, S. Mitsuda, H. Kitazawa, and K. Katsumata, *J. Phys. Soc. Jpn.* **57**, 3686 (1988).
- [5] R. J. Birgeneau, Y. Endoh, K. Kakurai, Y. Hidaka, T. Murakami, M. A. Kastner, T. R. Thurston, G. Shirane, and K. Yamada, *Phys. Rev. B* **39**, 2868 (1989).
- [6] T. R. Thurston, R. J. Birgeneau, M. A. Kastner, N. W. Preyer, G. Shirane, Y. Fujii, K. Yamada, Y. Endoh, K. Kakurai, M. Matsuda, Y. Hidaka, and T. Murakami, *Phys. Rev. B* **40**, 4585 (1989).
- [7] S.-W. Cheong, G. Aeppli, T. E. Mason, H. Mook, S. M. Hayden, P. C. Canfield, Z. Fisk, K. N. Clausen, and J. L. Martinez, *Phys. Rev. Lett.* **67**, 1791 (1991).
- [8] J. Zaanen and O. Gunnarsson, *Phys. Rev. B* **40**, 7391 (1989).
- [9] D. Poilblanc and T. M. Rice, *Phys. Rev. B* **39**, 9749 (1989).
- [10] M. Kato, K. Machida, H. Nakanishi, and M. Fujita, *J. Phys. Soc. Jpn.* **59**, 1047 (1990).
- [11] V. J. Emery and S. A. Kivelson, *Physica C* **235**, 189 (1994).
- [12] J. M. Tranquada, D. J. Buttrey, V. Sachan, and J. E. Lorenzo, *Phys. Rev. Lett.* **73**, 1003 (1994).
- [13] V. Sachan, D. J. Buttrey, J. M. Tranquada, J. E. Lorenzo, and G. Shirane, *Phys. Rev. B* **51**, 12742 (1995).
- [14] J. M. Tranquada, J. E. Lorenzo, D. J. Buttrey, and V. Sachan, *Phys. Rev. B* **52**, 3581 (1995).
- [15] Y. Murakami, H. Kawada, H. Kawata, M. Tanaka, T. Arima, Y. Moritomo, and Y. Tokura, *Phys. Rev. Lett.* **80**, 1932 (1998).

-
- [16] Y. Murakami, J. P. Hill, D. Gibbs, M. Blume, I. Koyama, M. Tanaka, H. Kawata, T. Arima, Y. Tokura, K. Hirota, and Y. Endoh, *Phys. Rev. Lett.* **81**, 582 (1998).
- [17] I. S. Elfimov, V. I. Anisimov, and G. A. Sawatzky, *Phys. Rev. Lett.* **82**, 4264 (1999).
- [18] M. Benfatto, Y. Joly, and C. R. Natoli, *Phys. Rev. Lett.* **83**, 636 (1999).
- [19] C. W. M. Castleton and M. Altarelli, *Phys. Rev. B* **62**, 1033 (2000).
- [20] P. Abbamonte, L. Venema, A. Rusydi, G. A. Sawatzky, G. Logvenov, and I. Bozovic, *Science* **297**, 581 (2002).
- [21] C. Schüßler-Langeheine, E. Weschke, A. Y. Grigoriev, H. Ott, R. Meier, D. V. Vyalikh, C. Mazumdar, C. Sutter, D. Abernathy, G. Grübel, and G. Kaindl, *Journ. Electron Spectrosc. Relat. Phenom.* **114**, 953 (2001).
- [22] S. B. Wilkins, P. D. Hatton, M. D. Roper, D. Prabhakaran, and A. T. Boothroyd, *Phys. Rev. Lett.* **90**, 187201 (2003).
- [23] S. B. Wilkins, P. D. Spencer, P. D. Hatton, S. P. Collins, M. D. Roper, D. Prabhakaran, and A. T. Boothroyd, *Phys. Rev. Lett.* **91**, 167205 (2003).
- [24] S. S. Dhesi, A. Mirone, C. D. Nadai, P. Ohresser, P. Bencok, N. B. Brookes, P. Reutler, A. Revcolevschi, A. Tagliaferri, O. Toulemonde, and G. van der Laan, *Phys. Rev. Lett.* **92**, 056403 (2004).
- [25] K. J. Thomas, J. P. Hill, S. Grenier, Y.-J. Kim, P. Abbamonte, L. Venema, A. Rusydi, Y. Tomioka, Y. Tokura, D. F. McMorrow, G. Sawatzky, and M. van Veenendaal, *Phys. Rev. Lett.* **92**, 237204 (2004).
- [26] U. Staub, V. Scagnoli, A. M. Mulders, K. Katsumata, Z. Honda, H. Grimmer, M. Horisberger, and J. M. Tonnerre, *Phys. Rev. B* **71**, 214421 (2005).
- [27] S. B. Wilkins, N. Stojic, T. A. W. Beale, N. Binggeli, C. W. M. Castleton, P. Bencok, D. Prabhakaran, A. T. Boothroyd, P. D. Hatton, and M. Altarelli, *Phys. Rev. B* **71**, 245102 (2005).
- [28] S. B. Wilkins, N. Stojic, T. A. W. Beale, N. Binggeli, C. W. M. Castleton, P. Bencok, D. Prabhakaran, A. T. Boothroyd, P. D. Hatton, and M. Altarelli, *Phys. Rev. B* **74**, 049902 (2006).
- [29] P. Abbamonte, G. Blumberg, A. Rusydi, A. Gozar, P. G. Evans, T. Siegrist, L. Venema, H. Eisaki, E. D. Isaacs, and G. A. Sawatzky, *Nature* **431**, 1078 (2004).
- [30] P. Abbamonte, A. Rusydi, S. Smadici, G. D. Gu, G. A. Sawatzky, and D. L. Feng, *Nature Physics* **1**, 155 (2005).

- [31] A. Rusydi, P. Abbamonte, H. Eisaki, Y. Fujimaki, G. Blumberg, S. Uchida, and G. A. Sawatzky, *Phys. Rev. Lett.* **97**, 016403 (2006).
- [32] C. Schüßler-Langeheine, J. Schlappa, A. Tanaka, Z. Hu, C. F. Chang, E. Schierle, M. Benomar, H. Ott, E. Weschke, G. Kaindl, O. Friedt, G. A. Sawatzky, H.-J. Lin, C. T. Chen, M. Braden, and L. H. Tjeng, *Phys. Rev. Lett.* **95**, 156402 (2005).
- [33] V. Scagnoli, U. Staub, A. M. Mulders, M. Janousch, G. I. Meijer, G. Hammerl, J. M. Tonnerre, and N. Stojic, *Phys. Rev. B* **73**, 100409 (2006).
- [34] I. Zegkinoglou, J. Strempler, C. S. Nelson, J. P. Hill, J. Chakhalian, C. Bernhard, J. C. Lang, G. Srajer, H. Fukazawa, S. Nakatsuji, Y. Maeno, and B. Keimer, *Phys. Rev. Lett.* **95**, 136401 (2005).
- [35] D. J. Huang, H.-J. Lin, J. Okamoto, K. S. Chao, H.-T. Jeng, G. Y. Guo, C.-H. Hsu, C.-M. Huang, D. C. Ling, W. B. Wu, C. S. Yang, and C. T. Chen, *Phys. Rev. Lett.* **96**, 096401 (2006).
- [36] H. Ott, C. Schussler-Langeheine, E. Schierle, G. Kaindl, and E. Weschke, *Appl. Phys. Lett.* **88**, 212507 (2006).
- [37] H. Ott, C. Schussler-Langeheine, E. Schierle, A. Y. Grigoriev, V. Leiner, H. Zabel, G. Kaindl, and E. Weschke, *Phys. Rev. B* **74**, 094412 (2006).
- [38] H. Ott, Ph.D. thesis, Freie Universität Berlin, 2004.
- [39] E. Pellegrin, J. Zaanen, H.-J. Lin, G. Meigs, C. T. Chen, G. H. Ho, H. Eisaki, and S. Uchida, *Phys. Rev. B* **53**, 10667 (1996).
- [40] M. Imada, A. Fujimori, and Y. Tokura, *Rev. Mod. Phys.* **70**, 1039 (1998).
- [41] W. C. Koehler, in *Magnetic structures of rare earth metals and alloys*, Vol. 1 of *Magnetic properties of rare earth metals*, edited by R. J. Elliot (Plenum Press, London, New York, 1972).
- [42] J. Als-Nielsen and D. McMorrow, *Elements of Modern X-ray Physics* (Wiley, New York, 2001).
- [43] A. Guinier, in *X-ray Diffraction in Crystals, Imperfect Crystals, and Amorphous Bodies* (Dover, New York, 1994).
- [44] D. H. Templeton and L. K. Templeton, *Acta Cryst. A* **36**, 237 (1980).
- [45] V. E. Dmitrienko, *Acta Cryst. A* **39**, 29 (1983).
- [46] M. Blume, *J. Appl. Phys.* **57**, 3615 (1985).
- [47] P. Rennert, *Phys. Rev. B* **48**, 13559 (1993).
- [48] D. Waasmaier and A. Kirfel, *Acta Cryst. A* **51**, 416 (1995).

- [49] D. Gibbs, M. Blume, D. R. Harshman, and D. B. McWhan, *Rev. Sci. Instrum.* **60**, 1655 (1989).
- [50] J. P. Hannon, G. T. Trammell, M. Blume, and D. Gibbs, *Phys. Rev. Lett.* **61**, 1245 (1988).
- [51] R. V. Vedrinskii, V. L. Kraizman, A. A. Novakovich, and V. S. Machavariani, *J Phys.: Condens. Matter* **4**, 6155 (1992).
- [52] P. Carra and B. T. Thole, *Rev. Mod. Phys.* **66**, 1509 (1994).
- [53] J. P. Hill and D. F. McMorrow, *Acta Cryst. A* **52**, 236 (1996).
- [54] E. N. Ovchinnikova and V. E. Dmitrienko, *Acta Cryst. A* **56**, 2 (2000).
- [55] M. Born and E. Wolf, *Principles of Optics* (Pergamon Press, Oxford, 1970).
- [56] J. D. Jackson, in *Classical electrodynamics* (Wiley, New York, 1962).
- [57] S. Gasiorowicz, *Quantum physics* (Wiley, New York, 1996).
- [58] See review in the Theo Thole memorial issue, *J. Electron Spectrosc. Relat. Phenom.* **86**, 1 (1997).
- [59] A. Tanaka and T. Jo, *J. Phys. Soc. Jpn.* **63**, 2788 (1994).
- [60] Detailed description on this theoretical method and on the simulation program written by Arata Tanaka is given in the doctoral thesis of Maurits Haverkort [62].
- [61] F. M. F. de Groot, *J. Electron Spectrosc. Relat. Phenom.* **67**, 529 (1994).
- [62] M. W. Haverkort, Ph.D. thesis, Universität zu Köln, 2005.
- [63] E. Weschke, *Patent registration: Vakuum-Drehdurchführung (vacuum rotary feed-through), Aktenzeichen: 103 16 730.7* (Deutsches Patentamt, Berlin, delivered: 7th of April 2003).
- [64] F. M. F. de Groot, J. C. Fuggle, B. T. Thole, and G. A. Sawatzky, *Phys. Rev. B* **41**, 928 (1990).
- [65] G. Koster, B. L. Kopman, G. Rijnders, D. H. A. Blanck, and H. Rogolle, *Appl. Phys. Lett.* **73**, 2920 (1998).
- [66] M. Deutsch and B. M. Ocko, in *X-ray and neutron reflectivity*, Vol. 23 of *Encyclopedia of Applied Physics*, edited by G. L. Trigg (Wiley-VCH, Weinheim, 1998).
- [67] B. L. Henke, E. M. Gullikson, and J. Davis, *Atomic Data and Nuclear Data Tables* **54**, 181 (1993).
- [68] R. Souffi and E. M. Gullikson, *Appl. Opt.* **36**, 5499 (1997).

- [69] D. Alders, Ph.D. thesis, Rijksuniversiteit Groningen, 1996.
- [70] G. H. Lander, P. J. Brown, J. Spal/ek, and J. M. Honig, *Phys. Rev. B* **40**, 4463 (1989).
- [71] G. H. Lander, P. J. Brown, C. Stassis, P. Gopalan, J. Spalek, and G. Honig, *Phys. Rev. B* **43**, 448 (1991).
- [72] R. J. Cava, B. Batlogg, T. T. Palstra, J. J. Krajewski, W. F. Peck, A. P. Ramirez, and L. W. Rupp, *Phys. Rev. B* **43**, 1229 (1991).
- [73] P. Kuiper, J. van Elp, G. A. Sawatzky, A. Fujimori, S. Hosoya, and D. M. de Leeuw, *Phys. Rev. B* **44**, 4570 (1991).
- [74] S. M. Hayden, G. H. Lander, J. Zarestky, P. J. Brown, C. Stassis, P. Metcalf, and J. M. Honig, *Phys. Rev. Lett.* **68**, 1061 (1992).
- [75] C. H. Chen, S.-W. Cheong, and A. S. Cooper, *Phys. Rev. Lett.* **71**, 2461 (1993).
- [76] X.-X. Bi, P. C. Eklund, and J. M. Honig, *Phys. Rev. B* **48**, 3470 (1993).
- [77] S.-H. Lee and S.-W. Cheong, *Phys. Rev. Lett.* **79**, 2514 (1997).
- [78] J. M. Tranquada, D. J. Buttrey, and V. Sachan, *Phys. Rev. B* **54**, 12318 (1996).
- [79] J. M. Tranquada, J. D. Axe, N. Ichikawa, A. R. Moodenbaugh, Y. Nakamura, and S. Uchida, *Phys. Rev. Lett.* **78**, 338 (1997).
- [80] J. M. Tranquada, N. Ichikawa, and S. Uchida, *Phys. Rev. Lett.* **88**, 14712 (1999).
- [81] P. Wochner, J. M. Tranquada, D. J. Buttrey, and V. Sachan, *Phys. Rev. B* **57**, 1066 (1998).
- [82] C.-H. Du, M. E. Ghazi, Y. Su, I. Pape, P. D. Hatton, S. D. Brown, W. G. Stirling, M. J. Cooper, and S.-W. Cheong, *Phys. Rev. Lett.* **84**, 3911 (2000).
- [83] P. G. Freeman, A. T. Boothroyd, D. Prabhakaran, D. González, and M. Enderle, .
- [84] P. D. Hatton, M. E. Ghazi, W. B. Wilkins, P. D. Spencer, D. Mannix, T. d'Almeida, P. Prabhakaran, and A. Boothroyd, *Int. J. Mod. Phys. B* **16**, 1633 (2002).
- [85] S.-H. Lee, S.-W. Cheong, K. Yamada, and C. F. Majkrzak, *Phys. Rev. B* **63**, 060405 (2001).
- [86] J. Li, Y. Zhu, J. M. Tranquada, K. Yamada, and D. J. Buttrey, *Phys. Rev. B* **67**, 012404 .

- [87] H. Yoshizawa, T. Kakeshita, R. Kajimoto, T. Tanabe, T. Katsufuji, and Y. Tokura, Phys. Rev. B **61**, R854 (2000).
- [88] P. G. Freeman, A. T. Boothroyd, D. Prabhakaran, M. Enderle, and C. Niedermayer, Phys. Rev. B **70**, 024413 (2004).
- [89] M. E. Ghazi, P. D. Spencer, S. B. Wilkins, P. D. Hatton, D. Mannix, D. Prabhakaran, A. T. Boothroyd, and S.-W. Cheong, Phys. Rev. B **70**, 144507 (2004).
- [90] P. D. Hatton, M. E. Ghazi, W. B. Wilkins, P. D. Spencer, D. Mannix, T. d'Almeida, P. Prabhakaran, A. Boothroyd, and C. W. Cheong, Physica B **318**, 289 (2002).
- [91] V. Hinkov, S. Pailhès, P. Bourges, Y. Sidis, A. Ivanov, A. Kulakov, C. T. Lin, D. P. Chen, C. Bernhard, and B. Keimer, Nature (London) **430**, 650 (2004).
- [92] T. Hanaguri, C. Lupien, Y. Kohsaka, D.-H. Lee, M. Azuma, M. Takano, H. Takagi, and J. C. Davis, Nature (London) **430**, 1001 (2004).
- [93] M. Benomar, Ph.D. thesis, Universität zu Köln, in preparation.
- [94] P. Kuiper, G. Kruizinga, J. Ghijsen, G. A. Sawatzky, and H. Verweij, Phys. Rev. Lett. **62**, 221 (1989).
- [95] F. C. Zhang and T. M. Rice, Phys. Rev. B **37**, 3759 (1988).
- [96] H. Eskes and G. A. Sawatzky, Phys. Rev. Lett. **61**, 1415 (1988).
- [97] J. M. Tranquada, P. Wochner, A. R. Moodenbaugh, and D. J. Buttrey, Phys. Rev. B **55**, R6113 (1997).
- [98] E. D. Isaacs, G. Aeppli, P. Zschack, S.-W. Cheong, H. Williams, and D. J. Buttrey, Phys. Rev. Lett. **72**, 3421 (1994).
- [99] G. Aeppli and D. J. Buttrey, Phys. Rev. Lett. **61**, 203 (1988).
- [100] E. Collart, A. Shukla, J.-P. Rueff, P. Leininger, H. Ishii, I. Jarrige, Y. Q. Cai, S.-W. Cheong, and G. Dhalenne, Phys. Rev. Lett. **96**, 157004 (2006).
- [101] S. Bogner and S. Scheidl, Phys. Rev. B **64**, 054517 (2001).
- [102] J. P. Wright, J. P. Attfield, and P. G. Radaelli, Phys. Rev. B **66**, 214422 (2002).
- [103] E. J. W. Verwey, Nature (London) **144**, 327 (1939).
- [104] N. Tsuda, K. Nasu, A. Yanase, and K. Siratori, *Electronic Conduction in Oxides* (Springer, Berlin, 1991).
- [105] J. P. Wright, J. P. Attfield, and P. G. Radaelli, Phys. Rev. Lett. **87**, 266401 (2001).

- [106] W. Eerenstein, T. T. M. Palstra, T. Hibma, and S. Celotto, Phys. Rev. B **66**, 201101(R) (2002).
- [107] Z. Szotek, W. M. Temmerman, A. Svane, L. Petit, G. M. Stocks, and H. Winter, Phys. Rev. B **68**, 054415 (2003).
- [108] J. Chen, D. J. Huang, A. Tanaka, C. F. Chang, S. C. Chung, W. B. Wu, and C. T. Chen, Phys. Rev. B **69**, (2004).
- [109] D. J. Huang, C. F. Chang, H.-T. Jeng, G. Y. Guo, H.-J. Lin, W. B. Wu, H. C. Ku, A. Fujimori, Y. Takahashi, and C. T. Chen, Phys. Rev. Lett. **93**, 077204 (2004).
- [110] I. Leonov, A. N. Yaresko, V. N. Antonov, M. A. Korotin, and V. I. Anisimov, Phys. Rev. Lett. **93**, 146404 (2004).
- [111] H.-T. Jeng, G. Y. Guo, and D. J. Huang, Phys. Rev. Lett. **93**, 156403 (2004).
- [112] G. Subías, J. García, J. Blasco, M. G. Proietti, H. Renevier, and M. C. Sánchez, Phys. Rev. Lett. **93**, 156408 (2004).
- [113] G. Subias, J. Garcia, and J. Blasco, Phys. Rev. B **71**, 155103 (2005).
- [114] M. M. Seikh, C. Narayana, P. A. Metcalf, J. M. Honig, and A. K. Sood, Phys. Rev. B **71**, 174106 (2005).
- [115] E. Goering, S. Gold, M. Lafkioti, G. Schutz, and V. A. M. Brabers, Phys. Rev. B **72**, 033112 (2005).
- [116] R. J. McQueeney, M. Yethiraj, W. Montfroofij, J. S. Gardner, P. Metcalf, and J. M. Honig, Phys. Rev. B **73**, 174409 (2006).
- [117] P. W. Anderson, Phys. Rev. **102**, 1008 (1956).
- [118] P. Kuiper, B. G. Searle, L.-C. Duda, R. M. Wolf, and P. J. van der Zaag, J. Electron Spectrosc. Relat. Phenom. **86**, 107 (1997).
- [119] J.-H. Park, L. H. Tjeng, J. W. Allen, P. Metcalf, and C. T. Chen, Phys. Rev. B **55**, 12813 (1997).
- [120] W. A. Harrison, *Electronic Structure and the Properties of Solids* (W. H. Freeman and Co., San Francisco, 1980).

Zusammenfassung

Die hochkorrelierten Elektronensysteme sind bekannt für ihre oft ungewöhnlichen Eigenschaften, wie Metall-Isolator Übergänge und Hochtemperatursupraleitung. Insbesondere die gemischt-valenten Systeme unter ihnen zeigen eine Reihe von Ordnungsphänomenen, bekannt als Ordnung elektronischer Freiheitsgrade: Ladungsordnung, orbitale Ordnung und magnetische Ordnung. Während die magnetische Struktur eines Systems mittels Neutronenbeugung untersucht werden kann, fehlte es lange Zeit an einer geeigneten Beugungsmethode, die direkt auf Ladungs- bzw. orbitale Ordnung empfindlich wäre. Da Neutronen nicht mit der Ladung wechselwirken, kann Ladungs- bzw. orbitale Ordnung mittels Neutronendiffraktion höchstens indirekt nachweisen werden. Auch die konventionelle Röntgenbeugung im harten Röntgenbereich (Energien ≥ 10 keV) scheidet hier aus, da das Signal einen zu niedrigen Kontrast für die Elektronen der äußeren Schalen liefert. Es sind aber gerade die Valenzelektronen, die die elektronischen Eigenschaften von Festkörpern bestimmen und die an der Ausbildung von elektronischer Ordnung beteiligt sind; in Übergangsmetalloxiden (ÜMO) sind es die $3d$ -Elektronen des Übergangsmetalls (ÜM). Die geeignete Technik um elektronische Überstrukturen in ÜMO-Systemen zu untersuchen liefert deshalb resonante weiche Röntgenbeugung an der ÜM $L_{2,3}$ -Kante [19].

Weiche Röntgenstrahlen haben Energien im Bereich 200 - 2000 eV, wo folgende elektronische Übergänge stattfinden: Sauerstoff $1s \rightarrow 2p$ (K -Kante), ÜM $2p \rightarrow 3d$ ($L_{2,3}$ -Kante) und Lanthanid $3d \rightarrow 4f$ ($M_{4,5}$ -Kante). Aus der Röntgen-Absorptionsspektroskopie (XAS) weißman, dass die Änderung des Wirkungsquerschnitts der Photonen an der ÜM $L_{2,3}$ -Kante sehr empfindlich auf den elektronischen Zustand des ÜMO-Systems ist [61]. Während jedoch XAS nur die gemittelte Information über den elektronischen Zustand des gesamten Systems liefert, ist resonante weiche Röntgenbeugung Struktur-selektiv, da hier ausschließlich das kohärente Signal einer langreichweitigen Ordnung mit einer ganz bestimmten Periodizität gemessen wird. Das erlaubt spektroskopisch-aufgelöste Strukturuntersuchungen, bzw. strukturell-aufgelöste Spektroskopie.

In den letzten Jahren wurden bereits einige der ÜMO-Systeme mittels resonanter weicher Röntgenbeugung untersucht [22–35]. Die meisten Interpretationen der Daten beschränkten sich jedoch auf eine qualitative Analyse. Vollständige Spektralanalyse mittels einer realistischen mikroskopischen Theorie (in XAS ein Standard) stellt hier noch eine Ausnahme dar, was beweist dass sich die Methode noch in ihren Kinderschuhen befindet.

Im Rahmen dieser Arbeit wurde die resonante weiche Röntgenbeugung zur Un-

tersuchung von elektronischer Ordnung in ÜMO-Systemen an der ÜM $L_{2,3}$ -Kante benutzt. Ein Schwerpunkt in der Analyse lag auf einem quantitativen Verständniss der experimentellen Ergebnisse. Die Methode wurde zuerst an einem Modellsystem untersucht, um sie unter anderem auf ihre Durchführbarkeit und Empfindlichkeit zu testen. Insbesondere wurde hier der Einfluss von optischen Effekten im weichen Röntgenbereich systematisch untersucht. Experimente an komplexeren Systemen folgten: Untersuchung der Streifenphase in $\text{La}_{1.8}\text{Sr}_{0.2}\text{NiO}_4$ und der Ladungs- und orbitalen Ordnung in Fe_3O_4 . Die elektronische Ordnung in diesen Systemen konnte erfolgreich nachgewiesen werden.

Für eine quantitative Beschreibung der Daten wurde die Cluster-Theorie herangezogen, die eine vollständige atomische Multiplettbeschreibung liefert. Die Hybridisierungseffekte zwischen den Übergangsmetallionen und den benachbarten Sauerstoffen wurden hier explizit berücksichtigt. Obwohl dieses theoretische Werkzeug für die Absorptionsspektroskopie im weichen Röntgenbereich ein bewährtes mikroskopisches Model darstellt, wurde es im Rahmen dieser Arbeit zum ersten Mal zur Analyse von Röntgenbeugungsdaten herangezogen. Vorherige Modellrechnungen beschränkten sich ausschliesslich auf ein ionisches Bild [19, 24, 25]. Unsere Daten zeigen dagegen, dass Hybridisierung eine wichtige Rolle bei Übergangsmetalloxiden spielt, da hier die Ladungen stark über das gesamte $(\ddot{\text{U}}\text{M})\text{O}_6$ -Cluster delokalisiert sind.

Durch Messungen an dem Modellsystem SrTiO_3 mit einer gestuften Oberfläche (präsentiert in Kapitel 3) konnte die Durchführbarkeit der Methode gezeigt werden. Die kleine Stufendichte ($< \frac{1}{50}$) lieferte ein starkes Beugungssignal, das an der Ti $L_{2,3}$ -Kante um ein 10-faches verstärkt werden konnte. Dies beweist eine große Empfindlichkeit der Methode und das Potential auch stark verdünnte Systeme zu untersuchen. Das Beugungssignal der Stufen lieferte an der Ti $L_{2,3}$ -Kante dasselbe Resonanzverhalten wie die optischen Daten. Wir glauben dass dies ein charakteristisches Merkmal eines System ist, in dem die Überstruktur ein Resultat reiner Phasenmodulation ist - im Gegensatz zu elektronisch geordneten Systemen, wo der Kontrast durch Unterschiede in den Streuamplituden zustande kommt. Ferner konnten die optischen Konstanten von SrTiO_3 bestimmt werden. Ihre starke Variation über der Ti $L_{2,3}$ -Kante, und insbesondere das Wechseln des Vorzeichens des Realteils des Brechungsindex, zeigten dass sich die optischen Eigenschaften der Materie in der Nähe von Resonanzen im weichen Röntgenbereich extrem ändern. Im harten Röntgenbereich ist Materie optisch immer dünner als Vakuum, an einer weichen Resonanz kann sie jedoch teilweise optisch dichter werden als Vakuum. Der kritische Winkel für Totalreflexion erreicht in SrTiO_3 Werte bis 4.5° , was zur Verformung von optischen Spektren für kleine Einfallswinkel führt. Die Eindringtiefe der Photonen variiert zwischen 20 and 200 nm. Die Energieabhängigkeit der Reflektivität und des Stufenbeugungssignals konnte mithilfe eines kinematischen Modells im Wesentlichen reproduziert werden, mit Ausnahme der Energieverschiebung der Signalmaxima mit dem Einfallswinkel.

Die Ergebnisse der resonanten weichen Röntgenbeugung an den Streifenphasen in $\text{La}_{1.8}\text{Sr}_{0.2}\text{NiO}_4$ (Kapitel 4) zeigen, dass sowohl die Spinordnung wie auch die

Ladungsordnung in den Ni-O Lagen lokalisiert sind. Die Energie- und Polarisationsabhängigkeit der Beugungsintensität des $(2\epsilon, 0, 1)$ -Ladungsreflexes und des $(1-\epsilon, 0, 0)$ -Spinreflexes an der Ni $L_{2,3}$ -Kante konnte durch eine quantitative mikroskopische Modellrechnung reproduziert werden. In diesem Modell wird das System durch eine Anordnung von diagonalen Streifen aus Ni^{2+} und Ni^{3+} Clustern beschrieben. Das zusätzliche Loch in dem Ni^{3+} Cluster ist hauptsächlich auf den Nachbarsauerstoffen in der Ni-O-Ebene lokalisiert, wobei der Lochspin antiferromagnetisch an den Ni-Spin koppelt, in Analogie zu dem Zhang-Rice Singlet in den Kupraten [95]. Dieses Resultat liefert ein vollständiges Bild über den elektronischen Zustand der Streifenordnung in den Nickelaten.

Mit resonanter weicher Röntgenbeugung an Fe_3O_4 -dünnen Filmen auf MgO konnten die $(00\frac{1}{2})$ und (001) Reflexe der Niedrigtemperatur-Phase beobachtet werden. Die Spektralanalyse der Beugungsintensität an der Fe $L_{2,3}$ -Kante zeigt, dass das Signal bei $(00\frac{1}{2})$ ein Resultat der orbitalen Ordnung an den zweiwertigen Eisen B-Plätzen ist, während (001) auf Ladungsordnung auf den B-Plätzen zurückzuführen ist.

Acknowledgements

In the first place I would like to thank Prof. Liu Hao Tjeng for the great opportunity to perform this PhD work in the nice atmosphere of his group. I would especially like to thank him for his support and for his continuous encouragement toward a scientific career.

Prof. Jochen Schneider I would like to thank for co-assessing this thesis.

My special thanks goes to Christian Schüßler-Langeheine, who supervised this thesis and with whom I had the chance to share all the beamtimes where the data presented in this work was measured. His experimental skills and the broad technical knowledge are amazing and were crucial for the demanding requirements of the experiments. I have learned a lot from him. Thank you for the continuous support and guidance and for the persistence in getting these good results.

Maurits Haverkort I would like to thank for all the discussions. I have learned a lot from him about the correlated systems, resonant scattering and solid state physics in general. He was always willing to answer questions and never getting tired with even more questions. Our projects also profited a lot from these discussions. Thank you very much for this.

I would also especially like to thank our collaborator Arata Tanaka for the cluster calculations on the $\text{La}_{1.8}\text{Sr}_{0.2}\text{NiO}_4$ system and for his visit in Cologne. We have learned a lot from him about the application of cluster theory to resonant soft x-ray diffraction data.

Here I would like to thank people supporting us at beamlines. Many thanks to Eugen Weschke for the possibility of using his diffractometer in BESSY. Special thanks to Enrico Schierle for building up and commissioning of the diffractometer and for all the re-locations that had to be done with it between the beamtimes. Also thanks to Thomas Koethe for help with building up of the new machine. Enrico, Holger Ott and Zhiwei Hu I would like to thank for manpower support on the nickelates and SrTiO_3 . Also many thanks to Zhiwei Hu for helping us with the x-ray absorption measurements. I would like to thank Peter Abbamonte and Andriwo Rusydi for supporting us during the NSLS beamtimes and Ralf Feyerherm and Esther Dudzik for assistance during K-edge measurements on the nickelates.

The BESSY personnel I would like to thank for the good experimental conditions

at BESSY.

I would like to thank Mark Huijben, Guus Rijnders and Prof. Dave H. A. Blank for preparation of the SrTiO_3 samples. Mohammed Benomar I would like to thank for growing of the $\text{La}_{1.8}\text{Sr}_{0.2}\text{NiO}_4$ sample and Oliver Friedt for the neutron measurements on it. Thanks to Markus Kriener for the measurements of specific heat on $\text{La}_{1.8}\text{Sr}_{0.2}\text{NiO}_4$. Many thanks also to Zhiwei Hu for the XAS data on LaTiO_3 and Fe_3O_4 .

Chung Fu (Roger) Chang I would like to thank for the preparation of the Fe_3O_4 thin films and for the conductivity measurements. Also thank you for the shared beamtimes on the magnetite and SrTiO_3 project and especially for the great guidance through the Taiwanese culture/cuisine in October 2004!

I would like to thank Prof. Markus Braden for the very fruitful discussions on $\text{La}_{2-x}\text{Sr}_x\text{NiO}_4$. Eugen Weschke and Holger Ott I would like to thank for the useful discussions on $\text{La}_{2-x}\text{Sr}_x\text{NiO}_4$. Zhiwei Hu and Maurits Haverkort I would like to thank for all the discussions inspiring our projects. Our magnetite project profited a lot from the discussions with Daniil Khomskii and Paolo Radaelli and all our projects from discussion with Peter Abbamonte and George Sawatzky.

I would like to thank Lucie Hamdan for her skillful technical support in the laboratories in Cologne. The mechanics workshop of the II. Physikalisches Institut in Cologne I would like to thank for their excellent job, especially in manufacturing of the precision-mechanics pieces used in the experiments, including the sample holders and the Vernier-scale system to orient the bulk samples.

At this place I would like to thank the entire group of Prof. Tjeng in Cologne, and especially my room-mates: Maurits, Thomas, Jan and Dilek, for the nice atmosphere, the discussions and the mutual support. The entire II. Physikalisches Institut in Cologne I would like to thank for the good cooperation and the nice time.

Ich möchte mich auch ganz besonders bei meinen Eltern und Gustavo bedanken, die mich die ganze Zeit unterstützt und immer an mich geglaubt haben.

Erklärung

Ich versichere, dass ich die von mir vorgelegte Dissertation selbständig angefertigt, die benutzten Quellen und Hilfsmittel vollständig angegeben und die Stellen der Arbeit - einschließlich Tabellen, Karten und Abbildungen -, die anderen Werken im Wortlaut oder dem Sinn nach entnommen sind, in jedem Einzelfall als Entlehnung kenntlich gemacht habe; dass diese Dissertation noch keiner anderen Fakultät oder Universität zur Prüfung vorgelegen hat; dass sie - abgesehen von unten angegebenen Teilpublikationen - noch nicht veröffentlicht worden ist sowie, dass ich eine solche Veröffentlichung vor Abschluss des Promotionsverfahrens nicht vornehmen werde. Die Bestimmungen der Promotionsordnung sind mir bekannt. Die von mir vorgelegte Dissertation ist von Prof. Dr. Liu Hao Tjeng betreut worden.

Justine Schlappa

Publications

- *Systematic errors in multi-frequency EIT.*
J. Schlappa, E. Annese, and H. Griffiths,
Physiol. Meas. **21**, 111 (2000).
- *Watching electronic charge order in a crystal lattice.*
C. Schler-Langeheine, J. Schlappa, Z. Hu, O. Fried, E. Schierle, H. Ott,
E. Weschke, G. Kaindl, M. Benomar, M. Braden, and L. H. Tjeng,
BESSY - Highlights 2003, p. 16.
- *Comment on “Temperature-Dependent Fermi Gap Opening in the $c(6\times 4)$ - $C_{60}/Ag(001)$ Two-Dimensional Superstructure”.*
J. Schlappa, C. Schler-Langeheine, R. Scherer, and L. H. Tjeng,
Phys. Rev. Lett. **93**, 119701 (2004).
- *Spectroscopy of stripe order in $La_{1.8}Sr_{0.2}NiO_4$ using resonant soft x-ray diffraction.*
C. Schler-Langeheine, J. Schlappa, A. Tanaka, Z. Hu, C. F. Chang, E. Schierle,
M. Benomar, H. Ott, E. Weschke, G. Kaindl, O. Friedt, G. A. Sawatzky, H.-
J. Lin, C. T. Chen, M. Braden, and L. H. Tjeng,
Phys. Rev. Lett. **95**, 156402 (2005).
- *Direct observation of charge order and orbital ordering in magnetite.*
J. Schlappa, C. Schler-Langeheine, C. F. Chang, H. Ott, A. Tanaka, Z. Hu,
M. W. Haverkort, E. Schierle, E. Weschke, G. Kaindl, and L. H. Tjeng,
Submitted to Phys. Rev. Lett.; cond-mat/0605096.
- *Resonant soft x-ray diffraction from stepped surface on $SrTiO_3$.*
J. Schlappa, C. Schler-Langeheine, H. Ott, C. F. Chang, E. Schierle, E. Weschke,
A. Starodubov, G. Kaindl, M. Huijben, G. Rijnders, D. H. A. Blank, A. Rusydi,
P. Abbamonte, and L. H. Tjeng,
In preparation.
- *Temperature dependence of stripe order in $La_{1.8}Sr_{0.2}NiO_4$.*
J. Schlappa, C. Schler-Langeheine, A. Tanaka, Z. Hu, C. F. Chang, E. Schierle,
M. Benomar, H. Ott, E. Weschke, G. Kaindl, O. Friedt, G. A. Sawatzky, H.-
J. Lin, C. T. Chen, M. Braden, and L. H. Tjeng,
In preparation.

Curriculum vitae

Justine Sophia Schlappa

Day of birth: 29th of January 1974, Oppeln (Opole)

- | | |
|----------------------|--|
| Jan 2003 - Dez 2006 | Present PhD work, group of Prof. L. H. Tjeng,
II. Physikalisches Institut, Universität zu Köln. |
| Oct 1999 - Dec 2002 | Solid State Physics at Universität zu Köln.
Computer Sciences at Universität Bonn. |
| Oct 2001 - Dec 2002 | Diplom research (Diplomarbeit), Prof. L. H. Tjeng,
“Photoelectron Spectroscopy on 1 ML C ₆₀ / Ag(100)”,
II. Physikalisches Institut, Universität zu Köln. |
| June 1999 - Sep 1999 | Working-student at the Department of Medical
Physics and Clinical Engineering,
University Hospital of Wales, Cardiff, UK. |
| Sep 1998 - Sep 1999 | Scholarship for Erasmus studies,
Department of Physics and Astronomy,
University of Wales, Cardiff, UK. |
| Oct 1998 - Mai 1999 | Research in Medical Physics, Prof. H. Griffiths,
Dep. of Medical Physics and Clinical Engineering,
University Hospital of Wales, Cardiff, UK. |
| Oct 1995 - Sep 1998 | Physics at Universität zu Köln. |
| Aug 1997 - Sep 1997 | Miniforschung, group of Prof. R. Gross,
II. Physikalisches Institut, Universität zu Köln.
Rewarded with the Dieter-Wohlleben-Prize. |
| June 1995 | Abitur (A-level) at Humboldt-Gymnasium in Köln. |